



DEM/CFD-DEM Modelling of Non-spherical Particulate Systems: Theoretical Developments and Applications



Wenqi Zhong ^{a,b,*}, Aibing Yu ^{b,c}, Xuejiao Liu ^{a,c}, Zhenbo Tong ^{a,b}, Hao Zhang ^{a,b}

^a Key Laboratory of Energy Thermal Conversion and Control of Ministry of Education, School of Energy and Environment, Southeast University, Nanjing 210096, P.R. China

^b Centre for Simulation and Modelling of Particulate Systems, Southeast University - Monash University Joint Research Institute, Suzhou 215123, P.R. China

^c Department of Chemical Engineering, Monash University, Clayton, Vic 3800, Australia

ARTICLE INFO

Article history:

Received 25 February 2016

Received in revised form 1 June 2016

Accepted 3 July 2016

Available online 7 July 2016

Keywords:

non-spherical particles
discrete element method
computational fluid dynamics
particulate systems
CFD-DEM

ABSTRACT

Particles encountered in nature and engineering practice are normally not spherical but of irregular shapes. Particle shape plays a key role in determining the behaviour of bulk solids, which poses a number of challenges in modelling and simulation of particulate systems. Discrete element method (DEM) has been recognized as a promising method to meet the challenges. This paper presents a review of the recent efforts in developing DEM approaches to model non-spherical particulate systems (NSPS) and strategies of coupling such a non-spherical DEM model with computational fluid dynamics (CFD) for particle-fluid flows. It mainly covers four important aspects: the techniques for representation of non-spherical particles and their contact detection, the models describing inter-particle collision dynamics and fluid-particle forces, CFD-DEM coupling methodologies including averaged volume method and immersed family methods and the applications of the developed theories to the modelling of different NSPS. The main findings are discussed and summarized as a part of the review. Finally, the needs for future development are highlighted.

© 2016 Elsevier B.V. All rights reserved.

Contents

1. Introduction	109
1.1. Description of non-spherical particulate system	109
1.2. DEM modelling on non-spherical particles	110
1.3. Scope of this work	111
2. Representation of non-Spherical particles and contact detections	112
2.1. Single-particle method	112
2.1.1. Polygons and polyhedrons	112
2.1.2. Continuous function representations	113
2.1.3. Discrete function representation (DFR)	114
2.1.4. Virtual space method	116
2.1.5. Combined geometric element method	116
2.2. Composite approach	116
2.3. Other approaches.	118
3. DEM Models for non-spherical particles	118
3.1. Equations of motion of particles	118
3.2. Force calculation schemes	121
3.2.1. Contact forces between particles	121
3.2.2. Particle-fluid interaction forces	126
4. Fluid-particle coupling scheme	130
4.1. Computational sequence	132
4.2. Averaged volume method	133
4.2.1. Determination of flow projected area.	134

* Corresponding author at: Key Laboratory of Energy Thermal Conversion and Control of Ministry of Education, School of Energy and Environment, Southeast University, Nanjing 210096, P.R. China.

E-mail address: wqzhong@seu.edu.cn (W. Zhong).

4.2.2. Determination of porosity	135
4.3. Immersed Family Methods	137
4.3.1. Immersed boundary method	137
4.3.2. Direct numerical simulation	139
5. Applications	140
5.1. Particle packing and sandpile formation	140
5.2. Particle flow	143
5.2.1. Hopper discharge	143
5.2.2. Rotating drum	143
5.2.3. Other applications	143
5.3. Particle-fluid flow	144
5.3.1. Fluidized bed	144
5.3.2. Pneumatic conveying and channel flow	144
5.3.3. Other applications	145
6. Challenges and future research	145
7. Summary	146
Acknowledgements	147
References	147

1. Introduction

1.1. Description of non-spherical particulate system

A non-spherical particulate system (NSPS) is an assembly of non-spherical particles [1]. Such systems are very common and diverse in nature, industries and our daily life, as seen in Fig. 1, containing multifarious non-spherical particles varying from irregularly shaped rocks in macroscale to elongated airborne particles and/or oblate red blood cells in blood vessel in microscale. It is believed that at least 70% of the raw materials consist of non-spherical particles in modern industries such as pharmaceuticals [2–5], agriculture [6–12], energy [13–17], mining [18–20], environment [21–28] and geological engineering [29,30]. Understanding the fundamentals generally governing the behavior of

non-spherical particulate systems is of great importance to reduce, if not eliminate, the damages from natural disasters and improve the design and control of many industrial processes.

Particle shape, which often determines the microstructure of a granular material, is one of the most important primary parameters to control the macroscopic behavior of NSPS. The dynamics of non-spherical particles are significantly more complicated than those of spherical particles in many processes such as packing [31], compaction [32], conveying [33] or fluidization [34], because the geometrical contact scenarios are far more diverse between a non-spherical particle and its neighbors or walls, as well as the interactions between particles and surrounding fluid. For example, angular particles (e.g., elongated and flattened ones) are likely to interlock each other to form solid-like assemblies, exhibiting stronger resistance to shear than smooth spheres [35]. On



Fig. 1. Various non-spherical particulate systems in nature and industry.

the other hand, industrial processes are often operated under complicated conditions to realize different outcomes, which add significant complexity to the issue. Typical examples include rotary kiln, blast furnace, fluidized and spouted beds, where non-spherical particles undergo complicated translations, rotations, deformations, wear, adhesion, aggregations, breakages, and so on, all of which are very difficult to predict, further to the fact that the thermochemical behaviors are not even considered. Clearly, the complexity arising from a combination of microscale particle characteristics and macroscale technological requirements pose significant challenges to control NSPS. It requires in-depth understandings of underlying mechanisms of NSPS, of which the most essential one is the detailed microdynamic information at the particle or sub-particle scale.

Many experimental and numerical efforts have been made to elucidate the fundamentals of NSPS. Particle-scale investigations have been recognized as necessary in this regard. Computational techniques, such as Monte Carlo method, cellular automata and discrete element method (DEM), have been generally accepted as powerful tools for such studies [36,37]. In particular, DEM, which can describe the relationships between micro- and macroscopic properties of particulate matter by considering the shapes and properties of individual particles and forces acting on them, has attracted increasing attention. Indeed, it has been considered as one of the most promising approaches in the study of NSPS in the recent decades [36–40].

1.2. DEM modelling on non-spherical particles

The soft-sphere DEM originally developed by Cundall and Strack [41] has been used worldwide to study various particulate phenomena in the past several decades [36,37]. In this approach, the overlap between particles is considered to represent the particle deformations in the vicinity of the contacting surfaces, which is then used to calculate the elastic, plastic and frictional contact forces between contacting elements, while the particle motion is described by the Newton's second

law of motion. This straightforward and delicate treatment has achieved enough success in addressing applications of spherical particles [36,37]. However, for more complicated systems containing a large number of non-spherical particles, the application of DEM still faces some significant challenges.

As discussed above, NSPS in industrial or engineering applications are often complex in their physical structures and operating conditions, in addition to the fact that they have various particle properties. A typical example, biomass fluidized-bed gasifier (BFBG), is illustrated in Fig. 2. The high-velocity fluidization gas and gasification agent (air and steam) flow from the reactor bottom and passes through a bed of solid particles. Intense interactions between gas and solids result in strong disturbances with a number of bubbles being formed in the bed. The particle bed consists of a mixture of rod-like biomass particles and spherical fluidizing medium, and the volume fraction of particles in the bottom zone is extremely high (>40%). To deal with this type of a complicated dense and multi-shape particle-fluid system via the DEM approach, following issues must be addressed:

- (1) Object representation and the corresponding contact detection Object representation is fundamentally important for accurately describing particle behaviours, because DEM requires detailed information of individual particle-to-particle contacts for the evaluation of contact forces and torques [41–43]. The nature of the shape representation for a particular body controls not only the accuracy of the geometrical modelling of each particle, but also the type, accuracy and efficiency of the relevant contact detection algorithm [38–40,44]. In principle, it is theoretically possible to construct particles of arbitrary shapes; the essential difficulty lies in providing the efficient contact detection algorithm for a given set of particle shapes. Generally, more than 80% of the computational time is spent on detecting contacts and calculating the geometric details of the contact regions [45], and this proportion depends strongly on the actual particle

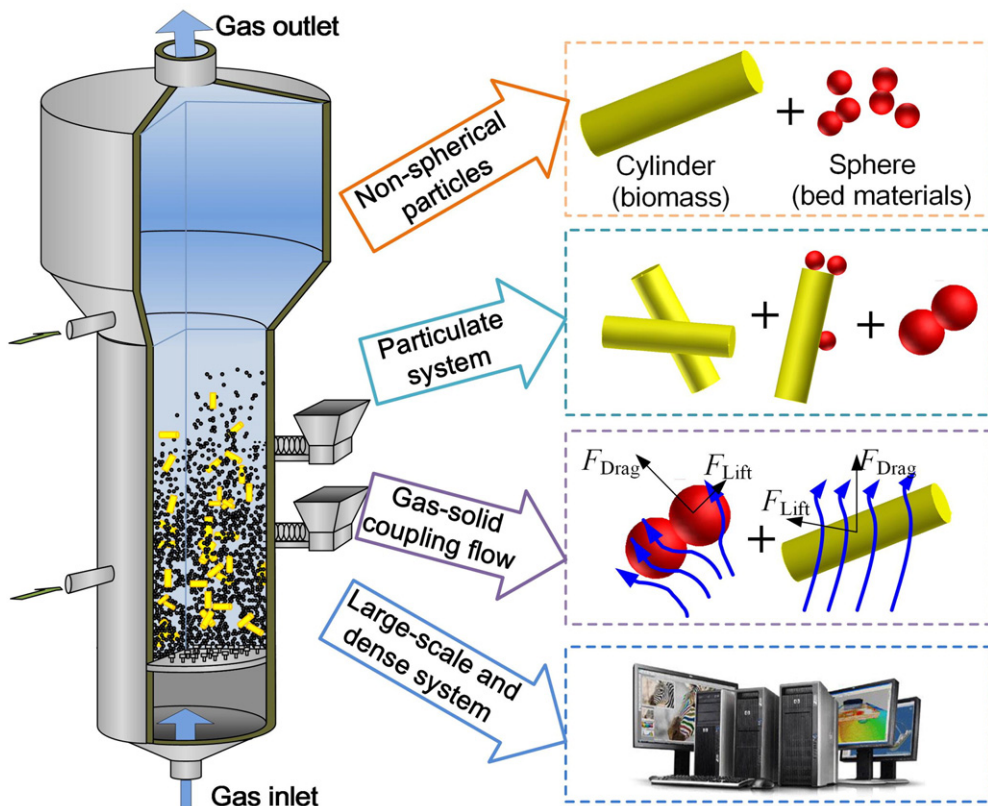


Fig. 2. A typical dense and multi-shape particle-fluid system: biomass fluidized bed gasification.

shape. It should be noted that the accurate object representation and efficient contact detection method are the crucial steps needed for correctly simulating NSPS.

(2) Calculation method of contact force

Contact force is one of the most noticeable outcomes of interactions between particles in a granular system. In DEM, when constructed particles make contact with each other, they do not change their shapes near the contact points; instead, they are considered to have interpenetrating or overlapping surfaces, and the amount of the overlap for each particle is taken as the contact deformation [37,41,45]. However, quite different from spherical particles whose contact forces have been accurately evaluated based on a simple overlap distance using the Hertz theory or others, the contact forces of non-spherical particles strongly depend not only on the overlap area or volume, but also on the specific geometrical configuration of the overlap region, both of which being very difficult to determine in numerical simulations. What makes the matter worse is that, the mathematical relationships between the contact force and overlap under various scenarios are still not well established for non-spherical particles. The direction of the normal at the contact point and coordinates of the reference contact point for non-spherical particles are still widely debated issues.

(3) Description of interactions between particles and fluids

When a fluid is introduced into a NSPS, the interaction forces between particles and fluid become another important factor that governs the motion of particles. The particle-fluid interaction force for non-spherical particles is significantly complex. The traditional empirical formulas for spherical particles in fluids may fail in a NSPS because the force can be strongly influenced by the shape, size, orientation and concentration of non-spherical particles, in addition to the physical and rheological states of the fluid medium and wall effects. Therefore, it could be very difficult to develop a general mathematic expression to describe the particle-fluid interactions such as the drag force or lift force, for such a complex system. Furthermore, it is still arguable how one should choose a proper parameter to represent particle shapes that significantly deviate from a spherical shape. For example, for the rod-like biomass particles mentioned above, the popular sphericity has been proved to fail to cover the features of the shape [46].

(4) Fluid-solid system with multi-shape particles

A practical granular or particulate system often contains particles of different shapes. For example, in the typical BFBG, one finds two entirely different particle types, namely, the coarse rod-like biomass particles and fine spherical medium particles, in the same chamber. Situations like this make considerable computational demands on DEM. For all of the aforementioned problems, such as the object representation, calculation of contact forces, description of gas-solid interactions, one must explore solutions which are not only accurate and efficient, but also as general as possible. For example, in the case of BFBG, a general and accurate algorithm is needed to simultaneously deal with the contact forces between pairs of cylinders, spheres and cylinder-sphere particles, which form three completely different contact scenarios. A universal contact detection method is essential for simulating the dynamics of arbitrary non-spherical particles in a system. Clearly, the generality of the solutions to the contact detection equations, as well as the calculation of forces, will leave us with multiple challenges when there are significant shape differences between particles.

(5) Limitation of computational capacity

To simulate a large-scale particle-fluid system with densely-packed multi-shape particles as in a BFBG, DEM faces huge challenges from the perspective of computing capacity and resources. Compared to other numerical methods, DEM is computationally

expensive because it needs to store and update many instantaneous details of every particle, identify collisions among particles and calculate the contact forces. The computational cost dramatically increases with the number of particles and the complexity of particle shapes. In real industrial systems, the number of particles often exceeds 10^9 and different shapes are involved. When the gas and liquid phases are taken into account, the computational efforts will be further increased heavily sharply. This significantly large amount of computations required for simulating NSPS strictly demands the DEM codes and algorithms to be efficient and computing capacity to be powerful.

1.3. Scope of this work

With rapid advancements in computer technology and theoretical development, non-spherical modelling has become a hot research area for DEM modelling as shown in Fig. 3. DEM modelling for non-spherical particle systems has been recently reviewed by Lu et al. [38]. The review covers advances in the non-spherical particle models, which include shape representation algorithms and efficient detection of contacts, and it also covers the main applications in granular systems containing non-spherical particles, spanning both static and dynamic systems. However, the review does not cover either the force models related to fluid-particle interactions or the coupling methods between CFD (Computational Fluid Dynamics) and DEM for non-spherical particles. This knowledge is vital in the application of non-spherical modelling in particle-fluid multiphase flows, and therefore, a comprehensive review is necessary.

The aim of this article is to extensively review the theoretical developments and applications of DEM modelling in NSPS. Firstly, this review summarises the representations and contact detection methods of non-spherical particles. Secondly, the equations of particle motion and models for contact forces between particles and interaction forces between particles and fluid are comprehensively reviewed. Thirdly, CFD-DEM coupling methods, including the averaged volume method (AVM) and immersed family methods (IFM) are reviewed. Fourthly, the applications of non-spherical modelling in packing, particle flows and particle-fluid flow systems are reviewed and the main findings were discussed in some detail. Finally, the main challenges DEM currently faces and the interesting research topics for future studies are discussed. We conclude that the non-spherical modelling has a bright future as it offers a new way of understanding industrial processes

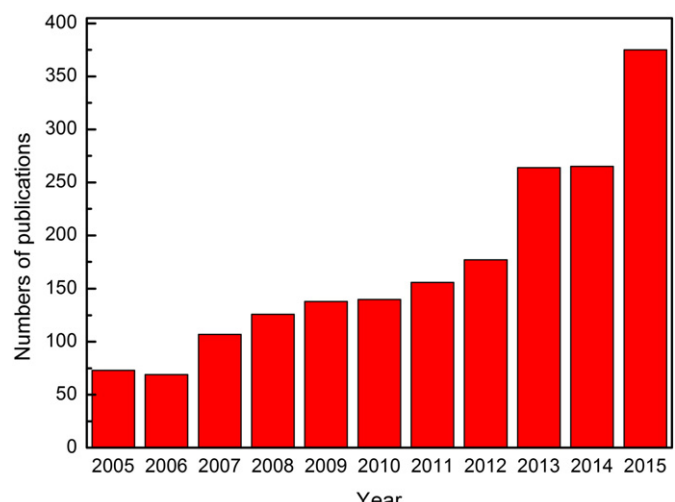


Fig. 3. Number of publications obtained from Science Direct using the key words: 'discrete element method/DEM' and 'non-spherical'.

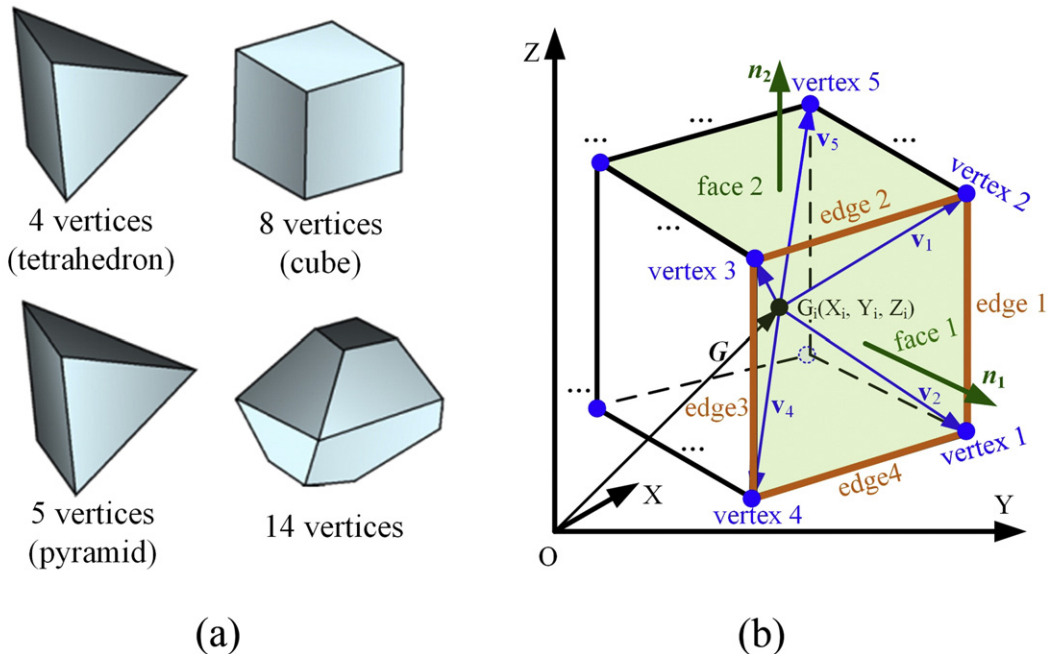


Fig. 4. Particle represented by polyhedrons: (a) typical particles constructed by polygon/polyhedron method [71]; (b) The geometric representation of a polygonal particle.

and/or phenomena with practical particle shapes, although there are still some aspects that are needed to be investigated in the future. It should be noted that when the overall particle density is sufficiently low, the granular medium can be regarded as fluid- or gas-like, which is not a point for consideration in this review.

2. Representation of non-Spherical particles and contact detections

Although few attempts have been made to explore a general contact detection algorithm independent of the object representation [44,47, 48], until now, particle representation and contact detection have been considered to be inextricably linked. It has been one of the hotspots and challenges in previous researches to find a flexible description which can not only construct particles with arbitrary shapes but also provides a robust and efficient contact detection method. Efforts to explore new or more efficient contact algorithms for the existing particle representation approaches are also important. Relentless attempts have been made in the past several decades, and the major achievements are discussed below in detail.

In this section, the object representation methods are classified into two groups: the single-particle method and composite-particle

approach. It should be noted that the contact detection processes discussed in the following section will focus only on the stage of contact resolution, and that the spatial sorting [43,45,49] has already been carried out to identify the pairs of objects in possible contact by using the previous algorithms, independent of the shape descriptors.

2.1. Single-particle method

2.1.1. Polygons and polyhedrons

Initially introduced to DEM by Cundall [41], polygonal and polyhedral body shapes in Fig. 4 have developed into the most interesting approaches to represent the realistic particles in soil and rock mechanics applications [48,50–66]. The geometry of a polygonal/polyhedral particle is defined in terms of corners, edges and faces (in 3D) as shown in Fig. 4(b). The locations of corners are specified by a series of vectors from the center of mass and a unit outward normal vector is associated with each face. The location of each polygon/polyhedron in the space is defined by the components of a vector to the center of gravity (with respect to a fixed reference frame).

There exist a number of algorithms for the contact detection between two polygons or two polyhedrons [44,47,67–69] and the most

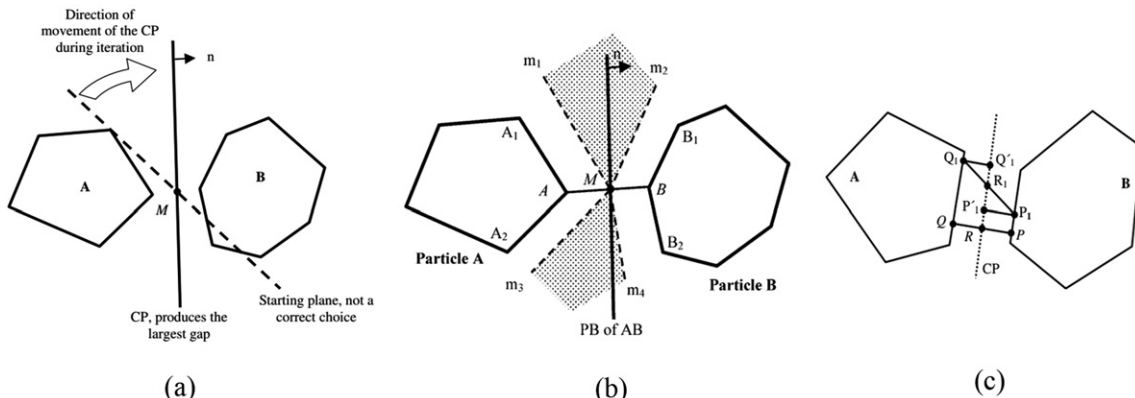


Fig. 5. Algorithms to find a common plane: (a) the conventional iterative algorithm [70,71]; (b) the fast common plane (FCP) algorithm [71] and (c) Shortest Link Method (SLM) [72].

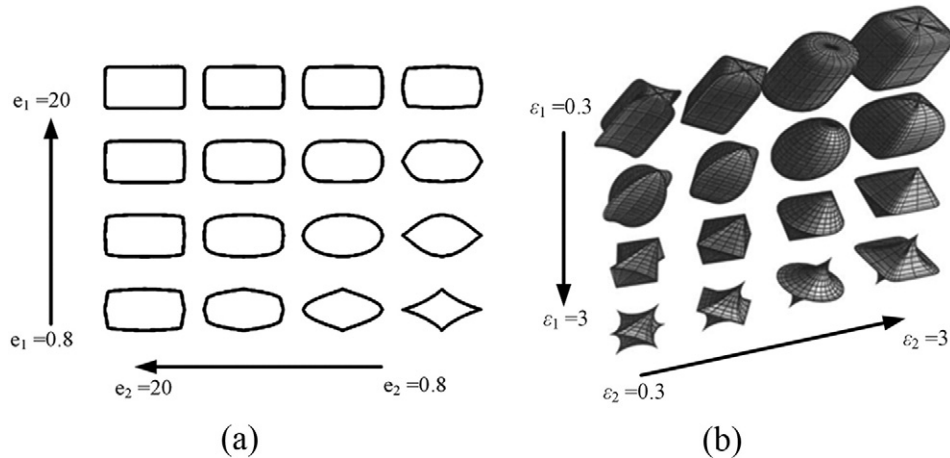


Fig. 6. Continuous functions representations (CFR) [40]: (a) 2D: $f(x, y) = \left(\frac{x}{a}\right)^{e_1} + \left(\frac{y}{b}\right)^{e_2} - 1$, e_1, e_2 range from 0.8 to 20; (b) 3D: $f(x, y, z) = \left(\left(\frac{x}{a_1}\right)^{2/e_2} + \left(\frac{y}{a_2}\right)^{2/e_2}\right)^{e_2/e_1} + \left(\frac{z}{a_3}\right)^{2/e_2} - 1$, e_1, e_2 range from 0.3 to 3.

well-known one is based on the concept of “Common Plane (CP)” [70]. The CP is introduced to bisect the space between the two contacting particles, simplifying the expensive particle-to-particle contact detection to a much faster corner-to-plane contact detection problem and provides a robust technique for obtaining the direction of the normal contact force, i.e. the line perpendicular to the CP. The crux of the difficulty for the CP method is to explore a fast and efficient algorithm to locate and move the CP. Useful algorithms to find the CP are the iterative algorithm [70], fast common plane (FCP) algorithm [71], quick updating algorithm [70] and the shortest Link Method (SLM) [72] as shown in Fig. 5.

The main limitation of the polygonal and polyhedral representations is that smooth shapes cannot be easily reproduced unless a large number of corners and edges are introduced, or other elements are incorporated. But inevitably, this would lead to a dramatic increase in the computational cost of contact detection. However, this problem can be fortunately avoided in the area of rock mechanics, where the objects are intrinsically polygonal or polyhedral.

2.1.2. Continuous function representations

Continuous functional representation (CFR) can be used to model smooth non-spherical particles, such as ellipses [73,74], 2-D superquadric curves [75–79], ellipsoids [8,74,80–91] and 3-D superquadrics [32,58,69,75,79,86,92–103]. The surfaces of such bodies are generally described implicitly with a function $f(x, y)$ in 2D cases, or $f(x, y, z)$ in 3D cases [49,79], which are as given below, respectively:

$$f(x, y) = \left(\frac{x}{a}\right)^{e_1} + \left(\frac{y}{b}\right)^{e_2} - 1 \quad (1)$$

or

$$f(x, y, z) = \left(\left(\frac{x}{a_1}\right)^{2/e_2} + \left(\frac{y}{a_2}\right)^{2/e_2}\right)^{e_2/e_1} + \left(\frac{z}{a_3}\right)^{2/e_2} - 1 \quad (2)$$

The specific particle shapes illustrated by Eqs. (1) and (2) are shown in Fig. 6.

The CFR appears to be very attractive with a drastic improvement in the accuracy of simulations by using super-quadric particles instead of circular elements for representing sand particles under quasi-static compression [104] and also in some other cases [86,92,96–98, 100,101,103]; nevertheless, to date only symmetric particles have been realized, and the CFR still faces considerable challenges to model arbitrary irregular particles, although it is believed that 80% of shapes of solids can be represented by superquadrics, and other shapes of solids can be derived from superquadrics in higher-dimensional hyperquadrics [105].

Direct contact detection and overlap evaluation between two superquadrics shapes can be obtained by resolving the intersection of the two functions, analytically or iteratively, as shown in Fig. 7(a), but the non-linearity of these equations makes it quite computationally expensive and even impractical [40,106,107], especially in 3D cases or when the squareness of the particles is increased [93,107], and there will also be some errors in the determination of the contact normal [80]. Relatively the indirect methods in Fig. 7(b) and (c) are quite efficient and promising, for example, the geometric potential method [39, 108,109], the common normal algorithm [80] and so on. In fact, with the exception of ellipses, the intersection between two superquadric

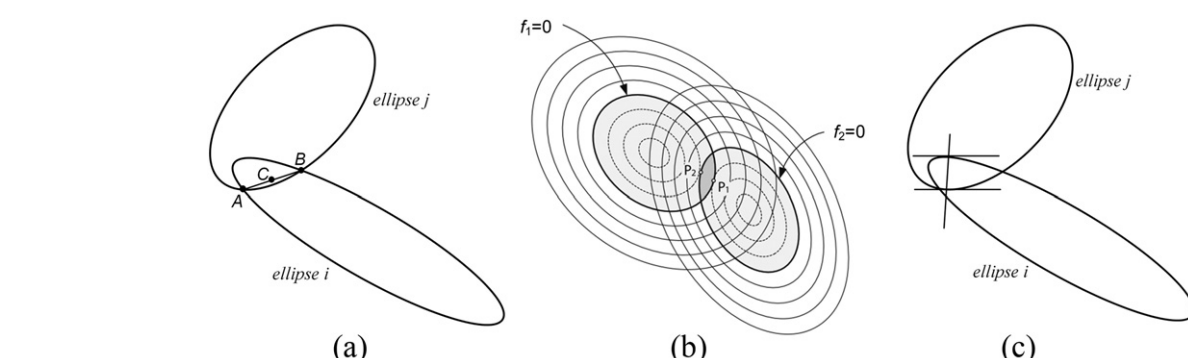


Fig. 7. Contact detection of two ellipses according to [39]: (a) the intersection algorithm; (b) the geometric potential algorithm; (c) the common normal concept.

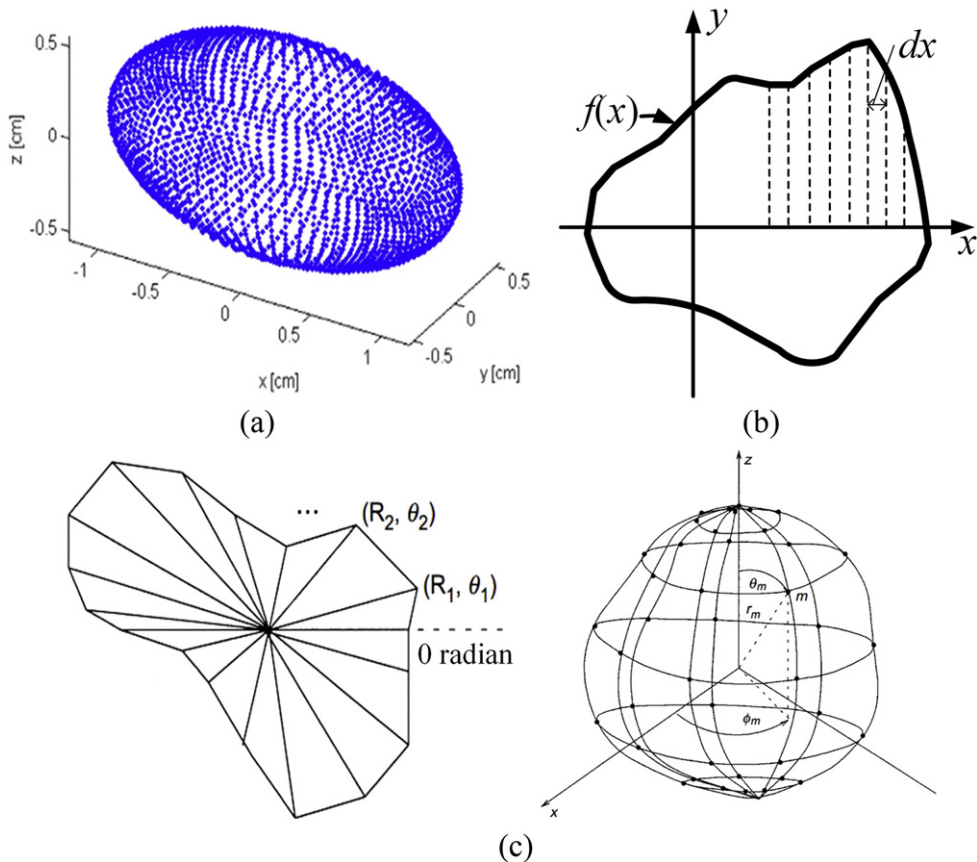


Fig. 8. Typical examples of DFR: (a) a discretised representation of an implicit function (superellipsoid) [58]; (b) a discretised representation of a single-valued boundary function $y=f(x)$ [40]; (c) the polar descriptor in 2D (left) case with each node defined by a radius and angle, and 3D (right) case with the coordinates of node m given as (r_m, θ_m, ϕ_m) [40].

particles is usually obtained by discretizing the surface of one body and then checking each point on it against the implicit function representing the other body [40,49,75], which has been further developed to be the so-called discrete function representation.

2.1.3. Discrete function representation (DFR)

DFR was defined to represent a particle shape by an array of boundary nodes with some specific associated information [110]. Some typical examples are: a discretised representation of implicit functions [40,49, 58,75,107] (see Fig. 8(a)), a discretised representation of a body boundary function as shown in Fig. 8(b) [40,110], and the polar descriptor in Fig. 8(c) [40,43]. In DFR, the surface of a body is discretised into a

grid of nodes using a certain criterion (for example, the uniform discretization or adaptive discretization [38,107], a fixed grid intervals of dx [40,110], or a parameter group including a radius r_m and two angles, θ_m and ϕ_m [40,43]), providing us an ordered set of points, which can be searched fast.

For efficient contact detection, a search usually starts by narrowing the search space to a minimum region where the contact may occur. Bounding spheres or bounding boxes are usually used as a first approximation of the particle shapes for narrowing the search space [40,110]. Once an overlap is detected at this stage, the corresponding shapes need to be refined, and the search is next confined to the overlapping area between the bounding geometries. Each

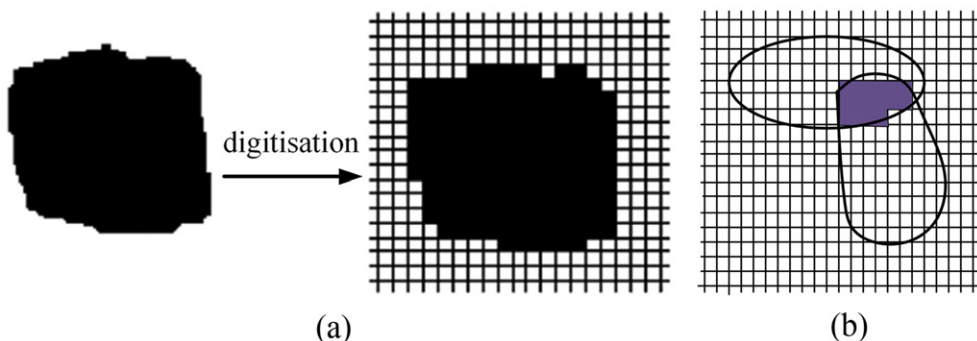


Fig. 9. Particles in the virtual space: (a) digitization of a real object (b) the overlap of two particles [39,111].

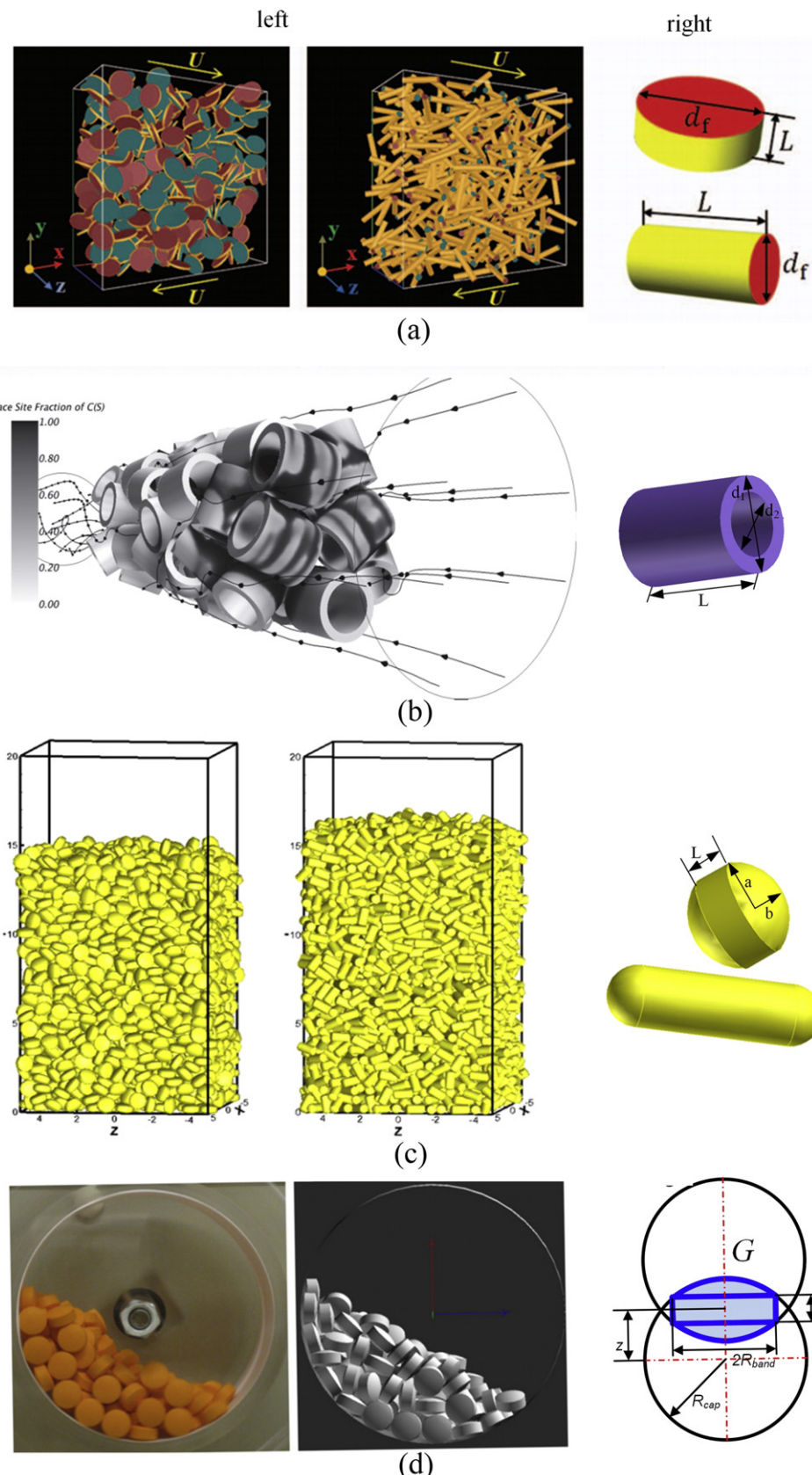


Fig. 10. particles constructed by combining geometric elements: (a) DEM simulations of granular shear flows (left) with flat disks and elongated rods (right) represented by a cylindrical bond and two end surfaces [35], (b) DEM simulation of methane gas through a fixed bed (left) with one-hole cylinders (right) represented by two cylindrical bond and two end annuluses [121], (c) DEM simulations of packing behaviors (left) of spherocylinders (right) represented by a cylindrical bond and two curved end surfaces [44], (d) Experimental and DEM simulation of a rotating drum (left) with bi-convex tablets (right) represented by two spheres and a cylinder [125].

node of a particle j belonging to this region is transformed to the system of local coordinates of particle i , and then a test is done to determine if the node lies inside particle i . The detailed operations can be found in references [40,110].

It is clear that the accuracy of the contact detection considerably depends on the number of nodes and their distribution on the particle surface in the DFR approach [38,107]. It is an average rather than the true contact normal that is usually calculated due to lack of coincidence of nodes on contacting bodies [106]. The particle shape is also believed to affect the efficiency which is quite low when dealing with large aspect ratios [40].

2.1.4. Virtual space method

Another potential approach to describe a particle of arbitrary shape in space is based on digitization [111]. In this approach, a space is digitized and mapped onto discrete cells named “virtual space”, and an arbitrary shape is just a coherent collection of pixels (in 2D) or voxels (in 3D), as illustrated in Fig. 9(a). These pixels are stored in a computer and manipulated as integers or bits. Once the resolution is assigned, the computational cost depends only on the area (in 2D) or volume (in 3D) of the shape, instead of its increase with the complexity of the shape. The real shapes can be reproduced directly from the digital images obtained by scanning real particles using 3D optical and X-ray scanners. Since both the particles and space are digitized, particles movements are consequentially digitized. As a result, collision and overlap detection is now a simple matter of detecting whether two objects occupy the same site(s) at a given time, shown as Fig. 9(b), without having to compute and test intersections between objects [39,111–113]. This straightforward contact detection is the simplest, and on the basis of this method, it is very easy to develop other methods, for example, the so-called Orientation discretization database solution [39,44,111].

2.1.5. Combined geometric element method

The surface of an arbitrary particle can be represented by a group of geometric elements, such as planar or curved surface segments, with edges and/or vertices at the positions where the surface is not continuous. This combined geometric element method is suitable for constructing regular particles with smooth surfaces and obvious edges, some examples being perfect cylinders [35,44,114–121], hollow cylinders [121], spherocylinders [44] and bi-convex round tablets [122–125] as shown in Fig. 10. In the case of a perfect cylinder, its surface is simply

composed of a cylindrical surface and two flat ends. However, for this seemingly simple particle, the contact detection algorithm must consume a relatively large amount of computational resources because it is needed to store and update a large amount of information related to the vertexes, edges and faces during simulations, and a cumbersome process is required to judge every possible type of contacts between two particles, e.g., vertex-to-edge, edge-to-edge, edge-to-face, face-to-face and so on [120]. To speed up the contact detection, Guo et al. [120] suggested performing, as the first step, a coarse contact detection search in which the cylindrical particle is divided into a number of elements that are subsequently approximated by circumscribing spheres or boxes of each element. To locate the contacts between neighboring cylinders, the circumscribing boxes are mapped onto the background domain, as illustrated in Fig. 11. Subsequently, the lattices with which these circumscribing boxes are intersecting are identified. Only the particles with the circumscribing boxes that occupy the same lattice are subjected to further contact checks.

2.2. Composite approach

In the past decades, many attempts have been made to create composite particles by combining simple geometries [126–132]. To date, the most efficient composite approach has been mainly the multi-sphere model (MSM), which was introduced by Favier et al. [106] and Abbaspour-Fard [16].

In the multi-sphere model, an arbitrary particle can be approximated by a certain number of spheres with various amounts of overlaps, as shown in Fig. 12(a). Once a model particle is created, the relative distances between the elemental spheres will remain fixed during the simulation, and the generated particle acts as a rigid body. This shape representation shows efficient contact detection because it employs the well validated sphere-sphere contact detection algorithm rather than introducing any new mechanics. The multi-sphere model has been used efficiently in many applications such as simulating gravel deposits [133], bio materials [6,11,13,15,16,118,134–140], pharmaceutical tablets [2–5], industrial particles [20,58,61,83,117,141–156], and so on; especially it holds an advantageous position for simulating the mixing processes involving particles of very different shapes [11,157].

However, this approach has achieved only a limited success, because there are still numerous practical difficulties in determining the optimal number of spheres as well as their sizes and locations, so that not only

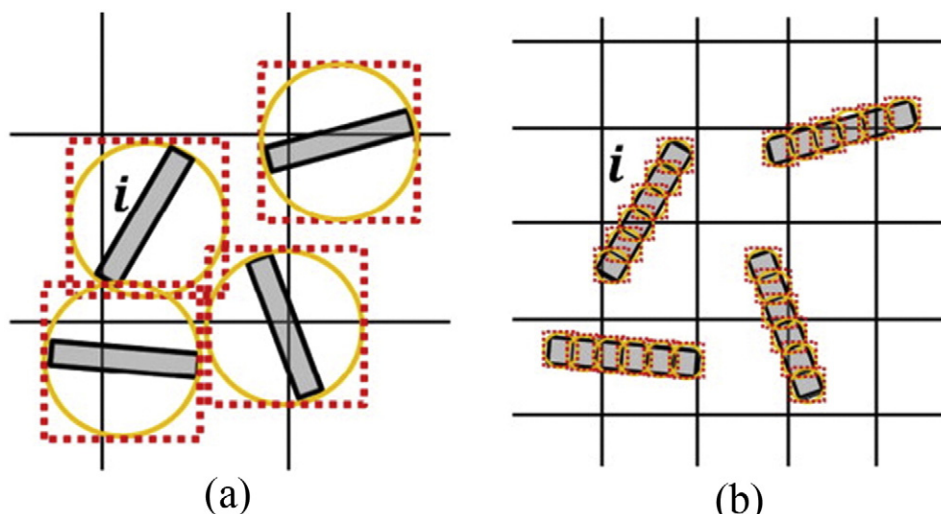


Fig. 11. The mapping scheme of large aspect ratio particles on the background mesh based on (a) the whole particle, (b) the elements [120].

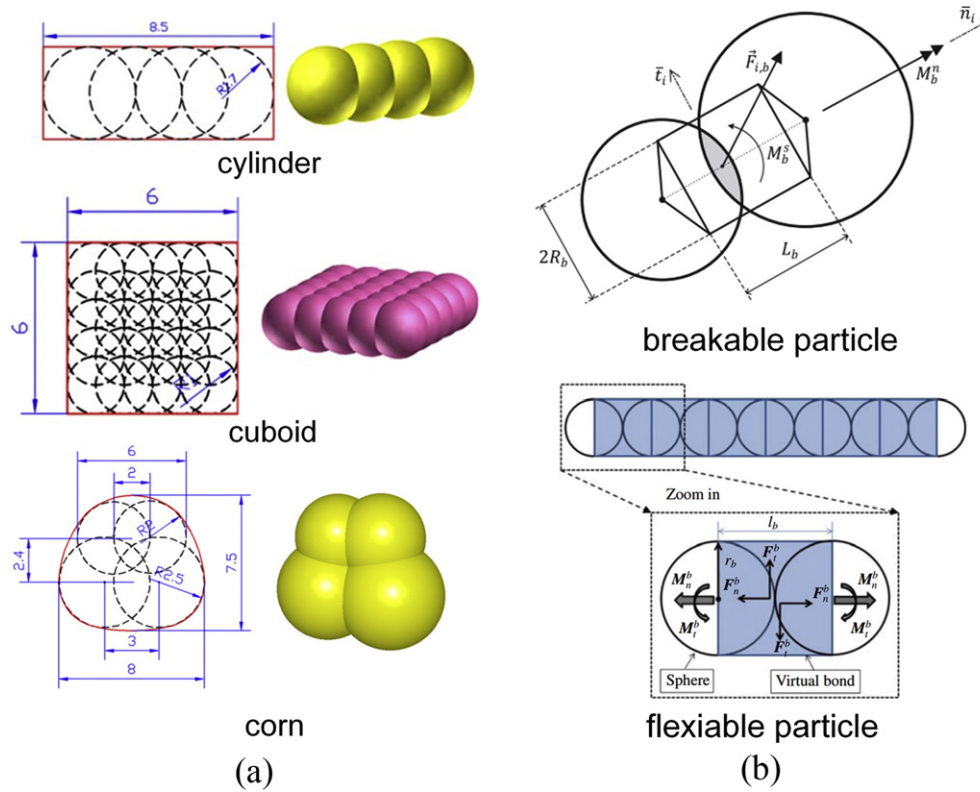


Fig. 12. Various non-spherical particles constructed with multi-sphere model [6,11,15,135,136]; (b) the bonded model [167–169].

Table 1
Equations of normal direction contact force.

Force model	Equations
Elastic repulsion force	
Linear models	$\mathbf{F}_{n,ij,elastic} = K_{n,ij}\delta_{n,ij}\mathbf{n}_{ij}$ $\mathbf{F}_{n,ij,dynamic} = K_{n,ij,dynamic}\delta_{n,ij}\mathbf{n}_{ij}$
Non-linear models	$K_{n,ij,dynamic} = \alpha K_{n,ij,static}; K_{n,ij,static} = \frac{\pi E_i E_j}{2(E_i + E_j)}$ $\mathbf{F}_{n,ij,elastic} = \frac{4}{3} \frac{E_i E_j}{E_i(1-\sigma_j^2) + E_j(1-\sigma_i^2)} \sqrt{R_{ij}} \delta_{n,ij}^{3/2} \mathbf{n}_{ij}$
Models with hysteresis	$\mathbf{F}_{n,ij,elastic} = K_{n,ij}\delta_{n,ij}\mathbf{n}_{ij}; K_{n,ij} = \text{constant}$ $F_{n,ij,elastic} = \begin{cases} K_1 \delta_{n,ij} & \text{for loading} \\ K_2 (\delta_{n,ij} - \delta_{n,ij,max}) & \text{for unloading} \end{cases}$ $e = \sqrt{\frac{K_1}{K_2}}, K_2 = K_1 + S \mathbf{F}_{n,ij,elastic} $ $\mathbf{F}_{n,ij,L} = K_{n,ij,L} \delta_{n,ij}^p \mathbf{n}_{ij}^p \quad \text{for loading}$ $\mathbf{F}_{n,ij,L} = K_{n,ij,U} \delta_{n,ij}^{p+q} \mathbf{n}_{ij}^{p+q} \quad \text{for unloading or re-unloading}$ $\mathbf{F}_{n,ij,L} = \beta \mathbf{F}_{n,ij,L} + (1-\beta) \mathbf{F}_{n,ij,U} \quad \text{for re-loading}$ $q = (A \cdot \delta_{max})^2, \beta = \frac{\delta - \delta_{min}}{\delta_{max} - \delta_{min}}$ $\mathbf{F}_{n,ij,elastic} = \begin{cases} -K_{n,ij} \delta_{n,ij}^{3/2} \mathbf{n}_{ij} & \delta \geq 0 \wedge \delta < \delta_y \\ -(K_{n,ij} \delta_{n,ij}^{3/2} + \pi \cdot p_y \cdot R_{ij} (\delta - \delta_y)) & \delta \geq 0 \wedge \delta \geq \delta_y \\ -K_{n,ij} (\delta - \delta_{max}) & \delta < 0 \end{cases}$ $K_{n,ij} = \frac{4}{3} \frac{E_i E_j}{E_i(1-\sigma_j^2) + E_j(1-\sigma_i^2)} \sqrt{R_{ij}}$
Continuous interaction models	$\mathbf{F}_{n,ij} = -\frac{\partial V}{\partial \mathbf{x}_{ij}}$ $V = \begin{cases} \mathcal{E} \left[\left(\frac{d}{x_{ij}} \right)^{12} - \left(\frac{6}{x_{ij}} \right)^6 + \frac{1}{4} \right] & \text{if } x_{ij} < r_c \\ 0 & \text{otherwise} \end{cases}$ $r_c = 2^{1/2} d$ $V = \begin{cases} \mathcal{E} \left(\frac{d}{x_{ij}} \right) & \text{if } x_{ij} < r_c \\ 0 & \text{otherwise} \end{cases}$ $\varepsilon = \frac{dmg}{a}, a = 36, r_c = 1.8d; a = 36, r_c = 1.2d; \text{ or } a = 36 \text{ and } 144, r_c = 1.2d$
Energy dissipation in the normal direction of contact (viscous dissipation)	Linear models $\mathbf{F}_{n,ij,viscous} = -\gamma_{n,ij} m_{ij} \mathbf{v}_{n,ij}$ $m_{ij} = \frac{m_i m_j}{m_i + m_j}$
	Non-linear models $\mathbf{F}_{n,ij,viscous} = 2 \frac{E_i E'_j}{E_i(1-\sigma_j^2) + E'_j(1-\sigma_i^2)} \sqrt{R_{ij}} \delta_{n,ij} \mathbf{v}_{n,ij}$ $E'_i = \frac{9\xi_i \eta_i}{3\xi_i + \eta_i}, O'_j = \frac{3\xi_i - 3\eta_i}{2(3\xi_i + \eta_i)}$ $\mathbf{F}_{n,ij,viscous} = c_{n,ij} (8m_{ij} \frac{E_i E'_j}{E_i(1-\sigma_j^2) + E'_j(1-\sigma_i^2)} \sqrt{R_{ij}} \delta_{n,ij})^{1/2} \mathbf{v}_{n,ij}$

Table 2
Equations of tangential direction contact force.

Model	Expressions
Complex models	$\mathbf{F}_{t,ij} = -t_{ij} \min(\mathbf{F}_{t,ij,static} , \mathbf{F}_{t,ij,dynamic})$ $\mathbf{F}_{t,ij,dynamic} = -\mu \mathbf{F}_{t,ij} \mathbf{t}_{ij}$ $\mathbf{F}_{t,ij,static} = \mathbf{F}_{t,ij,spring} + \mathbf{F}_{t,ij,dissipation}$ $\mathbf{F}_{t,ij,spring} = -k_{t,ij} \delta_{t,ij} \mathbf{t}_{ij}$ $k_{t,ij} = \frac{16}{G_i(2-\sigma_i) + G_j(2-\sigma_i)}$ $\text{or } k_{t,ij} = \text{const};$ $\mathbf{F}_{t,ij,dissipation} = -\gamma_i m_{ij} \mathbf{v}_{t,ij}$
Global models	$\mathbf{F}_{t,ij}(t + \Delta t) = \mathbf{F}_{t,ij}(t) + K_t(t) \Delta \delta_t(t)$ $K_t = \begin{cases} K_{t0} (1 - \frac{F_{t,ij} - F_{t,ij}^*}{\mu F_{t,ij} - F_{t,ij}})^a \Delta \delta_t \geq 0 \\ K_{t0} (1 - \frac{F_{t,ij} - (F_{t,ij}^*)^a}{\mu F_{t,ij} + F_{t,ij}}) \Delta \delta_t < 0 \end{cases}$ or $K_t = \begin{cases} K_{t0} (1 - \frac{F_{t,ij} - F_{t,ij}^*}{\mu F_{t,ij} - F_{t,ij}})^a \Delta \delta_t \geq 0 \\ K_{t0} (1 - \frac{F_{t,ij} - F_{t,ij}^*}{\mu F_{t,ij} + F_{t,ij}}) \Delta \delta_t < 0 \end{cases}$ $\text{with } K_{t0} = 5 \times 10^5 \text{ N/m, } a = 0.3; \text{ or } K_{t0} = 0.8 K_1, \text{ } K_1 = 10^6 \text{ N/m, } a = 0.3;$ or $K_{t,ij} = \frac{K_{t,ij}}{V} \sqrt{1 - \frac{F_{t,ij}}{\tan \varphi_i F_{n,ij}}}$ $\mathbf{F}_{t,ij} = -\mu \mathbf{F}_{n,ij} (\frac{\delta_{t,ij}}{\delta_{t,ij,0}} - \frac{\delta_{t,ij}}{\delta_{t,ij,0}}) \mathbf{t}_{ij}$ $ \mathbf{F}_{t,ij,0} \text{ or}$ $F_{t,ij} = \mu F_{n,ij} [1 - (1 - \frac{ \delta_{t,ij} }{\delta_{t,ij,0}})^{3/2}]$ $\delta_{t,ij,0} = C_t \mu F_{n,ij},$ $\text{If } \delta_{t,ij} > \delta_{t,ij,0}, \text{ then } \delta_{t,ij} = \delta_{t,ij,0}$ $\mathbf{F}_{t,ij} = -k \delta_{t,ij} \mathbf{t}_{ij} - \gamma \mathbf{v}_{t,ij}$ $\mathbf{F}_{t,ij} = -\gamma m_{ij} \mathbf{v}_{t,ij} - \text{sign}(\delta_{t,ij}) \min(k_t \delta_{t,ij}, \mu \mathbf{F}_{n,ij})$
Other models	

the shapes of real particles, but also their motion properties such as density distributions and moment of inertia can be accurately represented [143,158–163]. For example, surfaces generated by this approach are generally too “knobbly” [164]. To alleviate these undue surface irregularities of complex particles, a large number of spheres must be used to obtain an approximation to the real particles, which may however result in the non-uniform mass distribution and incorrect moment of inertia, as well as the loss of computational efficiency. Therefore, the applicability of multi-sphere method is usually limited to a few types of simple shapes [113], although several improved methods have been proposed in order to generate and assemble spheres more efficiently, typical ones among them being the optimized clustering method

[162], the dynamic method [163], the four-points-sphere-fitting methods [165], the sphere growing method [143,158,159], the modified greedy heuristic algorithm [166] and so on.

Apart from MSM, the bonded-particle model was proposed to bond spheres or other elements together and construct clusters with arbitrary shapes as shown in Fig. 12(b) [167–169]. Within these clustered bodies, elements are connected using bonds, and the relative movements of constituent elements may lead to a breakage or deformation of the bonds, which make the clustered particles breakable or flexible.

2.3. Other approaches

Apart from the conventional particle representations discussed above, some uncommon but promising methods have also been proposed, some examples being the so-called ‘racetrack particles’ [55,56,58,92,109,170–175], ‘potential particle’ [109,176,177], ‘Minkowski particle’ [178–181], ‘Booleana particle’ [182], and so on. However, most object representations and contact detection methods have their own strong preferences. For example, CFR and its contact detection are best suited for regular shaped particles with a smooth and continuous surface, but they are quite powerless for the particles with sharp edges and flat surfaces. The lack of versatility of the representation methods causes great difficulties in simulating particulate systems with mixtures of particles of different shapes. To address such issues, it is important to explore new and more general shape representation methods as well as generalized contact detection techniques. Already, impressive efforts have been made in developing generalized contact detection techniques for non-spherical particles, the typical ones being probability-based contact algorithm [47], GJK-based strategy [48] and Orientation Discretization Database Solution [44].

3. DEM Models for non-spherical particles

3.1. Equations of motion of particles

A particle in a granular flow can have two motion types, translational and rotational, which are governed by Newton's second law of motion as given below:

$$m_i \frac{d^2 \mathbf{x}_i}{dt^2} = m_i \mathbf{a}_i = \mathbf{F}_i \quad (3)$$

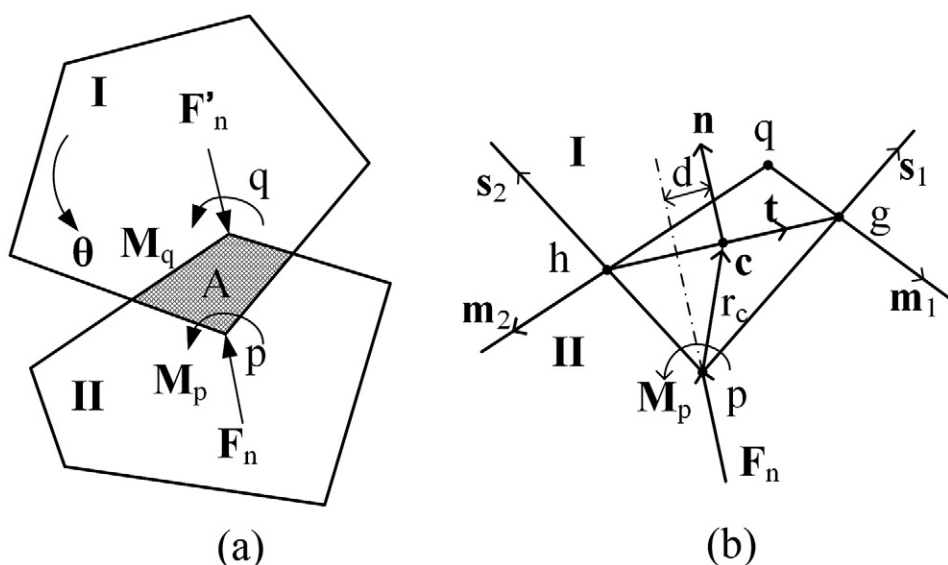


Fig. 13. Energy-based polygon to polygon normal contact model: (a) corner-corner contact of two polygons, and (b) normal contact model [202].

Table 3Expressions of C_D for non-spherical particles with fixed shapes.

Authors	Equations	Conditions
Clift et al. (2005) [216] Isaacs and Thodos (1967) [256]	$C_D = 9.689(\text{Re}_d)^{-0.78} + 1.42(\text{Re}_d)^{0.04}$ $C_D = 0.99(\rho_p/\rho_f)^{-0.12} E_l^{-0.08}$	$0.1 < \text{Re}_d < 5$ Cylindrical particles in the turbulent regime $E_l > 1$ $20 < \text{Re} < 6000$ Cones, cylinders, needles, disks, prisms, etc., in Newtonian and power law liquids
Agarwal and Chhabra (2007) [226]	$C_D = C_{D0} + \frac{A_c}{A_p} C_{D\infty} (C_{D0})^{2/3} k \left[\frac{6Xb}{6Xb + C_{D0}} \right]^\beta + C_{D\infty} \left[\frac{6Xb}{6Xb + 128C_{D0}} \right]^{11/12}$ $C_{D0} = \frac{24X}{\text{Re}}, C_{D\infty} = 0.44$ $X = 6^{(n-1)/2} \left(\frac{3}{n^2 + n + 1} \right)^{n+1}, a = \frac{3}{n^2 + n + 1}, b = \exp\{3(\alpha - , \ln 6)\}$ $k = \frac{3-\partial}{\partial a} \cdot \exp\left\{ \left(\frac{3-\partial}{\partial a} \right)^2, \ln 3 \right\}, \beta = \frac{11}{48} \sqrt{6} [1 - , \exp\left\{ \left(\frac{3-\partial}{\partial a} \right)^2, \ln \left(\frac{\sqrt{6}-1}{\sqrt{6}} \right) \right\}]$ $C_D = \frac{4}{3} \frac{\exp\{A_1 \text{Re}_p^{-1/B_1} + A_2 \text{Re}_p^{-1/B_2} + C\}}{\text{Re}_p^2};$	$10^{-5} < \text{Re} < 300$ $0.31 \leq n \leq 1$ $0.62 \leq \varphi \leq 0.86$ Cuboid with square base $0.05 \leq \text{Re}_p \leq 6300$
Wang et al. (2011) [270]	$A_1 = -0.00136, B_1 = 0.5656, A_2 = -2.938, B_2 = 12.32, C = 4.308$	Long cylinder
Clift et al. (2005) [216]	$C_D = \begin{cases} 9.689 \text{Re}^{-0.78} (1 + 0.147 \text{Re}^{0.82}) & 0.1 < \text{Re} \leq 5 \\ 9.689 \text{Re}^{-0.78} (1 + 0.227 \text{Re}^{0.82}) & 5 < \text{Re} \leq 40 \\ 9.689 \text{Re}^{-0.78} (1 + 0.0838 \text{Re}^{0.82}) & 40 < \text{Re} \leq 400 \end{cases}$	
Ren et al. (2011) [239]	$C_D = \frac{24}{\text{Re}_p} (1 + C_2 \text{Re}_p^{C_2}) + \frac{C_3}{1 + (C_4/\text{Re}_p)}$ $C_1 = 0.0005 \left(\frac{\rho_p - \rho_f}{\rho_f} \right)^{1.1687} \varphi^{4.7677} \left(\frac{d_a}{d_v} \right)^{6.5032}$ $C_1 = 0.6813 \left(\frac{\rho_p - \rho_f}{\rho_f} \right)^{-0.0534} \varphi^{-1.0632} \left(\frac{d_a}{d_v} \right)^{-1.5334}$ $C_3 = 0.6478 \left(\frac{\rho_p - \rho_f}{\rho_f} \right)^{-0.1328} \varphi^{-3.8035} \left(\frac{d_a}{d_v} \right)^{-3.3911}$ $C_4 = 22.4748 \left(\frac{\rho_p - \rho_f}{\rho_f} \right)^{-1.764} \varphi^{-1.1738} \left(\frac{d_a}{d_v} \right)^{5.1868}$	$500 \leq \text{Re}_p \leq 84945$ Cylinders $0.78 \leq d_a/d_v \leq 1.28$ $0.68 \leq \varphi \leq 0.87$

$$\mathbf{v}_i = \frac{d\mathbf{x}_i}{dt} \quad (4)$$

$$I_i \frac{d^2\theta_i}{dt^2} = I_i \mathbf{u}_i = \mathbf{T}_i \quad (5)$$

$$\mathbf{w}_i = \frac{d\theta_i}{dt} \quad (6)$$

where $m_i, \mathbf{v}_i, \mathbf{a}_i$ and \mathbf{x}_i are the mass, velocity, acceleration and position of the particle i , respectively, and $I_i, \theta_i, \mathbf{w}_i$ and \mathbf{u}_i are the moment of inertia, orientation vector (i.e., the angle between the principle axis of the particle and the inertial coordinate system), angular velocity and angular acceleration, respectively. \mathbf{F}_i and \mathbf{T}_i are the sum of all the forces and torques which are respectively given by:

$$\mathbf{F}_i = \mathbf{F}_{i,contact} + \mathbf{F}_{i,gravity} + \mathbf{F}_{i,fluid} + \mathbf{F}_{i,external} \quad (7)$$

Table 4General expressions of C_D for non-spherical particles.

Authors	Equations	Conditions
Haider and Levenspiel (1989) [223]	$C_D = \frac{24}{\text{Re}} (1 + A \text{Re}^B) \frac{C}{1 + \frac{B}{\text{Re}}}$ For spherical particles: $A = 0.1806, B = 0.6459, C = 0.4251, D = 6880.95$ For non-spherical particles: $A = , \exp(2.3288 - 6.4581\varphi + 2.4486\varphi^2)$ $B = 0.0964 + 0.5565\varphi$ $C = , \exp(4.905 - 13.8944\varphi + 18.42222\varphi^2 - 10.2599\varphi^3)$ $D = , \exp(1.4681 + 12.2584\varphi - 20.7322\varphi^2 + 15.8855\varphi^3)$ For isometric particle ($\varphi \geq 0.67$) $C_D = \frac{24}{\text{Re}} [1 + \{8.1716, \exp(-4.0655\varphi)\} \times \text{Re}^{(0.0964 + 0.5564\varphi)}] + \frac{73.69 \text{Re} \exp(-5.0748\varphi)}{\text{Re} + 5.378 \exp(6.2122\varphi)}$	$\text{Re}_d < 2.6 \times 10^5$
Ganser (1993) [249]	Isometric shapes $K_1 = [\frac{1}{3} + \frac{1}{3}\varphi^{-0.5}]^{-1}, K_2 = 10^{1.1814(-\log\varphi)^{0.5743}}$ Non-isometric shapes $K_1 = [\frac{d_a}{3d} + \frac{2}{3}\varphi^{0.5}]^{-1}, K_2 = 10^{1.1814(-\log\varphi)^{0.5743}}$	
Chien (1994) [250]	$C_D = \frac{30}{\text{Re}} + 67.289, \exp(-5.03\varphi)$	$0.2 \leq \varphi \leq 1$ $\text{Re} < -5000$
Hartman et al. (1994) [251]	$\log \text{Re}(Y, \varphi) = , \log \text{Re}(Y, 1) + P(Y, \varphi)$ $Y = C_D/\text{Re}$	
Hölzer and Sommerfeld (2008) [271]	$C_D = \left(\frac{8}{\text{Re}} \right) \frac{1}{\sqrt{\text{Co}_i}} + \frac{16}{\text{Re}} \frac{1}{\sqrt{\varphi}} + \frac{3}{\sqrt{\text{Re}}} \frac{1}{\sqrt{\varphi^3}} + 0.4210^{0.4(-\log\varphi)^{0.2}} \frac{1}{\varphi}$	Stokes region
Leith (1987) [272]	$C_D = \frac{8}{\text{Re}} \frac{1}{\sqrt{\text{Co}_i}} + \frac{16}{\text{Re}} \frac{1}{\sqrt{\varphi}}$	Stokes region
Ganser (1993) [249]	$C_D = 0.42 \cdot 10^{1.8148} (-\log\varphi)^{0.5743}$	Stokes region
Swamee and Ojha (1991) [273]	$C_D = \left[\frac{48.5}{(1 + 4.5\text{Co}^{0.35})^{0.8} \text{Re}^{0.64}} + \left\{ \left(\frac{\text{Re}}{\text{Re} + 100 + 100\text{Co}} \right)^{0.32} \frac{1}{\text{Co}^{1.8} + 1.05\text{Co}^{0.8}} \right\} \right]$ $\text{Co} = c/(ab)^{1/2}$	$0.3 < \text{Co} < 1$ $1 < \text{Re} < 10000$
Tran-Cong et al. (2004) [274]	$C_D = \frac{24}{\text{Re}} \frac{d_n}{d_A} \left[1 + \frac{0.15}{\sqrt{\text{Co}_i}} \left(\frac{d_A}{d_n} \text{Re} \right)^{0.687} \right] + \frac{0.42 \left(\frac{d_A}{d_n} \right)^2}{\sqrt{\text{Co}_i} [1 + 4.25 \times 10^4 \left(\frac{d_A}{d_n} \text{Re} \right)^{-1.16}]} \quad 0.8 < \frac{d_A}{d_n} < 1.50 \text{ and } 0.4 < \text{Co}_i < 1.0$	Cubes, rectangular parallelepipeds, tetrahedrons, cylinders and other shapes. $0.15 < \text{Re} < 1500$
Dioguardi and Mele (2015) [275]	$C_D = \frac{C_{d,sphere}}{\text{Re}^2 \varphi} \exp\left(\frac{\text{Re}}{1.1883}\right)^{\frac{1}{0.4826}}$ $, \exp\left\{ \begin{array}{l} \text{Re}^{-0.23} & 0 < \text{Re} < 580 \\ \text{Re}^{0.05} & 50 < \text{Re} < 10000 \end{array} \right.$	

Table 5

Shape factors for non-spherical particles.

Sphericity	ϕ	Ratio of the surface area of a sphere (with the same volume as the given non-spherical particle) to the surface of the non-spherical particle
Crosswise sphericity	ϕ_{\perp}	Ratio between the cross-sectional area of the volume-equivalent-sphere and the projected cross-sectional area of the particle perpendicular to the flow
Lengthwise sphericity	ϕ_{\parallel}	Ratio between the cross-sectional area of the volume
	d_n/d_A	Ratio between the diameter of the sphere with equivalent volume (d_n) and the diameter of the sphere having the same projected area
Particle circularity	c_{ir}	Ratio between the perimeter of the sphere having the same projected area and the projected perimeter of the particle in its moving direction
	$(d_{\max}/d_{\min})^m$	Dimensionless numbers based on the largest, intermediate and shortest particle axes. $d_{\max}/d_{\min} > 1.7, m = 0.315$ (discs), 2.3 (cylinders, prisms); $d_{\max}/d_{\min} < 1.7, m = 0$
Corey shape factor	Co	Ratio of the length of the shortest particle axis to the square root of the product of those of the other two axes
Drag shape factor	ε	Ratio between the drag coefficient of a non-spherical particle and that of a sphere, both being evaluated at the condition of $Re = 1000$
Volumetric shape factor	Ω	Ratio of the volume of the particle to the diameter of a sphere with the same projected area as the particle cubed
Roundness	σ	Ratio of the average radius of curvature of the corners to the radius of the largest inscribed circle
Aspect ratio	E_l	Ratio of the particle length along the symmetrical axis over the largest cross-sectional diameter
Particle shape factor	ψ	$\Psi = \phi/\chi$, Ratio between sphericity and a newly defined circularity X
Stokes' factors	K_1	Modeled as function of the geometric shape descriptors' sphericity and the projected area in the direction motion
Newton's factor	K_2	Modeled as function of the geometric shape descriptors' sphericity and the projected area in the direction motion

$$\mathbf{T}_i = \mathbf{T}_{i,contact} + \mathbf{T}_{i,fluid} + \mathbf{T}_{i,external} \quad (8)$$

However, the motion Eqs. (3) and (5) are strictly correct only for a particle which is symmetric around its center of mass. For a generic non-spherical particle, the moment of inertia always changes with the new spatial orientation of a particle at each time step. To address the

change of the inertia moment for a particle with large aspect ratios and determine the orientation of this particle, the space-fixed and body-fixed coordinate systems are usually introduced to conveniently describe the rotation of non-spherical particles [8,38,39,44,81,85,88, 91,183]. The space-fixed (or laboratory) coordinate system is fixed in a laboratory space, while the body-fixed (or local) coordinate system is a moving Cartesian coordinate system fixed to the particle. The axes of the latter coordinate system are chosen as the principle axes of inertia [184]. In the body-fixed frame, the rotational motion of non-spherical particles can be described as:

$$I_i \frac{d\mathbf{W}_i}{dt} + \mathbf{W}_i \times (I_i \mathbf{W}_i) = \Lambda_i^{-1} \mathbf{T}_i \quad (9)$$

where \mathbf{W}_i is the angular velocity in the body fixed frame, and \mathbf{T}_i is external moment in the inertial frame. I_i is the inertia tensor along the principle axis and Λ_i^{-1} is the transformation matrix converting a vector from the inertia frame into the body fixed frame.

As described in Section 2, basically two kinds of approaches, the single-particle and composite-particle approaches, are used to represent non-spherical particles, and correspondingly, here two different algorithms are used to deal with the problems introduced by particle orientation:

(1) Single-particle approach

In the single-particle approach, the orientation of the particle's principal axes can be described by three Euler angles, (ϕ, θ, ψ) [8,38,39,44,85,88,91,183]. Briefly, at each time step, for convenience the inertia tensor I_i in Eq. (5) in the space-fixed coordinate system (x, y, z) is converted to I_i in the body-fixed coordinate system (x', y', z') by the transformation matrix Λ^{-1} determined by the three Euler angles. The angular velocity \mathbf{W}_i of particles in body-fixed frame can be calculated by Eq. (9). Because angular velocity is closely related to the changes of Euler angles, three new Euler angles can be calculated and then the spatial orientation of particles can be determined on the basis of the so-called quaternion method [185–188], as well as by other methods [184,185,189, 190]. More details about this approach can be found in references [39,88,187].

(2) Multi-sphere particles

In the composite-particle approach, smaller elements such as spheres are connected together to form a given complex shape of a particle. Commonly for a particle i with overlapping spheres

Table 6

Expressions of drag force for multi-particle systems

Authors	Equations
Ergun, (1952) [257] and Wen and Yu(1966) [258]	$F_D = \beta_{pf}(\mathbf{u}_f - \mathbf{u}_p)/\rho_f$ $\beta_{pf} \begin{cases} 150 \frac{(1-\varepsilon_f)^2}{\varepsilon_f} \frac{\mu_f}{(\varphi_p d_p)^2} + 1.75(1-\varepsilon_f) \frac{\rho_f}{\varphi_p d_p} \mathbf{u}_f - \mathbf{u}_p & \varepsilon_f \leq 0.8 \\ \frac{3}{4} C_D \frac{ \mathbf{u}_f - \mathbf{u}_p \rho_f (1-\varepsilon_f)}{d_p} \varepsilon_f^{-2.7} & \varepsilon_f > 0.8 \end{cases}$ $\mathbf{F}_D = f(\varepsilon_f) F_{D0}$ $f(\varepsilon_f) = \varepsilon_f^{-(\alpha+1)}, \alpha = 3.7 - 0.65 \cdot \exp[-(1.5 - \log Re_p)^2/2]$ $F_{D0} = \frac{1}{2} \rho_f C_D A_{\perp} (\mathbf{u}_f - \mathbf{u}_p) \mathbf{u}_f - \mathbf{u}_p $ $F_D = A \frac{(1-\varepsilon_f)^2}{\varepsilon_f} + B(1-\varepsilon_f) Re_p \quad \varepsilon_f < 0.6$
Di Felice (1994) [265]	$A = \begin{cases} \frac{180}{18\varepsilon_f^3 1 + 3(1-\varepsilon_f)^{1/2} / \sqrt{2} + 135(1-\varepsilon_f) / 64 + 16.14(1-\varepsilon_f)} & \varepsilon_f > 0.6 \\ 1 - 0.681(1-\varepsilon_f) - 8.48(1-\varepsilon_f)^2 & \end{cases}$ $B = 0.6057\varepsilon_f^2 + 1.908\varepsilon_f^2(1-\varepsilon_f) + 0.209\varepsilon_f^{-3}$ $Re_p = \frac{\varepsilon_f \rho_f \mathbf{u}_f - \mathbf{u}_p d_p}{\mu_f}$
Koach and Hill (2001) [266]	$F_D = A \frac{(1-\varepsilon_f)^2}{\varepsilon_f} + B(1-\varepsilon_f) Re_p$ $A = 180 + 18 \frac{18\varepsilon_f^4 (1+1.5\sqrt{1-\varepsilon_f})}{1-\varepsilon_f}$ $B = \frac{0.31(\varepsilon_f^{-1} + 3\varepsilon_f(1-\varepsilon_f) + 8.4Re_p^{-0.343})}{1 + 10^{4(1-\varepsilon_f)} Re_p^{-2.5}}$ $Re_p = \frac{\varepsilon_f \rho_f \mathbf{u}_f - \mathbf{u}_p d_p}{\mu_f}$
Beetstra et al.(2007) [267]	$F_D(\varepsilon_s, Re) = \frac{10\varepsilon_s}{(1-\varepsilon_s)^2} + \frac{10\varepsilon_s}{1-1.14\varepsilon_s^{0.3}} + \frac{0.413 Re}{24(1-\varepsilon_s)^2} \left[\frac{-0.058(1-\varepsilon_s)^{-4} + 2.16(1-\varepsilon_s) + 23\varepsilon_s(1-\varepsilon_s) + 8.4Re^{-0.343}}{1+10^{3\varepsilon_s} Re^{-0.5-2\varepsilon_s}} \right]$ for cubic particles
Chen et al. (2015) [228]	

Table 7

Relative merits of the two models [37].

Model type	Computational effort	Numerical accuracy	Suitability for engineering application	Suitability for fundamental research
AVM	Low	Low	Easy	No
IFM	High	High	Difficult	Yes

of the same density, the overall mass m_i , the coordinates of the center of gravity \mathbf{G}_i , and the inertia tensor I_i are given by [106, 164]

$$m_i = \sum_{k=1}^N m_{ik} \quad (10)$$

$$\mathbf{G}_i = \sum_{k=1}^N (\mathbf{G}_{ik} m_{ik}) / m_i \quad (11)$$

$$I_i = \begin{bmatrix} \sum I_{ik} + \sum m_{ik} (G_{Yik}^2 + G_{Zik}^2) & -\sum m_{ik} G_{Xik} G_{Yik} & -\sum m_{ik} G_{Xik} G_{Zik} \\ -\sum m_{ik} G_{Xik} G_{Yik} & \sum I_{ik} + \sum m_{ik} (G_{Xik}^2 + G_{Zik}^2) & -\sum m_{ik} G_{Yik} G_{Zik} \\ -\sum m_{ik} G_{Xik} G_{Zik} & -\sum m_{ik} G_{Yik} G_{Zik} & \sum I_{ik} + \sum m_{ik} (G_{Xik}^2 + G_{Yik}^2) \end{bmatrix} \quad (12)$$

where N is the number of spheres in the composite particle i ; m_{ik} and I_{ik} are the mass and moment of inertia of the single spherical body k , respectively; and G_{Xik} , G_{Yik} , and G_{Zik} are the distances from the principal

axes of the particle to the center of sphere k . By performing a principle axis transformation, the principal moments of inertia can be calculated from Eq. (12) leading to a new inertia tensor:

$$I_i = \begin{bmatrix} I_{X_i} & 0 & 0 \\ 0 & I_{Y_i} & 0 \\ 0 & 0 & I_{Z_i} \end{bmatrix} \quad (13)$$

The normalized eigenvectors obtained from this transformation result in the transformation matrix Λ . The matrix Λ is orthogonal and therefore $\Lambda^T = \Lambda^{-1}$ which allows converting a vector from the space-fixed coordinate system into the body fixed frame as shown in Eq. (9). Several algorithms have been proposed to integrate Eq. (9), and examples can be found in references [191–193].

3.2. Force calculation schemes

3.2.1. Contact forces between particles

After the contacts between particles are detected using the methods introduced in Section 2, another important mission of DEM is to

Table 8

Typical examples of parallel computation of DEM.

Author	Techniques and equipment	Objects	Improvements	Numerical capacity and speed
Radeke et al. (2010) [356]	DEM	▪ sphere ▪ blade mixer	• Graz-Rutgers Particle Dynamic (GRPD)	▪ More than 7×10^6 particles ▪ 8 million particles-one month to finish
Shigeto and Sakai (2011) [359]	Multi-thread parallel computation of DEM	▪ sphere ▪ screw conveyor (4 m × 0.5m)	• linked-list structure algorithm (reduce the memory usage) • Reaction calculation method (double the efficiency of evaluation of contact force)	▪ Up to 1.28×10^6 particles
Kafui et al. (2011) [360]	CFD-DEM	▪ sphere ▪ fluidized bed		▪ 10^6 particles
Xu et al. (2012) [361]	CFD-DEM	▪ sphere ▪ circulating fluidized bed	• Multi-scale CPU-GPU hybrid computation • EMMS model to describe sub-grid structure	▪ Up to 1×10^7 particles ▪ 4.63×10^7 particle updates per second
Jajcevic et al. (2013) [355]	CFD-DEM	▪ sphere ▪ spout-fluid systems	• An efficient coupling method	▪ Up to 2.5×10^7 particles ▪ 25 million particles-1s real time-7200 min
Longmore et al. (2013) [362]	DEM	▪ a tetrahedral lattice	• Multi-sphere method	▪ 256,000 tetrahedral granules at 120 FPS
Govender et al. (2015) [366]	DEM	▪ convex polyhedra ▪ drum	• BLAZE-DEM framework for the GPU architecture • A GPU optimized collision detection algorithm (SP method)	▪ 3.4×10^7 polyhedra (13 s per step)
Gan et al. (2015) [365]	DEM	▪ ellipsoid ▪ rotating drum		▪ 5×10^4 ellipsoids

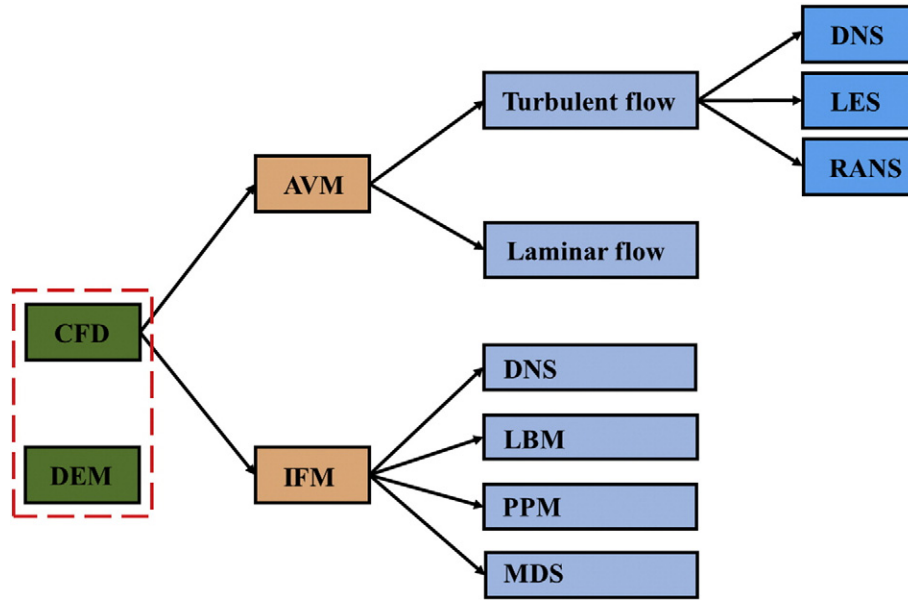


Fig. 14. Available CFD solvers for fluid-particle system.

evaluate the contact forces. In general, the contact between particles is not at a single point but rather on a finite area due to the deformation of the particle surface. This deformation is numerically described by the overlap between rigid bodies in DEM. The contact force consists of two components: the one normal and the other tangential to the contact plane. It is very difficult to accurately evaluate a generalized contact traction distribution over the contact area between non-spherical particles. This is because such an evaluation is closely related to many geometrical and physical factors such as the shape, material properties and movement state of particles. Alternatively, to be computationally

efficient, simplified models or equations are generally adopted to determine the forces and torques resulting from contacts between particles.

(1) Contact forces between spherical particles

In the simplest case, which is the case of spherical particles, the calculation of the contact forces has been comprehensively established and well-reviewed by Zhu et al. [36,39,194] and Zheng et al. [195]. The elastic repulsion and energy loss through internal friction are the two characteristics that are usually quantified to express the normal collision force between particles. In

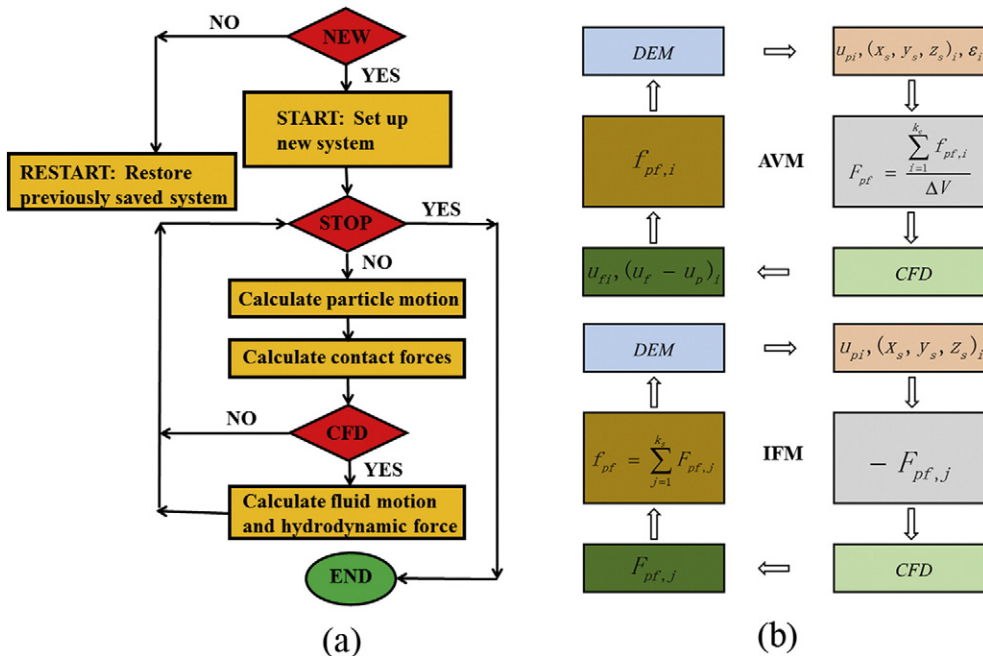


Fig. 15. (a) Flow chart for the computational sequence in AVM- and IFM-DEM; (b) Data exchange between the two phases [300,301].

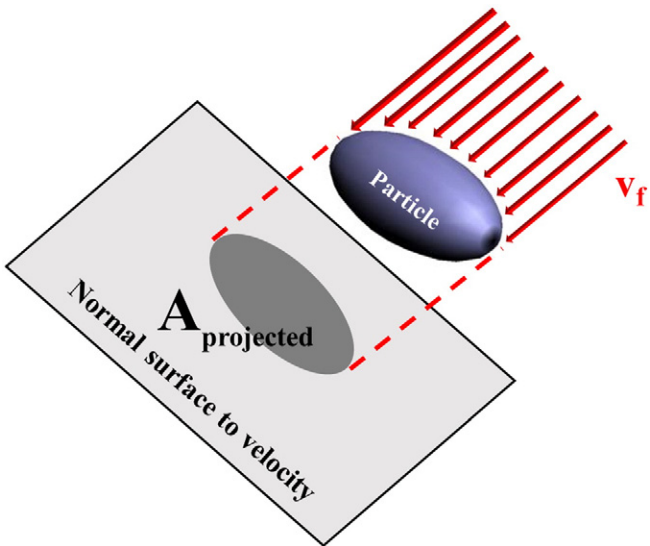


Fig. 16. Projected area of shaped particle in the direction of the flow [95].

DEM, the existing models to describe the elastic repulsion can be roughly divided into four main groups according to the dependency of the repulsion force on the overlap distance: namely, linear models, non-linear models, models with hysteresis and continuous interaction (or short-range force) models. These equations are listed in detail in Table 1. The energy loss during real collisions between particles generally depends on the impact history, and the dissipative energy can be modeled by the non-conservative viscous force during collision. The related approximations are also listed in Table 1 [196–199].

The tangential force depends on the normal force $F_{n,ij}$ and normal displacement δ_{ij} , as well as on the history of the tangential contact and energy dissipation. In previous publications, generally two major types of approaches have been used to model the tangential contact forces, namely the global and complex models.

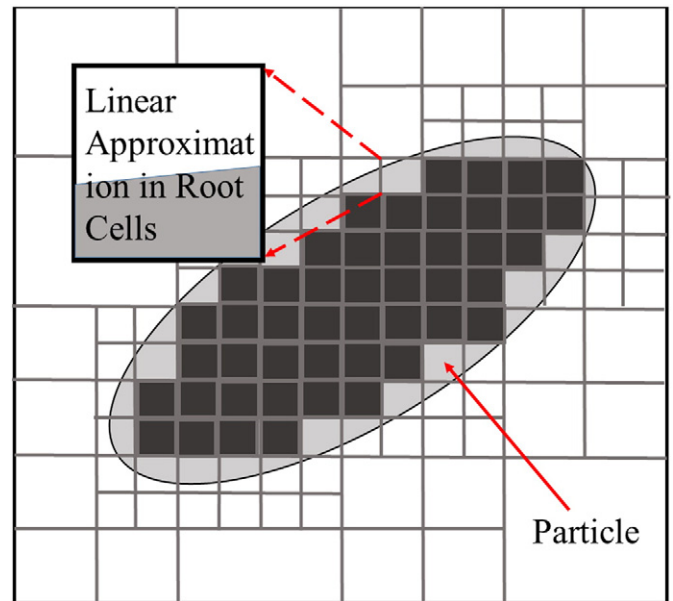


Fig. 18. Computational determination of the bed porosity is carried out using a recursive octree method. In the terminating cells, inset, a linear approximation of the volume fraction is used [95].

The relevant equations of these models are listed in Table 2 and more detailed information about these two approaches can be found in the literature [39,200].

(2) Contact forces between non-spherical particles

Compared to the treatment of the contact forces between spherical particles, the formulation of the contact forces for non-spherical particles is far more complicated. Several situations and corresponding treatments are listed as below.

• Particles represented by the multi-sphere model

In this category, the appropriate contact force model is the one for spherical particles: the force in each component sphere contact can be calculated using the "standard" model for spherical particle contacts. However, it should be noted that Kruggel-

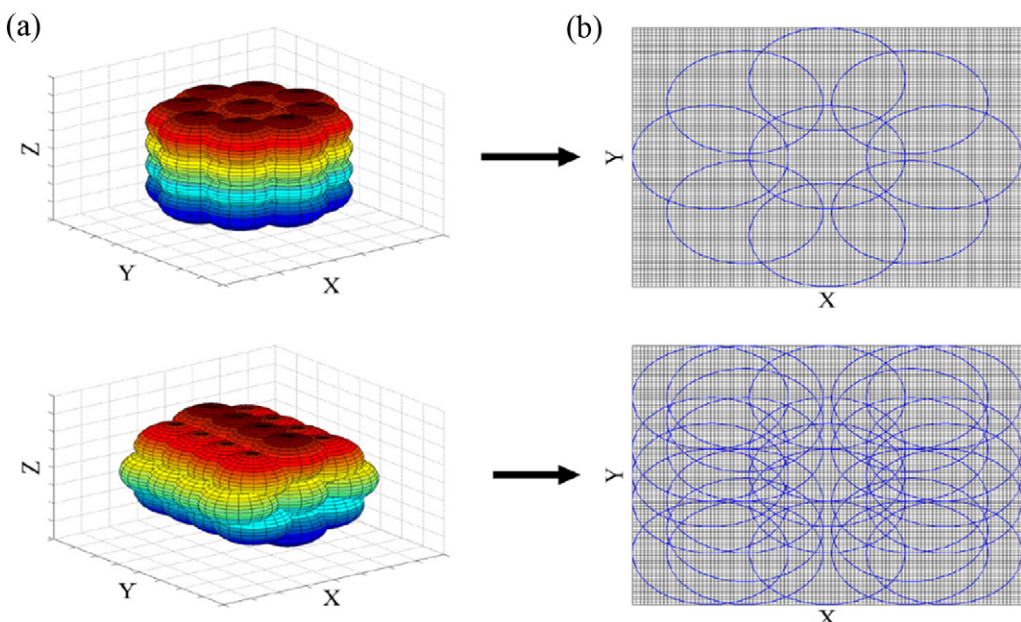


Fig. 17. Two examples for the calculation of the projection area, (a) clustered sphere particles with specific orientation, (b) the resulting projection areas for the x, y-plane calculated for a grid resolution of 100×100 [214].

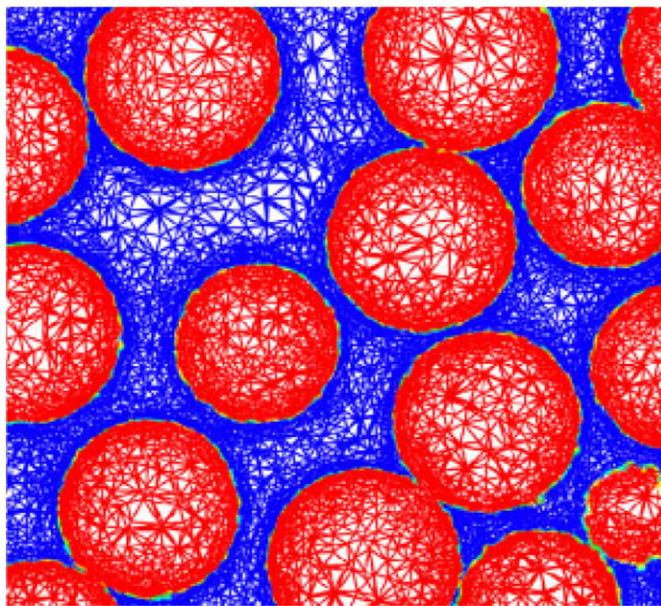


Fig. 19. An example of the finite element mesh [315].

Emden et al. [164] and Kodam et al. [201] have demonstrated that the overall contact may become over-stiff and over-damped, if contacts occur simultaneously on multiple spheres of a composite particle.

- Particles represented by other methods

In this category, the computation of contact force is usually carried out by the direct use of the models for spherical particles or their modifications. The difficulties are encountered in the

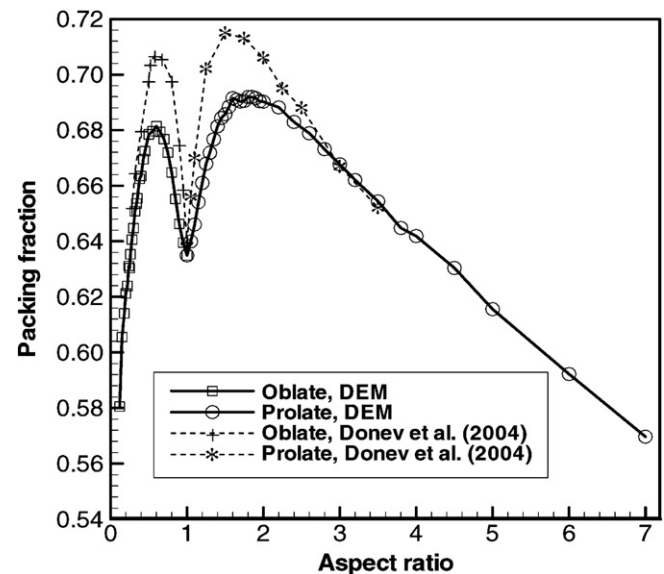


Fig. 21. Variation of packing fraction with aspect ratio under poured conditions (adapted from [88], Copyright 2010, with kind permission from ACS Publications).

determination of the contact parameters such as the amount of overlap, contact point and the normal vector.

Non-Hertzian contact geometries

For contact geometries such as those involving sharp corners, it is usually assumed that the contact force in the normal direction has the following form [48,50,53,56–59,61]:

$$F_n = k\delta_{\text{contact}} + v\dot{\delta}_{\text{contact}} \quad (14)$$

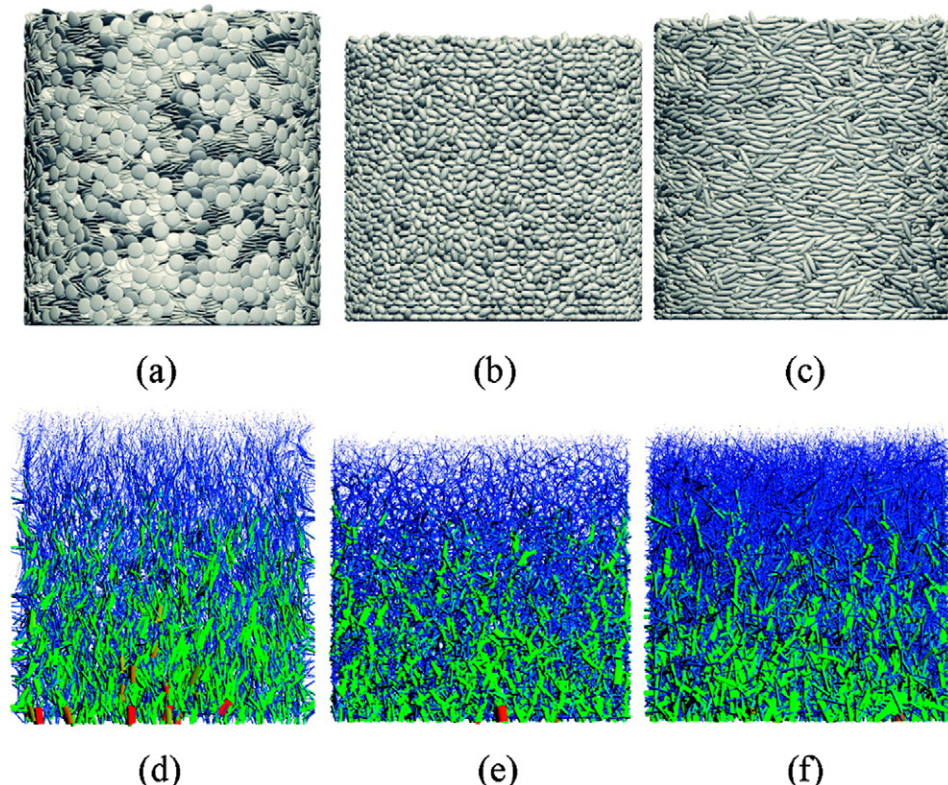


Fig. 20. Final packing of ellipsoids with aspect ratios of (a) 0.2; (b) 2.0; and (c) 4.0; and their corresponding force structures (adapted from [88], Copyright 2010, with kind permission from ACS Publications).



Fig. 22. Left particle system (prolate ellipsoids, cut-out); center corresponding pore-phase graph; right particle system with pore-phase graph [103].

where k and v are the linear spring constant and dashpot coefficient, respectively, and δ_{contact} and $\dot{\delta}_{\text{contact}}$ are the normal overlap distance at the contact and the normal relative velocity between two objects, respectively. Eq. (14) is clearly not the correct form for a real contact. For example, a cylinder-end-face to a plane-wall contact and cylinder-band to plane-wall

contact will generally have different contact forces because of their different overlap volumes at the same overlap. Despite this deficiency, a few researchers still prefer to use the approach described by Eq. (14) due to its simplicity [38,53,74]. An attempt to include the influence of the contact geometry into the force model was proposed by Feng and Owen [202].

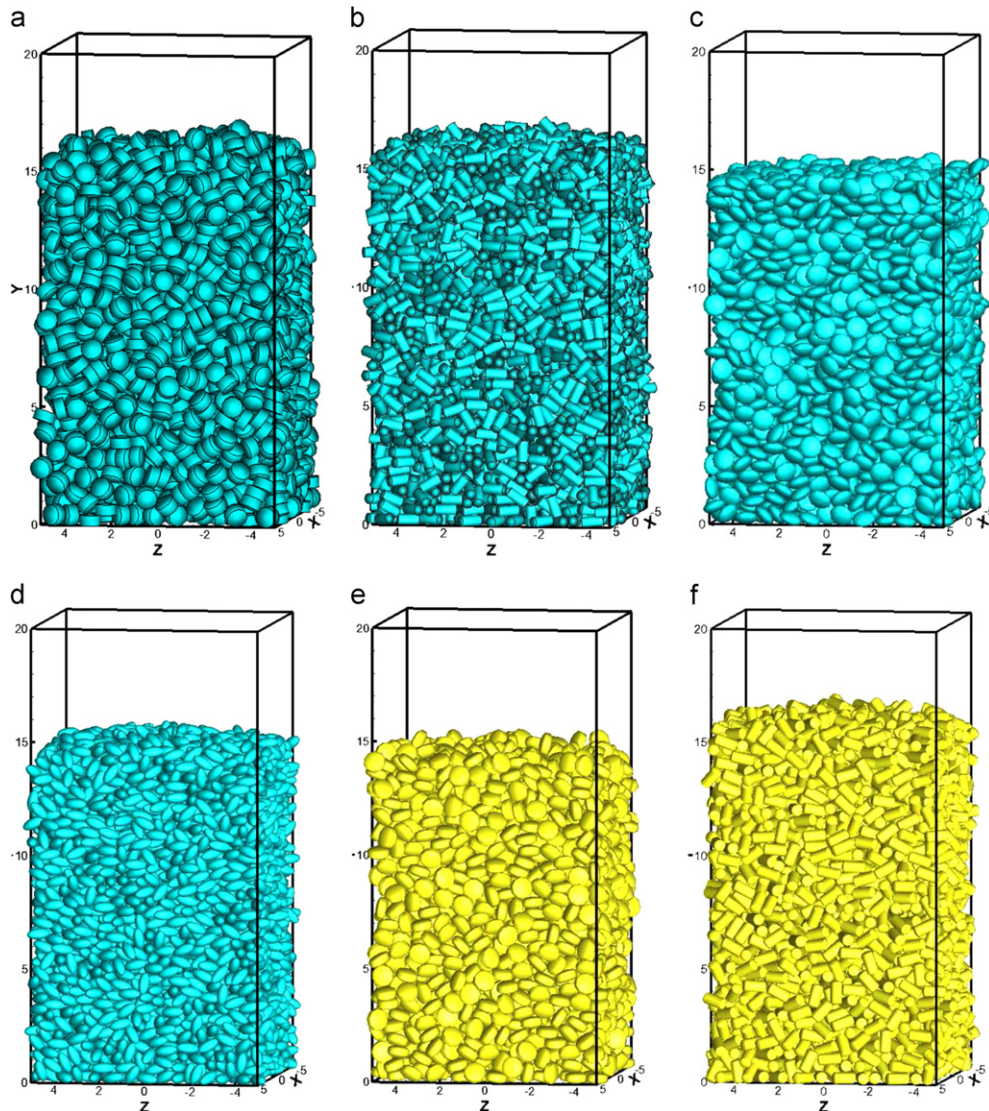


Fig. 23. Simulated 3D packing of particles of different shapes: (a) disks; (b) cylinders; (c) oblates; (d) prolates; (e) tablets; and (f) capsules (adapted from [44], Copyright 2014, with kind permission from Elsevier).

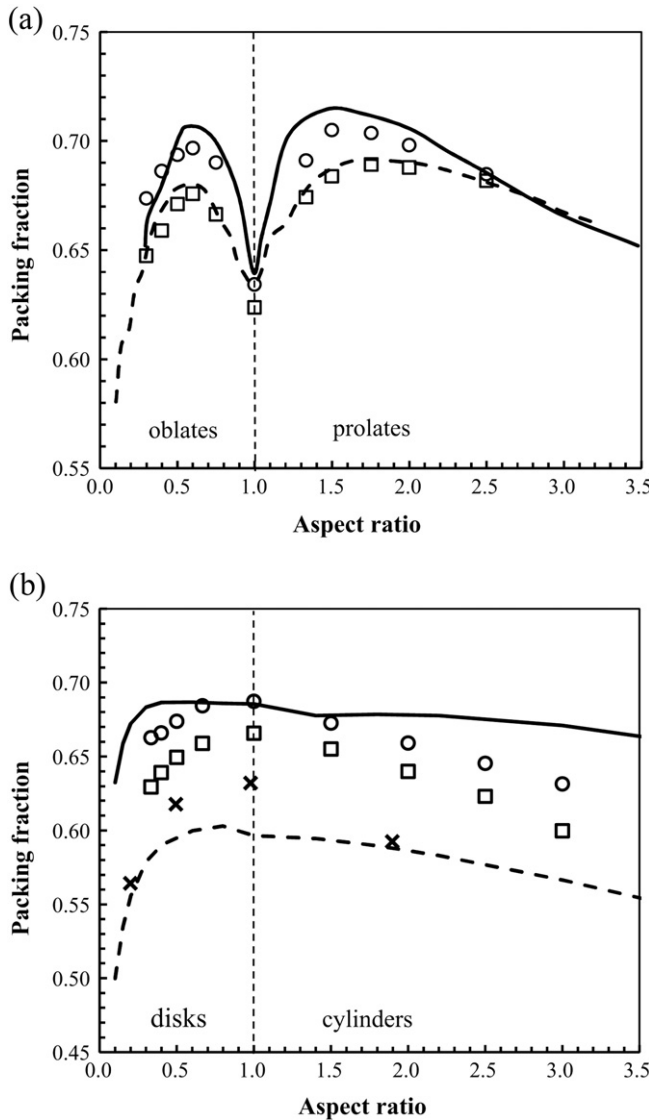


Fig. 24. Packing fraction as a function of aspect ratio for different aspect ratios (a) sliding friction 0.3 and 0.1; and (b) cylinders and disks (dash and solid line represent the experimental results.) (adapted from [44], Copyright 2014, with kind permission from Elsevier).

In their model as shown in Fig. 13, the magnitude of normal contact force was given by:

$$\|\mathbf{F}_n\| = E'(A)b_w \quad (15)$$

where A and b_w are the overlap area and contact width, respectively; and $E'(A)$ is the derivative of energy function $E(A)$. The normal force given in Eq. (15) is the result of the assumptions that (a) elastic strain energy stored in the contact increases monotonically with the overlap area, and (b) the normal force should be applied in a direction that reduces the contact energy at a maximum rate. However, it is very difficult to decide on a specific relationship between contact energy and overlap, because the contact geometry always varies depending on the particle orientation, contact location, magnitude of the overlap, as well as the material physical parameters. Furthermore, issues may arise if this concept is extended to 3D particle shapes, because of significant

difficulties in analytically determining the overlap volumes for complex particle shapes. Hertzian contact geometries When the surfaces of non-spherical particles are continuous and the particle deformation induced by the contact is far smaller than the dimensions of each particle as in the case of an ellipsoid contact, the Hertz theory can generally be applied to calculate the contact force, and the detailed assumptions and theories can be found in references [195,203].

3.2.2. Particle-fluid interaction forces

Since the pioneering work of Tsuji et al. [204], DEM approach has been increasingly extended to describe the behavior of particles immersed in flowing fluids in various processes such as fluidization and pneumatic conveying. The fluid flow can be successfully modeled at different length scales from discrete to continuum [37], and in principle all these methods can be combined with DEM to describe the coupled particle-fluid flows [205–213]. Among them the combined CFD and

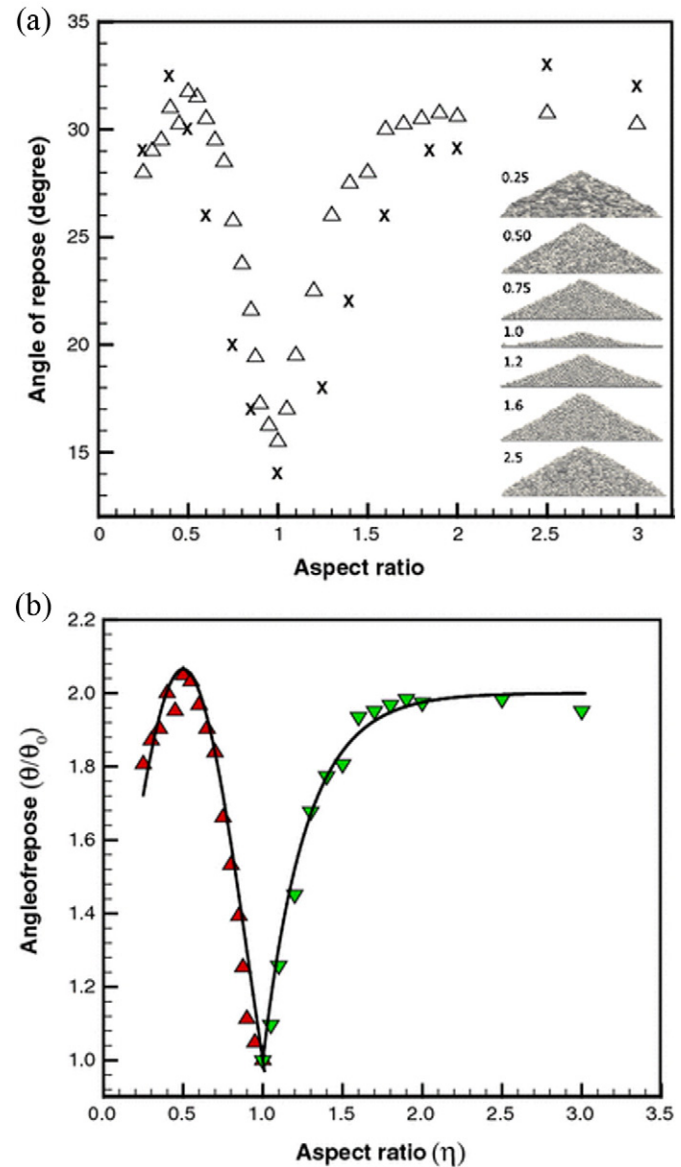


Fig. 25. (a) Angle of repose for different aspect ratios (the insets are sandpiles formed by the discharging method; (b) Angle of repose for different aspect ratios (adapted from [183], Copyright 2014, with kind permission from Springer Science and Business).

DEM approach has received the most attentions [36,37]. However, the current CFD-DEM technique is still largely limited to spherical particles because of enormous difficulties in simulating non-spherical particles: namely, apart from the great challenges in representing non-spherical particles and detecting their contacts in the DEM system, simulating the coupled behaviors of non-spherical particles and flow additionally suffers from the dramatic increase in the complexity of data transfer between the CFD and DEM systems as well as determining the particle-fluid interaction forces.

First breakthroughs have been gained in the CFD-DEM simulation of gas-solid two-phase flows that involve regular shape particles (e.g., ellipsoidal, cylindrical, and cubic particles) [34,59,85,89,95,96,135,214] and individual irregular (e.g., corn-shaped) particles [6,11], which can be described in DEM with direct analytical functions [34,85,89,95,96] or by simply gluing several spheres together [6,11,15,20,59,135,214,215]. In the above publications, some important aspects of certain gas/non-spherical particle systems have been discussed, which include local particle velocity, local and overall porosity, pressure drop, and so on. However, detailed microscopic information is scarcely reported, which is partly due to the approximate and tentative consideration of the forces and motion of non-spherical particles. Non-spherical particles have many additional intricate features, including more complicated fluid forces (for example, the shape induced lift force, the orientation dependent lift force and drag force, etc.), the significant secondary motion and a changing preferred orientation depending on the regime of motion [46]. It is essentially necessary to

properly capture these phenomena by constantly improving unusual strategies. This involves keeping the track of the orientation and rotation of the particle as well as formulating appropriate fluid forces that depend on the particle shape and orientation.

3.2.2.1. Drag force. A bulk of early investigations focused on the drag force experienced by spheres moving through a fluid, and the resulting empirical correlations for the drag coefficient, C_D , provides sufficient information to estimate the drag force of spheres. These correlations for spherical particles have been reviewed subsequently by many authors in treatises and review articles [216,217], and comparisons between most of these correlations for spheres showed relatively small deviations [218]. However, for non-spherical particles, the problem of the drag force becomes much more complicated [46]. The terminal falling velocity (and hence the drag coefficient) for a typical non-spherical particle is strongly influenced by its size, shape, and orientation in addition to the physical and rheological properties of the fluid medium, wall effects, and so on.

Currently available methodologies to deal with the drag force on a non-spherical particle fall into two distinct categories: the first approach is to develop the exclusive drag expressions for particles with fixed shape and orientation, such as spheroidal particles [219–221], polyhedrons [222,223], cubes [224–228], cylinders [229–239], disks [240–243], hemispheroidal particles [244], parallelepipeds [245], cones [246], and flat annular rings [247], to name a few. Some typical expressions derived by this approach are listed in Table 3. In the second

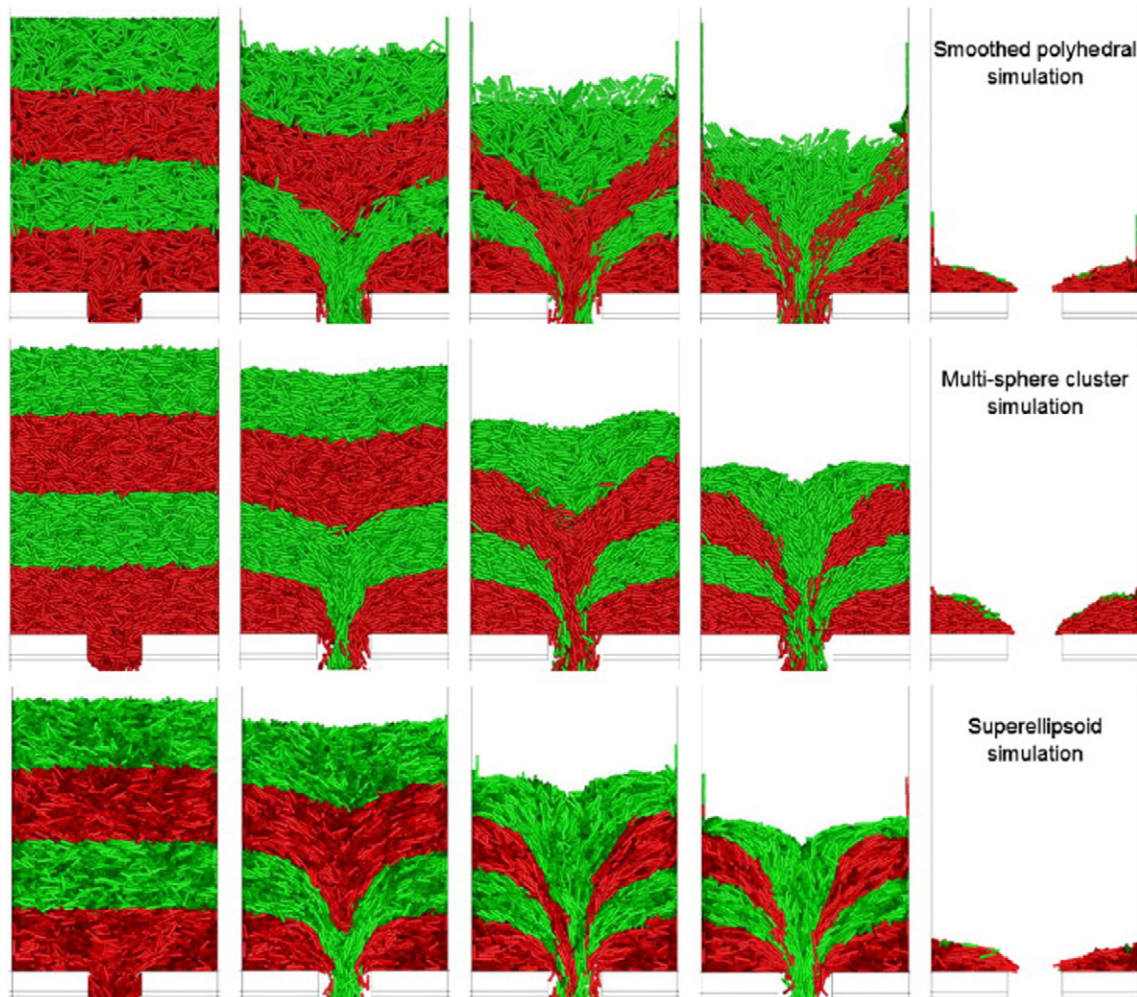


Fig. 26. Hopper discharge of smoothed polyhedron, multi-sphere cluster and super-ellipsoid [58].

approach, efforts are made to provide a single general correlation on the drag coefficient for non-spherical particles covering as many shapes and orientations as possible. The attempts by Haider and Levenspiel [223], Thompson and Clark [248], Ganser [249], Chien [250], Hartman et al. [251,252] and others as listed in Table 4 illustrate the applicability of this approach. Obviously, for a particle with a certain specific shape, the general expressions derived from the second approach tends to be less accurate than the specialized one for that shape, but the feasible interpolations/extrapolations to the various shapes provide the general expressions an attractive perspective on engineering applications.

In both approaches, one of the most important challenges is to find appropriate shape factors that comprehensively describe the shapes of non-spherical particles and their orientations in fluid. The sphericity, ϕ , is the most commonly used shape factor to account for the particle shape [253], and this concept can produce promising results for non-spherical particles with aspect ratios less than 1.7 [216,254]. However, for particles having extreme shapes and those having little resemblance to a sphere, the sphericity concept will fail to produce satisfying quantitative results [223,255]. Additionally, from a practical standpoint, the sphericity is difficult to be determined for highly

irregular particles because it requires a measure of the surface area, which is not easy to be obtained for extremely irregular particles or rough particles. Due to the limitations of the sphericity concept, many other shape factors have also been attempted for characterizing the shape of a particle and its orientation in fluid, and some of them are listed in Table 5.

Apart from the shape factor, characteristic lengths or sizes of non-spherical particles may also bring some confusion. The choice of reference area (derived from the characteristic length or size) is arbitrary, as long as it is used consistently. Many authors defined the reference area as the cross-section area of the volume equivalent sphere guaranteeing that it stays constant regardless of the angle of incidence, while the projected area [216], the total surface area of the particle [256] and other characteristic areas have also been reported as the reference area. However, all these drag coefficients calculated with different reference areas are interchangeable because the product of the drag coefficient times the area used in the calculations ($C_D \cdot A$) is a constant.

Aforementioned expressions of the drag force are generally obtained theoretically or semi-empirically for an isolated particle or for particles in dilute systems. When considering practical concentrated particulate

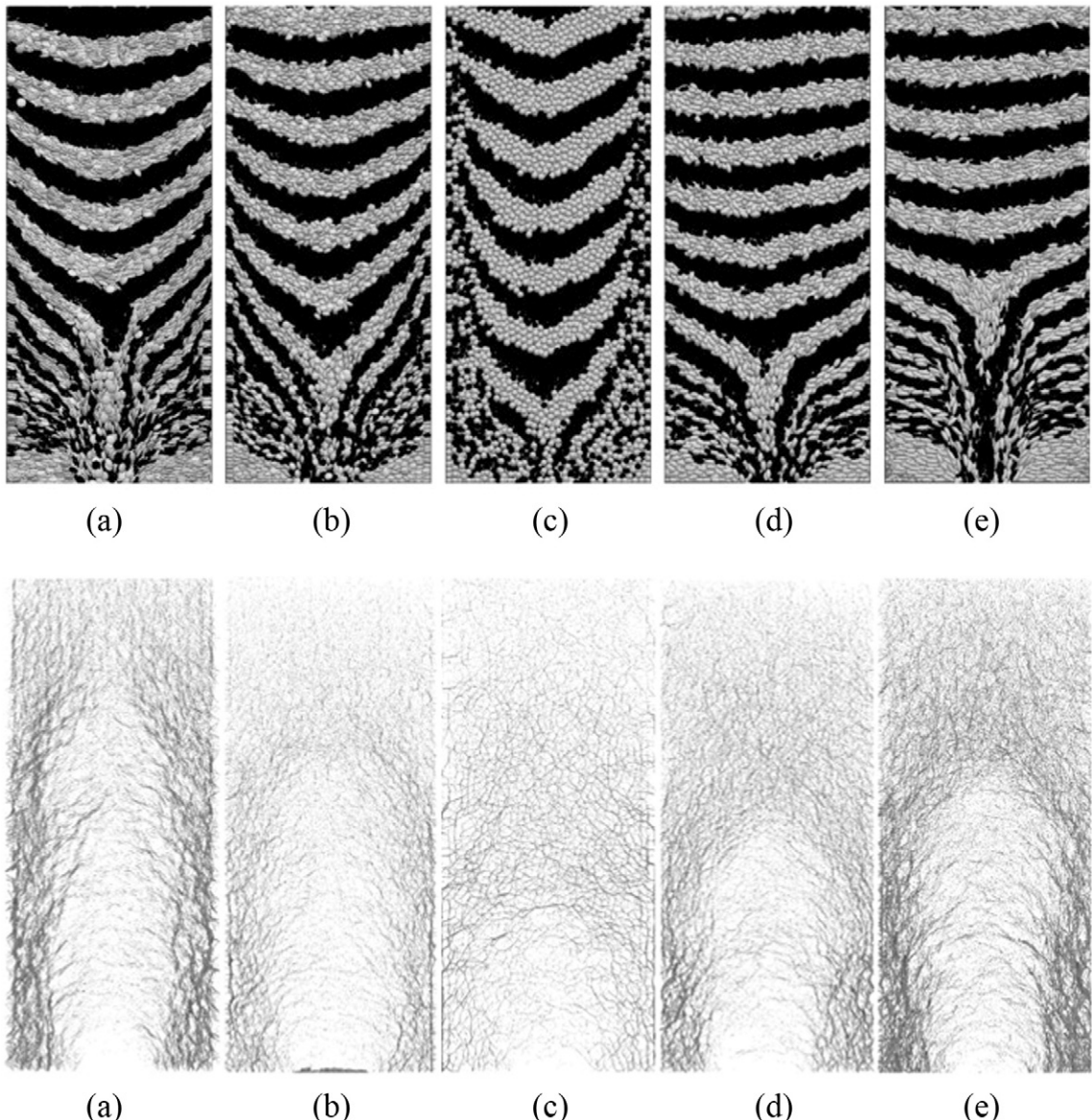


Fig. 27. Snapshots and force network from the DEM simulations for different aspect ratios at the steady state: (a) 0.3, (b) 0.5, (c) 1.0, (d) 2.0, and (e) 3.0 (adapted from [91], Copyright 2014, with kind permission from Elsevier).

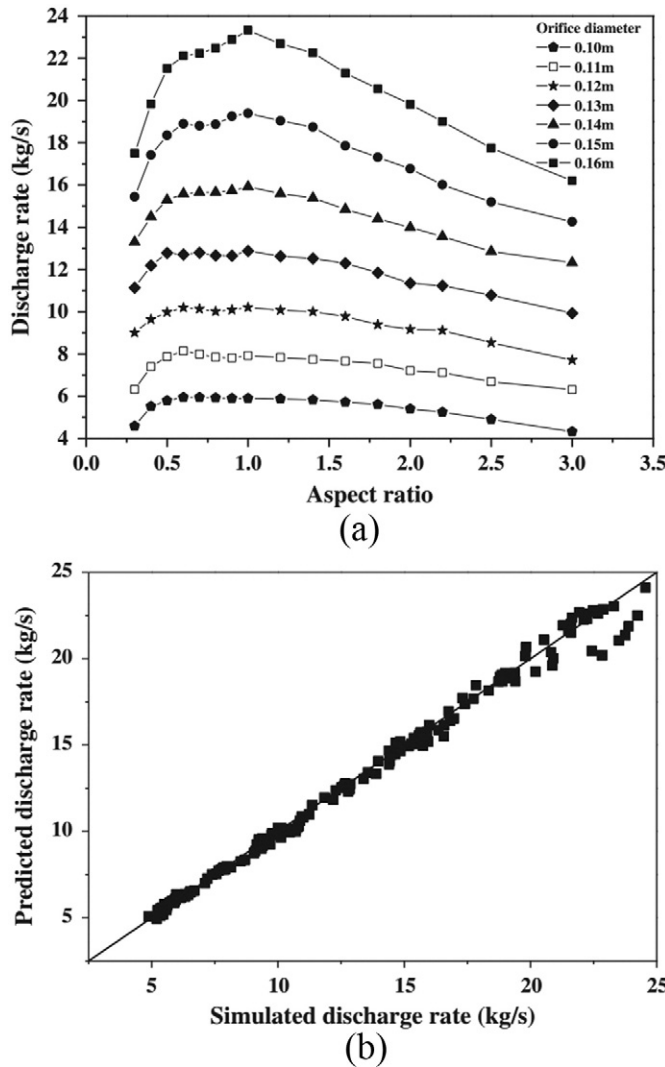


Fig. 28. (a) Hopper discharge rate obtained from the DEM simulations for different aspect ratios and orifice diameters; (b) Comparison of the predicted results using the modified Beverloo equation with the simulated results under different conditions (adapted from [91], Copyright 2014, with kind permission from Elsevier).

flows, especially the dense gas-solid or liquid-solid multiphase systems in industrial processes, the particle drag force may deviate significantly from that of an isolated particle. For flows through a packed bed of particles, the most commonly used approach to determine the particle drag force is to measure the bed pressure drop [257–261] or bed expansion [262–264], which can then be used to find an average drag force for a single particle. The resulting correlations developed for the drag force F_D can be classified into two categories. The first category is usually

formed by F_{D0} , which is the drag force around a single particle, and a correlation function f , which includes the parameters, such as the local voidage and particle Reynolds number in order to take into account the effect and interaction of surrounding particles. The most popular examples for the composed F_D are from Di Felice [265] and Wen and Yu [257,258] (see Table 6). This approach is very promising to develop the drag force relationships for multiphase systems with non-spherical particles, due to the abundance of reports on the drag coefficients of isolated non-spherical particles, as shown in Table 3. In the second form, F_D is expressed in one formula, which includes particle-particle interactions with solid holdup. Typical and well-known examples of this form are expressions developed by Ergun [257], Koch and Hill [266], Beetstra et al. [267], as listed in Table 6.

Given the lack of feasible or reliable drag force expressions for dense NSPS, the popular equations of Ergun, and Wen and Yu [257,258] and Di Felice [265] for spherical particles are usually directly applied to calculate the drag force for non-spherical particles as well [6,11,15,20,34,59, 85,89,95,96,214,215]. The Ergun equation considers the effect of particle shape using the concept of sphericity ϕ , but it may have a large deviation when applied to non-spherical particles [268,269]. It should be pointed out that there is no consensus at present as to the most suitable correlation for accurately predicting the fluid drag force even in a spherical particulate system at a given Reynolds number and packing fraction, let alone in an NSPS. Thus, it is necessary to validate the existing drag force correlations to choose an appropriate one for simulation works.

3.2.2.2. Lift force. Compared to spherical particles, behaviors of non-spherical particles in turbulent flows are observed to be much more complicated, and the lift force acting on them usually can no longer be neglected [46]. For irregular non-spherical particles submerged in a flowing fluid, the pressure differences on the unsymmetrical particle surfaces and the deviation of the center of pressure from geometric center will easily result in the shape induced lift force on the particles, consequently causing their sideways motion. For regular non-spherical particles such as disks and spheroids, the lift force is present when the particle's principle axis is inclined to the main flow direction. In high Reynolds number flows, the secondary motions of non-spherical particles will also cause the particle's principle axis to be oriented in the flow direction [240], and thus an orientation dependent lift force and its torque will consequently act on the non-spherical particle. This is very similar to the concept of 'aerofoil lift' in aerodynamics.

Given that there are relatively abundant predictions for the drag coefficient of non-spherical particles, but significantly scarce information and lesser understanding of the lift force and torques, one common method to deal with the lift force is to assume that it is proportional to the drag force. For example, as in the case of drag force, the lift force can be also characterized by a lift coefficient defined as:

$$C_L = \frac{F_L}{\frac{1}{2} \rho_f u^2 A_p} \quad (16)$$

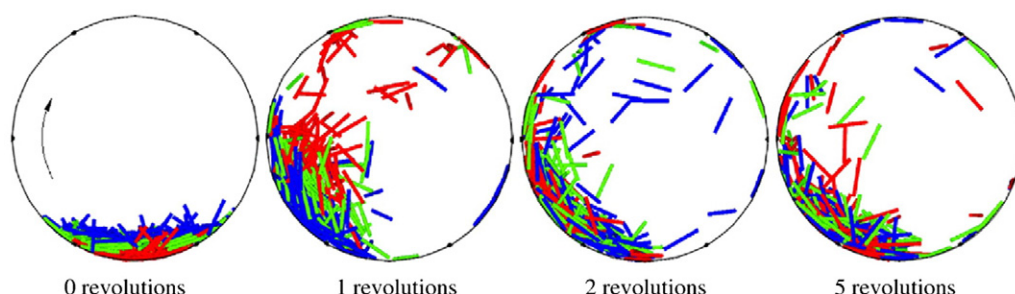


Fig. 29. Dynamic mixing of slender particles in a rotary dryer at different revolution numbers [115].

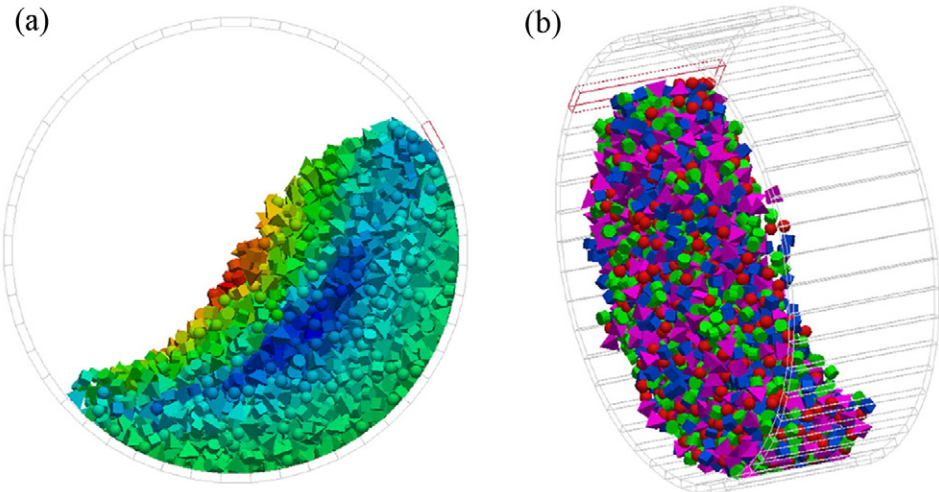


Fig. 30. Rotating drum filled with a blend of spheres, cylinders, cubes and tetrahedra colored by (a) their translational velocity; and (b) their shape [48].

where F_L is the actual lift force, and

$$\frac{C_L}{C_D} = \frac{\sin^2 \alpha \cdot \cos \alpha}{\sin^2 \alpha + 0.65 + 40 \text{Re}^{0.72}} \quad (\text{in Newton law region}) \quad (17)$$

[276]

$$\text{or } \frac{C_L}{C_D} = \frac{\sin^2 \alpha \cdot \cos \alpha}{0.65 + 40 \text{Re}^{0.72}} \quad (30 < \text{Re} < 1500) \quad (18)$$

[46] where α is the angle between the particle's principle axis and flow direction.

Direct prediction of the lift force for non-spherical particles is also proposed, and one of the examples is from Zasrawny et al. [277], which was claimed to give a very good fit for all of the particle shapes, Reynolds numbers and incident angles:

$$C_L = \left(\frac{b_1}{\text{Re}_p^{b_2}} - \frac{b_3}{\text{Re}_p^{b_4}} \right) \sin(\alpha)^{b_5 + b_6 \text{Re}_p^b} \cos(\alpha)^{b_8 + b_9 \text{Re}_p^{b_{10}}} \quad (19)$$

4. Fluid-particle coupling scheme

In this section, numerical issues related to the coupling schemes of non-spherical DEM and fluid are briefly reviewed. Apart from various force calculation techniques, it is obvious that the coupling scheme is also a key factor in achieving good overall computational efficiency. Therefore, it is of paramount importance to pick a suitable numerical

method depending on the problems, which is the main target of the current section. As stated above, in particle-fluid flows the interaction forces between fluid and solid particles play a major role in determining particle motion through the fluid [278,279]. This is particularly true in systems where high particle concentrations are present, some examples being the fluidized bed [280–282], spouted bed [283,284] and blast furnace [19,285].

Zhu et al. [36,37] have critically reviewed theoretical developments and major applications of the coupled CFD-DEM techniques, for spherical particles. Generally speaking, one may choose to work with either of the following two schemes for carrying out coupled CFD-DEM simulations: 1) Averaged Volume Method (AVM), where several solid particles are placed in one CFD cell, and the hydrodynamic force on those particles are evaluated based on empirical formulas; and 2) Immersed Family Methods (IFM), where each particle is placed in the flow field which is normally larger than one single CFD cell. The former scheme has a superior computational convenience for involving more particles in the simulation, but it cannot consider the particle geometry exactly during the coupling as discussed in Section 3.2.2. On the contrary, the latter scheme can produce detailed CFD information around a particle surface, and thus is more accurate. But the consequent drawback is its high computational burden, which makes it difficult to be used in investigations of actual three dimensional engineering problems. Obviously, the force calculation in Section 3.2.2 is developed under the assumption of AVM while the fluid-particle interaction force for the CFD part is obtained by summing up the forces acting on all the particles in a fluid cell. On the contrary, the coupling forces in the IFM scheme can be directly obtained by integrating the local forcing terms along the particle boundary

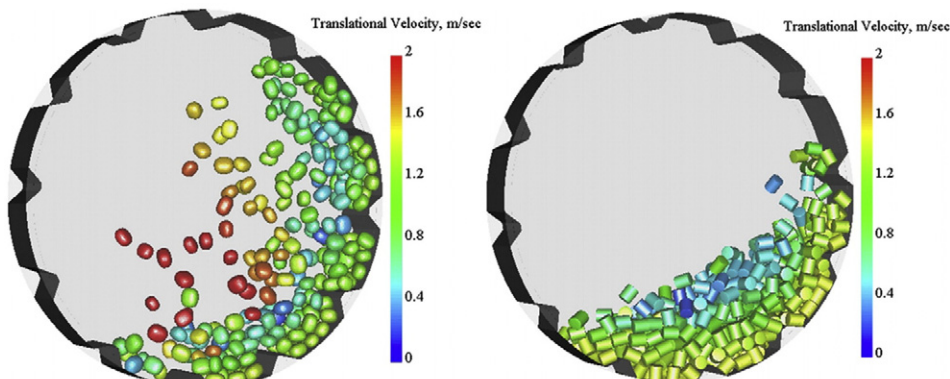


Fig. 31. Snapshots and illustration of worn media shapes and the clypebs [98].

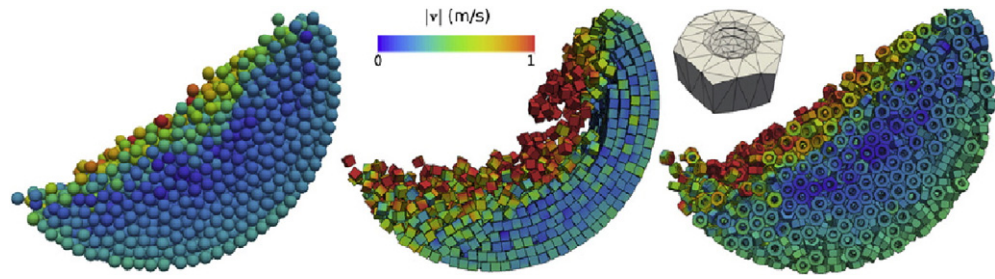


Fig. 32. Comparison of simulations of 3000 particles in a rotating drum for spheres (left), cubes (middle) and a complex “nut” mesh (right) [69].

which are highly dependent on the numerical schemes. So the later part is not summarized together in Section 3.2.2 but introduced below in each section detailing the numerical schemes. Presently available CFD solvers for the fluid-particle interaction system are briefly given in Fig. 14 with a summary of their relative merits listed in Table 7. As

shown in Fig. 14, all the commonly used numerical tools, including the Direct Numerical Simulation (DNS) [286], the Large Eddy Simulation (LES) [287] and the solution of the Reynolds-Averaged Navier-Stokes Equations (RANS) [288], can be adopted for solving turbulent flow fields in coupled AVM-DEM simulations. While in a coupled IFM-DEM

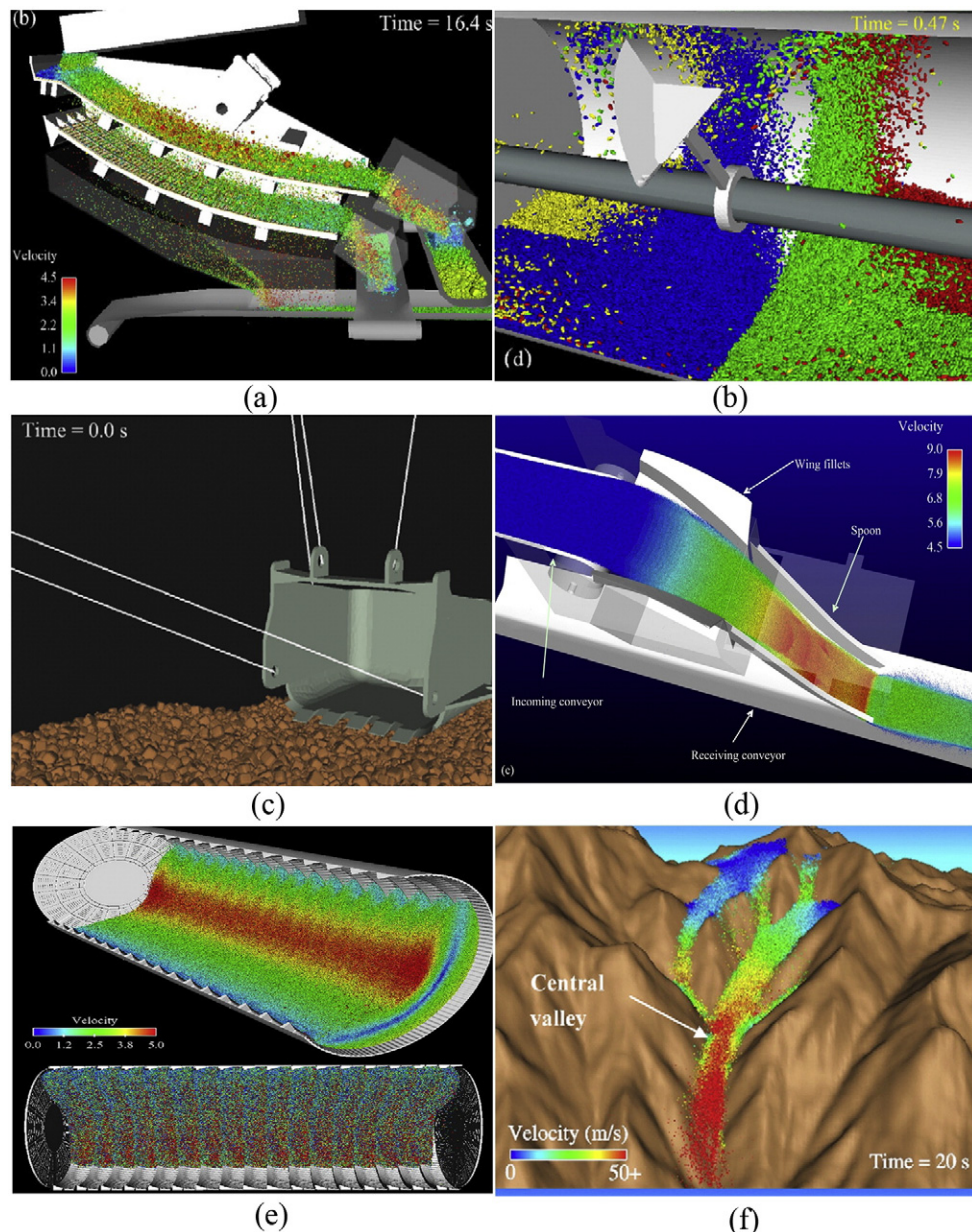


Fig. 33. (a) Vibrating screen; (b) One blade plough share mixer; (c) ESCO dragline bucket; (d) inline conveyor transfer chute; (e) cement ball mill; (f) landslide from collapse of an escarpment (adapted from [86], Copyright 2009, with kind permission from Elsevier).0e.

simulation, CFD solvers may vary among, Finite Element Method (FEM) [289,290], Level Set Method (LSM) [291] and Particle FEM (PFEM) [292] depending on the Navier-Stokes equations used and also among other solvers such as lattice Boltzmann method (LBM) [293,294], Pseudo-Particle Modeling (PPM) [208] and Molecular dynamic simulation (MDS) [295]. However, the distinction between AVM and IFM is mainly based on concepts rather than numerical solvers. For example, Zhang et al. [279] coupled LBM with DEM through a so-called PIBM where the particle size is much smaller than the CFD cell itself, and therefore, the LBM-PIBM-DEM scheme obviously follows the AVM style. It is also worthwhile mentioning that there are two different 'DNS' mentioned in Fig. 14, the one at the top right corner is a common name in the turbulent field which is dedicated to provide a direct numerical solution to

the Navier-Stokes equations without any modelling, while the one at the lower half was defined by Hu et al. [296], and followed by Zhu et al. [37] and in this paper. It is labelled this way to emphasize that no-modelling process is used to calculate the fluid-particle interactions. The readers will find it easy to identify the differences from the context of the content being presented.

4.1. Computational sequence

Fig. 15 displays the flow chart for the computational sequence both in AVM- and IFM-DEM and that for data exchange between the two phases. As shown in Fig. 15(a), the computational sequences of AVM- and IFM-DEM are basically the same, and following the sequence, one

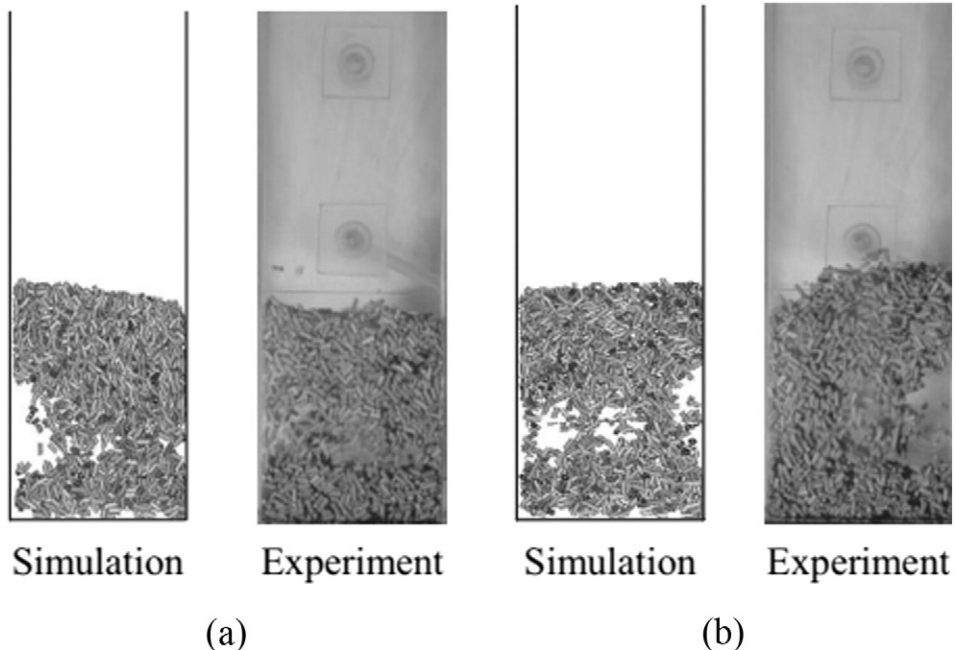


Fig. 34. Comparison of simulated flow patterns with experiments at different superficial gas velocity (adapted from [135], Copyright 2009, with kind permission from WILEY-VCH Verlag GmbH & Co. KGaA).

may start up a completely new case or continue the simulation from a saved interim state. At each time step, the simulation can begin with the DEM part, which first allows all the particles to move considering all the possible forces on particles. The particle positions are updated; newly formed contacts and contact forces will be considered, and the contacts that no longer exist will be removed. Then, solid particles are regarded as (moving) boundaries, which provide the position and velocity for the evaluation of porosity and fluid-solid interaction force. This information together with other macro boundary conditions enables the calculation of the flow field. For example, the CFD solver of the Navier-Stokes equations always contains explicitly calculated fluid velocity components and implicitly determined pressure from Poisson's equation, which is controlled by the mass residual. When new fluid velocities are obtained, the sequence of calculations comes to an end or goes back to the beginning again to make another round of calculations by sending the new fluid-solid interaction forces to DEM.

As shown in Fig. 15(b), the data exchange in AVM-DEM is slightly different from that in IFM-DEM. In an AVM-DEM scheme, the solid particles are mapped into CFD cells which can be structural [297] or non-structural [298]. The information of fluid at the particle positions are obtained using the numerical extrapolation from the circumambient fluid points [299]. Then, using a suitable empirical formula as introduced in Section 3.2.2, the fluid-particle interaction forces can be evaluated mainly based on the following information: the velocity difference between the two phases, the fluid property and local porosity. The feedback force on the fluid is obtained by summing up the forces acting on

$$\sum_{i=1}^{k_p} f_{pf,i}$$

all the particles in each control volume, $F_{pf} = \frac{1}{\Delta V} \sum_{i=1}^{k_p} f_{pf,i}$, as shown in Fig. 15(b) top. However, in an IFM-DEM scheme, since a particle could be much larger than one single CFD cell, it is not acceptable to simply map the particle center in the cell. On the contrary, the interaction between each CFD node and the particle boundary should be considered. The translational and rotational fluid velocities on the particle surface should be first obtained. Then, these fluid velocities will be further modified by the solid velocity, and the fluid-solid interaction force can be evaluated based on the difference of fluid velocities, before and after the modification. Finally, an integral along the particle boundary

needs to be conducted to obtain the total force on the particle, f_{pf}

$= \sum_{j=1}^{N_s} F_{pf,j}$, as shown in the bottom of Fig. 15(b), where N_s is the number of Lagrangian points on the surface of one single particle. Due to the fact that a particle boundary surface intersects many CFD cells, one can use all kinds of available mesh-work to describe the complex interaction processes such as directly employing two sets of meshes to represent the two phases or updating one set of moving CFD meshes to monitor the particle position and shape. These two schemes will be presented in Section 4.3. Note that, it is also possible to employ a mesh-free method to calculate the fluid flow field. However, it is beyond the scope of this study and thus not discussed in detail.

During the coupling calculation, one key issue that must be mentioned is the time step, because Δt_{CFD} and Δt_{DEM} are not the same in general. Δt_{CFD} is determined by the CFL criterion [302], whereas Δt_{DEM} can be additionally limited by physical conditions like the Rayleigh wave speed of force transmission on the surface of elastic bodies [301]. Therefore, an artificial technique is needed to make the simulations of two types synchronized. Owen et al. [303] suggested that when $\Delta t_{CFD} < \Delta t_{DEM}$, both the time steps can be determined by the smaller one, Δt_{CFD} . It is clear that this treatment further reduces Δt_{DEM} that is needed to produce a sufficiently stable DEM solution. On the other hand, a more commonly encountered case is $\Delta t_{CFD} > \Delta t_{DEM}$. In this case, to match the physical time of both sides, it is suggested that a sub-cycling treatment can be employed which executes several consecutive DEM time steps in only one CFD time step. During the sub-cycling

process, the hydrodynamic force and torque on the solid particle are not updated in unchanged flow fields. One should be very careful to pick the sub-cycling number, $\Delta t_{CFD}/\Delta t_{DEM}$, to avoid the particle crossing more than one CFD cell within a single CFD time step, because the hydrodynamic force and torque may vary greatly in different cells. Otherwise, a remapping of the particle into the flow field is required.

4.2. Averaged volume method

The most popularly employed AVM model is to couple a solver of the averaged Navier-Stokes equations and DEM, which is also called the combined discrete and continuum model (CCDM) [37]. The modeling of DEM is at the individual particle level, while the fluid flow by CFD is at the computational cell level. There are ongoing discussions on the formulations of the local averaged Navier-Stokes equations for modeling fluid-particle multiphase flows [304]. Traditionally, there are two commonly used models available: Model A and Model B [304]. The two models are mathematically equivalent but have different fluid pressure gradient terms when coupling with DEM. It has been indicated that there is little discrepancy between the two models when simulating mono-sized particles in fluidization, whereas they could produce very different results for the fluidization of binary particle mixtures [301, 305]. Kafui et al. [301] argued that the results by Model A are more consistent with observations and empirical correlations. On the other hand, Feng and Yu [305] suggested that the Model B is more favored. More recently, Zhou et al. [304] presented a comprehensive study of different model formulations and their applicability.

In this section, we do not intend to delve into this matter, but rather we would present the formulas of Model B below:

$$\frac{\partial(\varepsilon_f \rho_f)}{\partial t} + \nabla \cdot (\varepsilon_f \rho_f u_f) = 0 \quad (20)$$

$$\frac{\partial(\varepsilon_f \rho_f)}{\partial t} + \nabla \cdot (\varepsilon_f \rho_f u_f \otimes u_f) = -\nabla p + \nabla \cdot \varepsilon_f \tau_f + (1-\varepsilon_f) \nabla p - n_e \varepsilon_f F_{pf} + \varepsilon_f \rho_f g \quad (21)$$

where u_f and ρ_f are the fluid velocity and density, respectively. ε_f is the bed porosity, p is the fluid pressure, τ_f is the viscous stress, g is the gravitational acceleration, n_e is the number of particles in one fluid cell, $F_{pf} =$

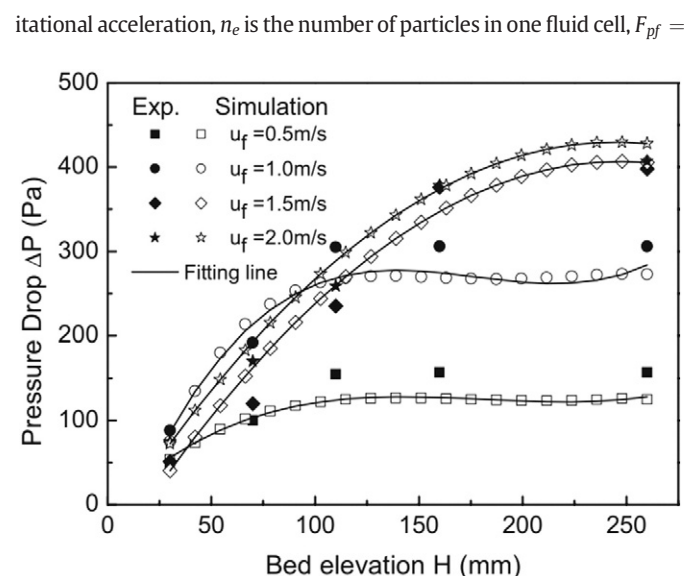


Fig. 35. Comparison of simulated pressure drops of bed elevation with experiments at different superficial gas velocities (adapted from [135], Copyright 2009, with kind permission from WILEY-VCH Verlag GmbH & Co. KGaA).

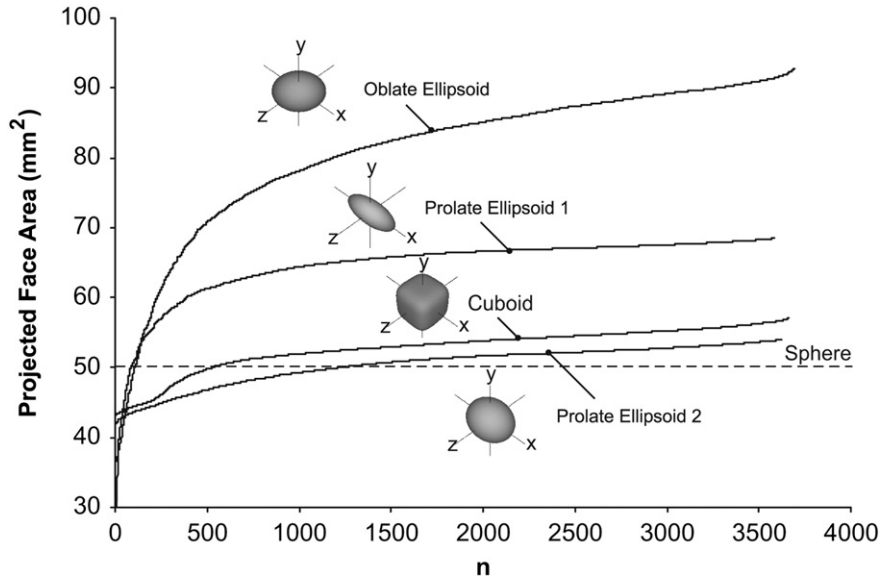


Fig. 36. Cumulative distribution of projected face area for particle index n in the initial flow direction for the four types of super-quadratic particles and sphere (adapted from [95], Copyright 2010, with kind permission from Elsevier).

$\frac{\sum_{i=1}^{N_c} F_{pf,i}}{\Delta V}$ and $F_{pf,i} = F_{D,i} + F_{L,i}$, where $F_{D,i}$ and $F_{L,i}$ are the drag and lift forces, ΔV is the volume of the CFD cell and N_c is the number of particles in the cell.

From numerical point of view, the coupling scheme for the non-spherical DEM and CFD could be very similar to that for spherical particles, but it uses the modified empirical formulas for hydrodynamic forces which consider the geometric difference of the exact particle geometry from a standard spherical ball as introduced in Section 3. Hereafter, two additional key points required to conduct a non-spherical AVM-DEM simulation are introduced.

4.2.1. Determination of flow projected area

From the formulas in Section 3.2.2, it is not difficult to find out that the drag force is proportional to the projected area. For spherical particles, the projected area can be directly calculated by $A_{\perp} = \pi d^2/4$. For non-spherical particles, more factors should be considered because the drag

force depends on particle orientation. Above equation can be still used; however, A_{\perp} is then calculated based on the projected cross-sectional area of the particle onto the velocity vector $|\mathbf{u}_f - \mathbf{u}_p|$. For each particle, the simplest way is to calculate the projected particle rim [95] as shown schematically in Fig. 16. For example, the normal equation of a super-quadratic particle is defined as:

$$n(\theta, \phi) = \begin{bmatrix} \frac{1}{a_x} \cos^{(2-q)} \theta \cos^{(2-q)} \phi \\ \frac{1}{a_y} \cos^{(2-q)} \theta \sin^{(2-q)} \phi \\ \frac{1}{a_z} \sin^{(2-q)} \end{bmatrix} \quad (22)$$

From above equation, the formula given below can be obtained:

$$\theta(\phi) = \arctan \left[\left(-\frac{a_z}{u_{fz}} \frac{u_{fx}}{a_x} \cos^{(2-q)} \phi + \frac{u_{fy}}{a_y} \sin^{(2-q)} \phi \right) \right]^{1/(2-q)} \quad (23)$$

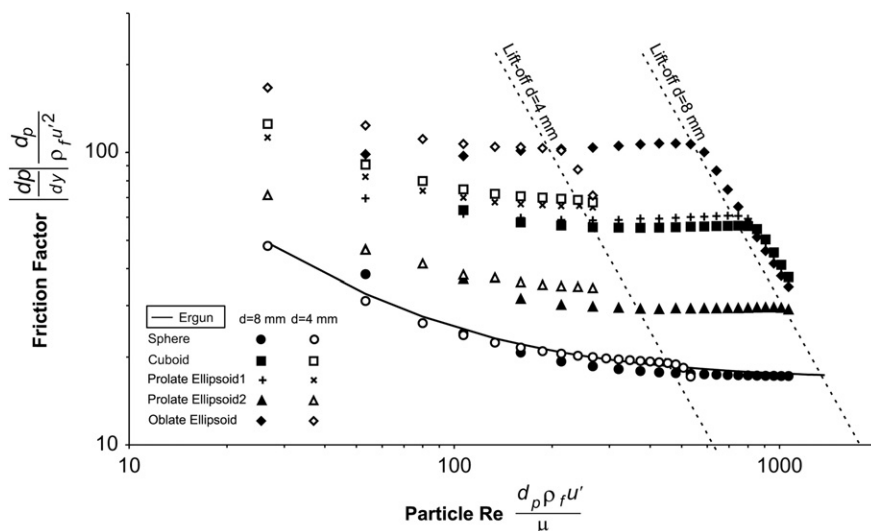


Fig. 37. Non-dimensional friction factor against Reynolds number for 4 and 8 mm volume equivalent diameter particles (adapted from [95], Copyright 2010, with kind permission from Elsevier).

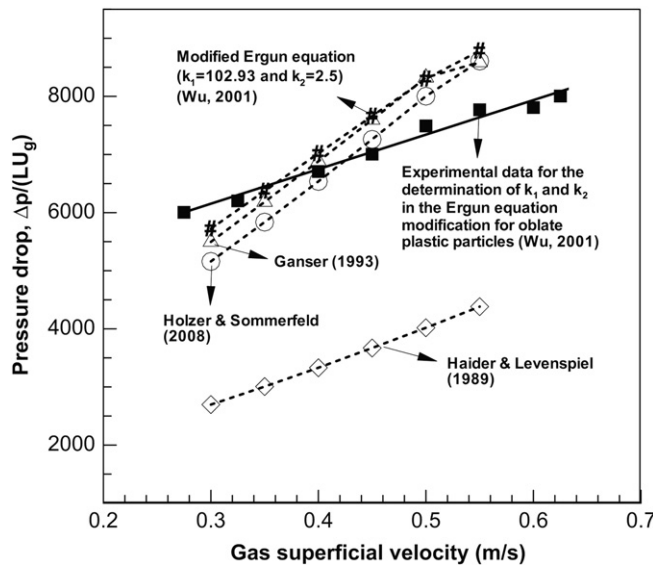


Fig. 38. The relationship between pressure drop and gas superficial velocity for different drag correlations (adapted from [34], Copyright 2011, with kind permission from Elsevier).

A Gram-Schmitt orthogonalisation can be performed on the points given by Eq. (23) to make a 2D projection onto the surface normal to the velocity. According to reference [95], the area can be numerically evaluated by subdividing this projected rim further into small segments and then summing them up.

In the case where complex shape particles are constructed by regular ones, iterative procedures can be used to numerically evaluate the projected area. For example, the cross-sectional area A_{\perp} of each regular particle is calculated and then tabulated based on the three symmetric Eulerian parameters and the sign of a fourth parameter [306]. Therefore, when treating clustered spheres, the individual regular particles are mapped on the xy-, yz- and xz-planes. Based on a 2D-Cartesian grid, whose size is chosen according to the projected particle size, it is checked for all grid cell centers that the respective point is lying within one of the sphere projections. The total projection area can be calculated using the accumulated grid area. Two examples for the calculation of the projection area of a clustered particle with varying orientation are given in Fig. 17. As shown in the top and bottom figures, respectively, totally different projection area could be obtained from the same object when mapped onto different planes or with different orientations which is the unique feature of a non-spherical particle.

4.2.2. Determination of porosity

The local porosity plays an important role in determining the drag force. The coarsest way to calculate the porosity is to consider the particle as entirely included in a fluid cell if the centroid of the particle is

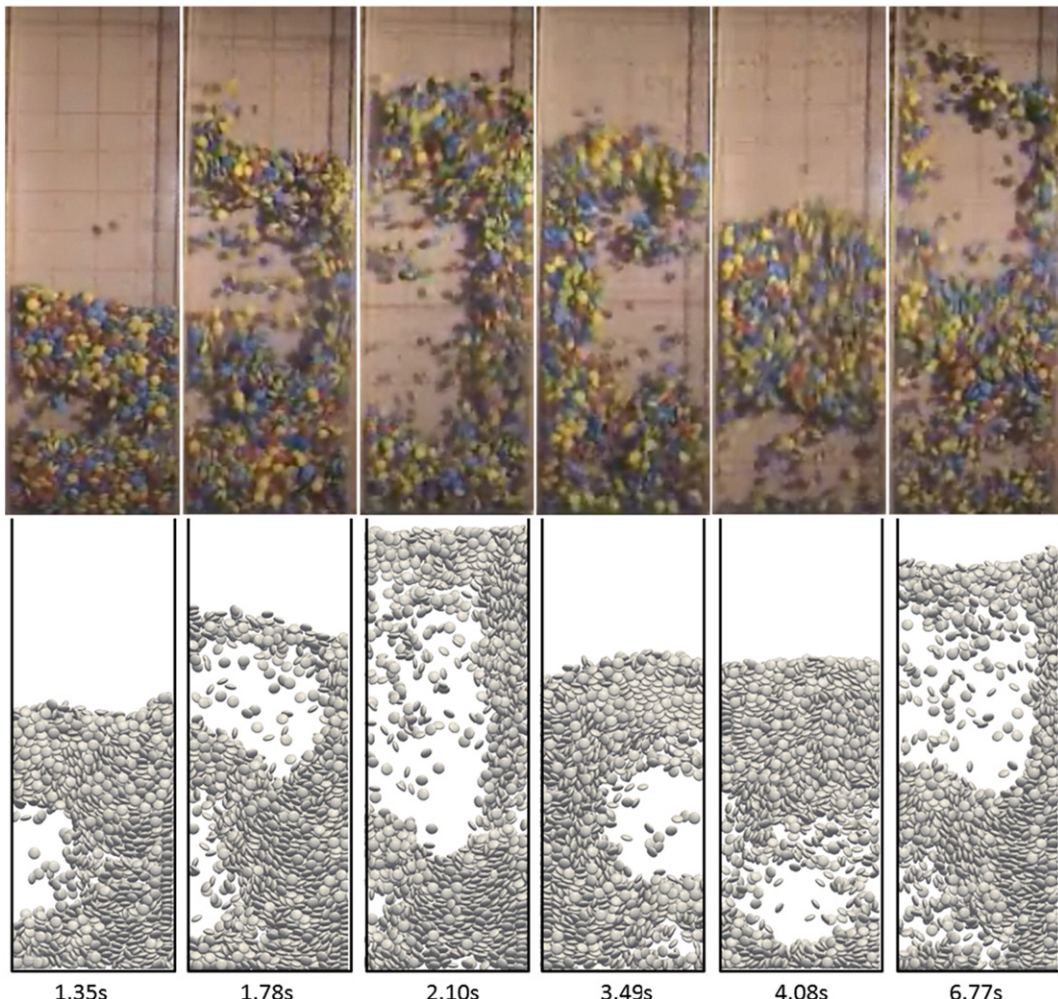


Fig. 39. (a) Comparison of snapshots of solid flow patterns observed in the experiments (the top figures) and CFD-DEM simulations (the bottom figures) (adapted from [34], Copyright 2011, with kind permission from Elsevier).

mapped into that cell. But obviously, the drawback of this method is that it can result in jumps in the porosity as the particles cross CFD cells, which can reduce the smoothness of the numerical solution. The so-called polyhedron method dresses up a particle by a cube whose side lengths are equal to the particle diameter. The volume of intersection of this cube with the CFD cell is calculated and adjusted to conserve the particle volume. The efficiency of this method is worse than the previous one, but it has the advantage to monitor changes in porosity smoothly. However, the errors increase when dealing with non-spherical particles using the polyhedron method.

The calculation of an accurate porosity is quite necessary for successfully simulating a system containing non-spherical particles. Moreover, the set of constitutive equations may include the time derivative of the porosity. Therefore, it is essential to guarantee the numerical stability using a temporally smooth porosity. One good option is to use the octree method proposed by Hilton et al. [95]. For the sake of clarity, a schematic of the algorithm is shown in Fig. 18 for a 2D case. The idea behind the method is to sub-divide the CFD cell into four sub-cells (eight in 3D) and then remove free spaces. The sub-cells that are occupied by solid

particles will be further sub-divided until an empty or the least occupied volume is reached. For example, a minimum volume size of $(\frac{1}{8})^5 \approx 3 \times 10^{-5}$ times the volume of the bounding cell was chosen as the termination criteria in the implementation of Hilton et al. [95]. However, as shown in Fig. 18, the treatment introduces a stepwise representation on the original shape which is not accurate enough to get a temporally smooth solution by simply summing up the squares (cubes in 3D). Therefore, an additional calculation is carried out on those terminating cells that are partly occupied by solid particles, by linearly approximating the volume fraction. Among the aforementioned three ways to calculate the porosity, the last one is the most accurate one although it requires the highest computational effort. It has been indicated by Hilton et al. [95] that the overall increase in the computational time for calculating the porosity and fluid calculations is around a factor of three compared to a single-phase DEM simulation. Of course, this efficiency also depends on the actual particle shape.

Furthermore, to correctly reflect the actual dynamic behavior, a two-dimensional porosity needs to be transferred to a three-dimensional one when conducting two-dimensional simulations. An example of a

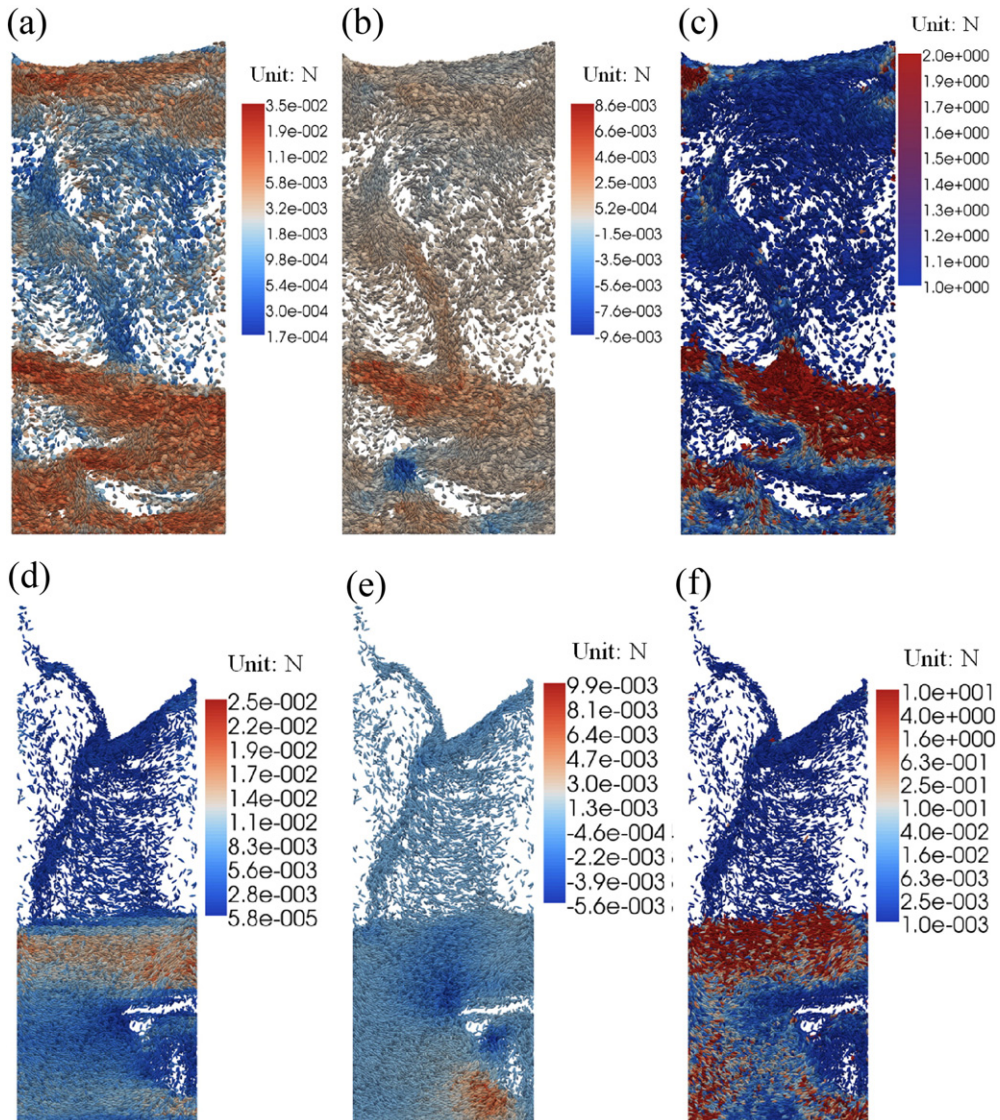


Fig. 40. Snapshots of solid flow pattern with different forces when aspect ratio is 0.25 (top) and 3.5 (bottom): (a) and (d), drag force in the vertical direction; (b) and (e), drag force in the horizontal direction; and (c) and (f), particle-particle contact force (adapted from [34], Copyright 2010, with kind permission from Elsevier).

commonly used formula, the following can be given [299]:

$$\varepsilon_{f,3D} = 1 - \frac{2}{\sqrt{\pi\sqrt{3}}} (1 - \varepsilon_{f,2D})^{3/2} \quad (24)$$

4.3. Immersed Family Methods

Unlike in the case of AVM, the size of a solid particle in IFM is larger than one single CFD cell, and thus, it is too coarse to simply map the particle center into CFD cells. In this sense, the hydrodynamic force between particles and fluid should be obtained based on the exact fluid-solid interaction process along the particle surface. Since the flow field in the vicinity of the particle surface is resolved at a scale comparable with the particle spacing, IFM is theoretically regarded as the most accurate method and may be the only theoretical tool capable of studying these non-linear and geometrically complicated phenomena [205]. As shown in Fig. 14, there are a number of available solvers for the coupled IFM-DEM simulations. IFM here represents the common idea to immerse the particle surface into the flow field and treat it as a moving solid boundary. Hereafter, we list two typical IFM-DEM coupling schemes, one of which depends on two sets of independent meshes (LBM) while the other depends on one set of moving mesh (DNS).

4.3.1. Immersed boundary method

A popular way to perform simulations is by using two sets of meshes. The communication between the two meshes is carried out through numerical interpolation. On one hand, the hydrodynamic forces and torques on a particle are calculated based on the velocity difference between the two phases. On the other hand, the original flow field is disturbed by the movement of the solid particles. In this subsection, we mainly focus on the LBM-DEM coupling scheme in relation to the Immersed Boundary Method (IBM) [307].

We consider simulating incompressible Newtonian fluids where the LBM-DEM model [308] is adopted. The nine lattice velocities are set as:

$$e_i = \begin{cases} (0, 0, 0)c & i = 0 \\ (\cos[(i-1)\pi/2], \sin[(i-1)\pi/2])c & i = 1, 2, 3, 4 \\ \sqrt{2}(\cos[(i-5)\pi/2 + \pi/4], \sin[(i-5)\pi/2 + \pi/4])c & i = 5, 6, 7, 8 \end{cases} \quad (25)$$

where c is the lattice speed. The LBM governing equation known as the lattice Bhatnagar-Gross-Krook model is:

$$f_i(r + e_i \delta_t, t + \delta_t) = f_i(r, t) - \frac{f_i(r, t) - f_i^{eq}(r, t)}{\tau} + F_b \delta_t \quad (26)$$

where $f_i(r, t)$ is the fluid density distribution function, $r = (x, y)$ represents the space position vector, t is time and τ is the non-dimensional relaxation time, and $F_b \delta_t$ denotes the fluid-solid interaction forcing term. The equilibrium density distribution function $f_i^{eq}(r, t)$, can be written as:

$$f_i^{eq}(r, t) = \rho_f \omega_i \left[1 + 3(e_i \cdot u_f) + \frac{9}{2}(e_i \cdot u_f)^2 - \frac{3}{2}|u_f|^2 \right] \quad (27)$$

where the values of weights are: $\omega_0 = 4/9$, $\omega_i = 1/9$ for $i = 1 - 4$ and $\omega_i = 1/36$ for $i = 5 - 8$. u_f denotes the macro velocity at each lattice node which can be calculated by $u_f = (\sum_{i=0}^8 f_i e_i) / \rho_f$, and the macro fluid density is obtained by $\rho_f = \sum_{i=0}^8 f_i$.

In the early LBM works, to handle fluid-particle interaction systems [293,294], the numerical boundary of solid particles were considered to be located approximately at the mid-points of the lattices when a particle boundary intersects with the CFD mesh. Again, this stepwise

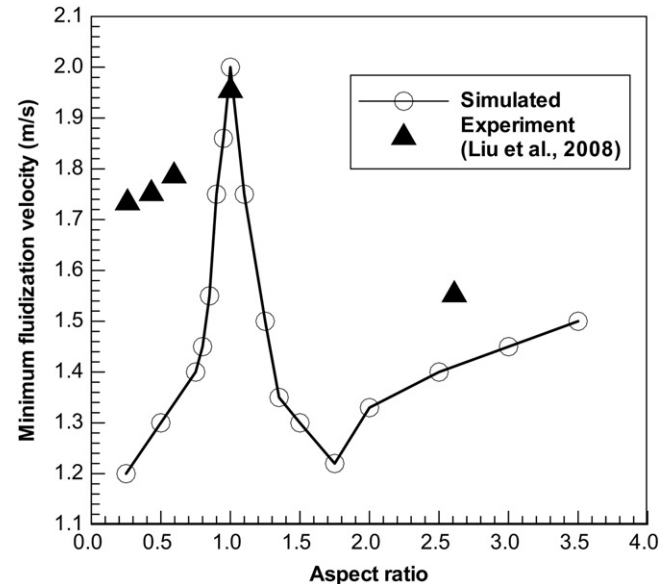


Fig. 41. Effect of aspect ratio on the minimum fluidization velocity (adapted from [34], Copyright 2010, with kind permission from Elsevier).

representation is too coarse to handle the coupling accurately, which may cause numerical oscillations on the hydrodynamic force when the particles move fast. Similar to Section 4.2.2, Noble and Torczynski [309] proposed an Immersed Moving Boundary (IMB) method to smoothen the surface curve, where the Lagrangian points on solid particles are regarded as located at the intersection points of the particle boundary and CFD mesh. The area fraction of the CFD cell covered by a particle is used to calculate the fluid-solid interaction force by ensuring the no-slip boundary condition on the particle surface. However, as it

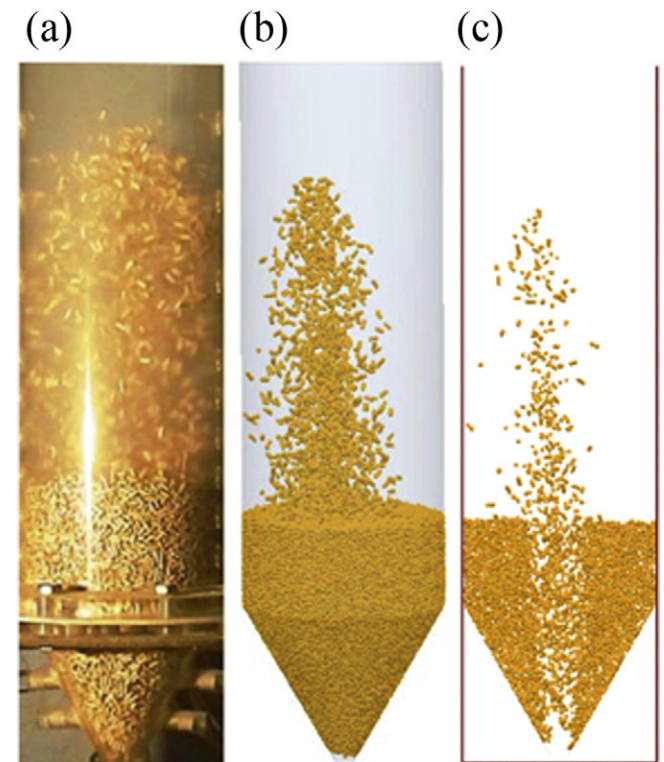


Fig. 42. Flow patterns: (a) experiments; (b) 3D simulation result; and (c) slice view at the centre of the bed (adapted from [15], Copyright 2014, with kind permission from John Wiley & Sons publications).

turned out in IMB, a re-calculation of the Lagrangian point position is still needed at each time step, which is fairly time consuming. In recent years, the more notable method for handling complex and moving boundaries is the IBM proposed by Peskin [307] originally for the numerical analysis of blood flows. In IBM, a particle is represented by a set of independent points, and thus the positions of the Lagrangian points can be simply derived by the particle position and orientation momentarily. Since the hydrodynamic force is calculated on each Lagrangian point, the total force and torque over the particle are found by considering the summation of the change of momentum given by each of the Lagrangian points that belong to the particle. As for the acting points of the force and torque, the readers are referred to Table 7. At present, a number of particle fluid interaction schemes are available for the coupled LBM-IBM-DEM simulations. The first coupling technique was proposed by Feng and Michaelides [310] via a penalty method to calculate the fluid-solid interaction force, which was next improved by using a direct forcing scheme [311]. Niu et al. [312] proposed an approach to compute the force, in which the forcing term is simply calculated by the momentum exchange method. These three schemes are briefly introduced below while several improvements based on them are reported in references [279,313,314].

4.3.1.1. Penalty method. In the scheme of Feng and Michaelides [310], the particle boundary is assumed to be deformable with a high stiffness constant. The numerical and physical particle boundaries are not the same, which is called a 'distortion' in the paper. The displacement

between the numerical boundary and reference points, $\zeta_j = x_j - x_j^r$, is defined, where the exponent r refers to the reference points. This displacement is used to calculate the hydrodynamic force, which is responsible for restoring the boundary point back to the reference position and expressed as follows:

$$F_{pf,j} = \begin{cases} 0 & \|\zeta_j\| = 0 \\ -k\zeta_j & \|\zeta_j\| > 0 \end{cases} \quad (28)$$

where k is the spring constant. Since k is an artificial parameter, one should be cautious when using this linear model because a user-defined spring parameter may have a significant effect on the computational efficiency and accuracy.

4.3.1.2. Direct forcing method. To eliminate the need for determining an artificial stiffness coefficient, Feng and Michaelides [311] proposed a more efficient and direct numerical method called 'Proteus'. In the 'Proteus' method, the forcing term is determined by solving the Navier-Stokes equations using the following explicit scheme:

$$F_i^{(n+1)} = \rho_f \left(\frac{u_{fi}^{(n+1)} - u_{fi}^{(n)}}{\Delta t} + u_{fi}^{(n)} u_{fi,i}^{(n)} \right) - \mu u_{fi,jj}^{(n)} + p_i^{(n)} \quad (29)$$

where $u_{fi}^{(n)}$ is the fluid velocity in the i th direction at current time step n and the subscripts and derivatives follow the Einstein notation. The

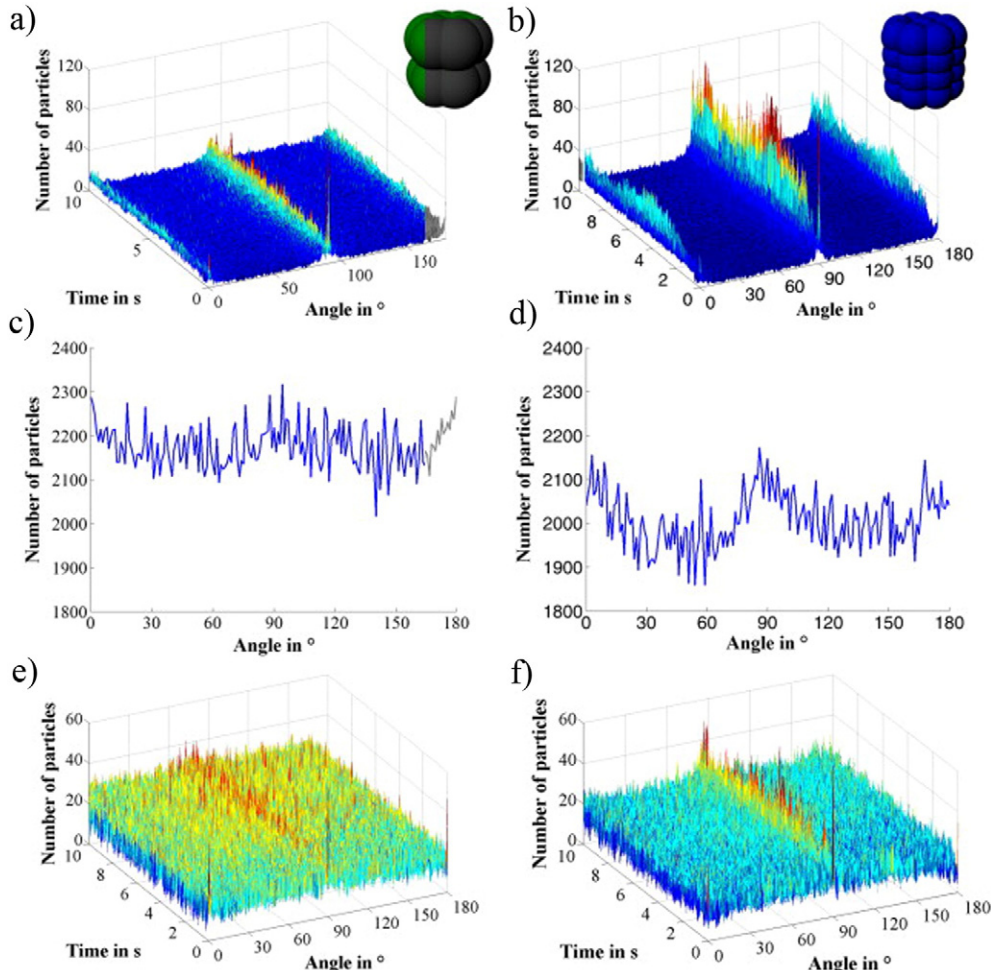


Fig. 43. Distribution of the particle orientation for particle approximations with 12 (a, c, e) and 36 (b, d, f) spheres: (a, b) Orientation in the outer perimeter close to the front and rear wall, (c, d) time summarized orientation in the inner region based on the projection on the x-y-plane and (e, f) orientation over time in the inner area based on a projection on the x-z-plane (adapted from [214], Copyright 2014, with kind permission from Elsevier).

velocity on the particle surface should obey the no-slip boundary condition, and thus is equal to the particle velocity, $U_{BCi}^{(n+1)}$. Therefore, the local density force can be expressed as below:

$$F_i^{(n+1)} = \rho_f \left(\frac{U_{BCi}^{(n+1)} - u_{fi}^{(n)}}{\Delta t} + u_{fi}^{(n)} u_{fi,i}^{(n)} \right) - \mu u_{fi,ij}^{(n)} + p_i^{(n)} \quad (30)$$

where superscript represents the time step, and μ and p are the fluid viscosity and pressure, respectively. Since there are no artificial parameters defined in Eq. (30), this method is termed the direct forcing method.

4.3.1.3. Momentum exchange-based method. Niu et al. [312] proposed an efficient approach to compute the force where the forcing term is calculated by the momentum exchange method. The density distribution functions on the boundary points are obtained from surrounding fluid nodes using

$$f_i(X_l, t) = \sum_{ij} \left(\prod_{k=1, k \neq i}^{i_{\max}} \frac{X_l - x_{kj}}{x_{ij} - x_{kj}} \right) \left(\prod_{m=1, m \neq j}^{j_{\max}} \frac{Y_l - y_{im}}{y_{ij} - y_{im}} \right) f_i(r_{ij}, t) \quad (31)$$

where $X_l(X, Y)$ is the coordinates of the Lagrangian boundary points. The distribution function will be modified by the velocity of the solid particle as follows:

$$f_{-i}(X_l, t + \delta_t) = f_i(X_l, t) - 2\omega_\alpha \rho_f \frac{e_\alpha \cdot U_{BC}}{c_s^2} \quad (32)$$

where $-i$ denotes the opposite direction of i , U_{BC} is the particle velocity. The force density $F(X_l, t)$ at the boundary point can be calculated by:

$$F_i = - \sum_{-i} e_{-i} [f_{-i}(X_l, t) - f_i(X_l, t)] \quad (33)$$

4.3.2. Direct numerical simulation

Another method is to represent the particle geometry using moving CFD meshes, as shown in Fig. 19, which are updated with the movement of solid particles [315]. Monitoring of the solid particles using moving grids was first conducted by Hu et al. [296]. Thereafter, Hu's team has continuously updated their method to conquer the primitive drawbacks [205,316]. In the initial model of Hu et al. [296], a so-called Arbitrary Lagrangian-Eulerian (ALE) moving mesh technique responsible for remeshing and projection was used to treat the time-dependent domain which is determined by the moving particle boundaries. For avoiding numerical instabilities, the forces and torques based on the flow field at the previous time step are imposed on the particles at each time step. The particle positions, angular orientations and the mesh point positions are calculated explicitly while the fluid and particle velocities are calculated implicitly. The calculation procedure consists of the following phases: initialization, updating, re-meshing and projection and using a Navier-Stokes solver. Then, the procedure was improved by incorporating the ALE scheme for determining fluid velocities implicitly by solving a set of Laplace equations [205].

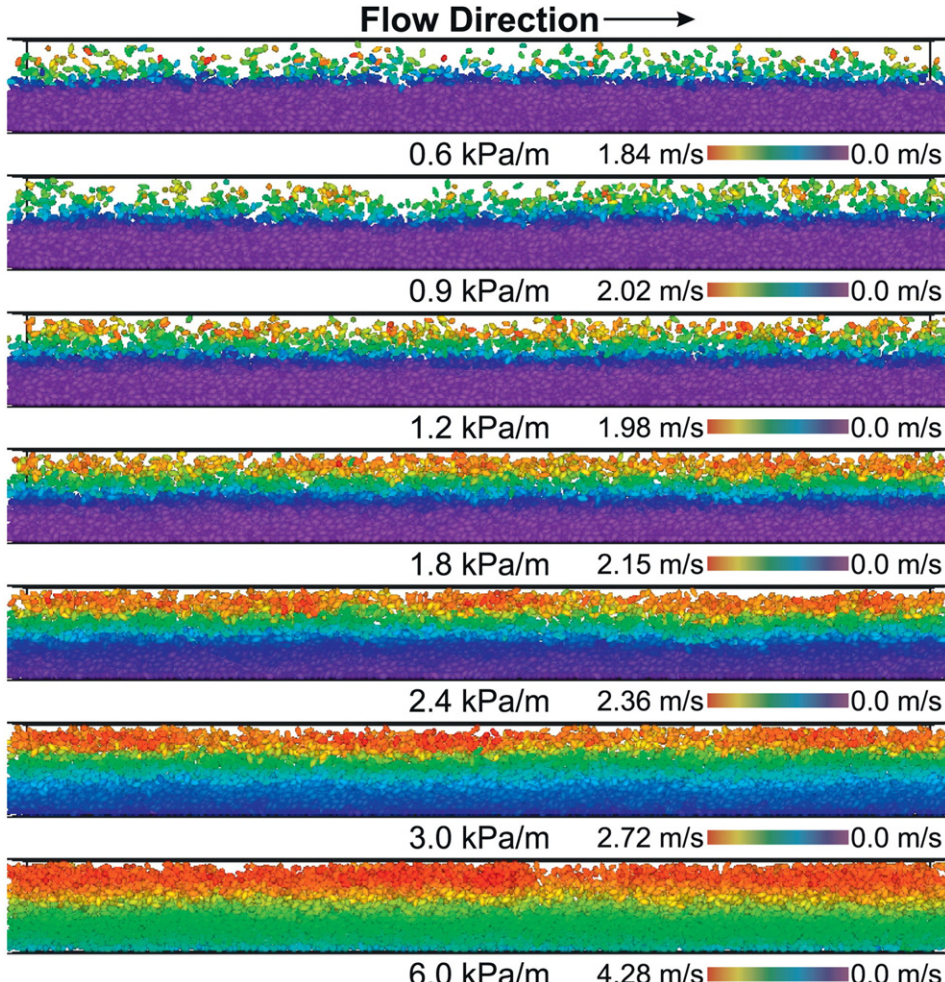


Fig. 44. Cross-section of the particle bed for prolate ellipsoidal particles. Pressure gradients from 0.6 to 6.0 kPa/m are shown. The particles are shaded by relative velocity magnitude (Adapted from [96], Copyright 2010, with kind permission from Elsevier).

In the DNS method, the nodes are distinguished as fluid and boundary ones, respectively. The hydrodynamic force and torque on a solid particle are directly calculated by the local velocity close to the boundary nodes. That is, as soon as the boundary nodes are determined at each time-step, the fluid velocity on these locations are interpolated and the stress tensor is obtained. Then, one can calculate the forces and torques on every segment of the surface and evaluate the total force [317] based on the following Gauss integral formula:

$$\int_{\Gamma_t} (\sigma \cdot n) \cdot \omega d\Gamma = \int_{\Omega_t} \rho_f \left(\frac{\partial u_f}{\partial t} + u_f \cdot \nabla u_f \right) \cdot \omega d\Omega + \int_{\Omega_t} \sigma(p, u_f) : \nabla \omega d\Omega \quad (34)$$

where ω is a vector-valued weighting function that is zero everywhere except on the boundary of the particle Γ . One can let $\omega = \omega_1 i$ for computing F_x , and $\omega = \omega_2 j$ for computing F_y , where ω_1 and ω_2 are each unity at the nodes on Γ and zero at any other nodes. By considering different weighting vectors ω as above and using numerical integration, the force acting on the solid particle can be obtained as follows:

$$F = F_x i + F_y j = \int_{\Gamma} \sigma \cdot n d\Gamma \quad (35)$$

The advantage of the DNS method to handle two-phase systems is that the actual particle shape can be vividly described by the fitting moving meshes. Further, the force distribution on the particle surface becomes noticeable, which plays a key role in controlling its motion in fluid. This information is especially critical for non-spherical particles.

Feng et al. [289,290] conducted DNS to study the motion and interaction of circular and elliptical particles in a Newtonian fluid in the cases of sedimenting, Couette, and Poiseuille flows. Huang et al. [317] numerically examined the turning couples on an elliptic particle settling in a channel of viscous fluid where the ellipse could oscillate under the action of vortex shedding. Hu [318] investigated the rotation of a circular cylinder settling in a viscous liquid between two parallel plates with

the considerations being given to two cases where the cylinder would settle either close to wall or away from it. Feng et al. [319] performed DNS on the motion of elliptic capsules carried by a Poiseuille flow in a channel and analyzed the mechanisms of the lifting of fast-moving capsules in pipelines. However, in the DNS method, the number of mesh points is extremely large, especially in 3D cases. Both a high-speed movement and approximation between particles could cause too frequent updating of the mesh generation, which is extremely time-consuming. Significant effort is needed to prevent serious mesh distortions from happening. Furthermore, the inter-particle collisions could not be treated properly in DNS. All such drawbacks limit the application of DNS mainly in the investigations on liquid-particle interaction problems.

5. Applications

In this section, the applications of the non-spherical modelling method are reviewed, considering the cases of particle packing, particle flows and particle-fluid flows. The hopper discharge flow and rotating drum are reviewed in detail as the typical cases of particle flows. The particle-fluid flows include the fluidized bed, pneumatic conveying and channel flow. Other applications related to non-spherical modelling are also introduced in this section.

5.1. Particle packing and sandpile formation

Particle packing is important, and numerous examples in nature and industries testify to this fact. In the past, extensive research based on DEM has been carried out for investigating the packing of uniform spheres [36]. However, the packing of particles is affected by many variables, among which particle shape is one important parameter. Investigating packing of non-spherical particles possibly has its origins in as early as 1940s [320].

One important topic in this area is to study the relationship between the packing fraction and particle shape. In 1990s, Matuttis et al. [62,321] simulated the packing of convex polygonal particles by a 2D DEM model and found that the angle of repose was dependent on the size dispersion

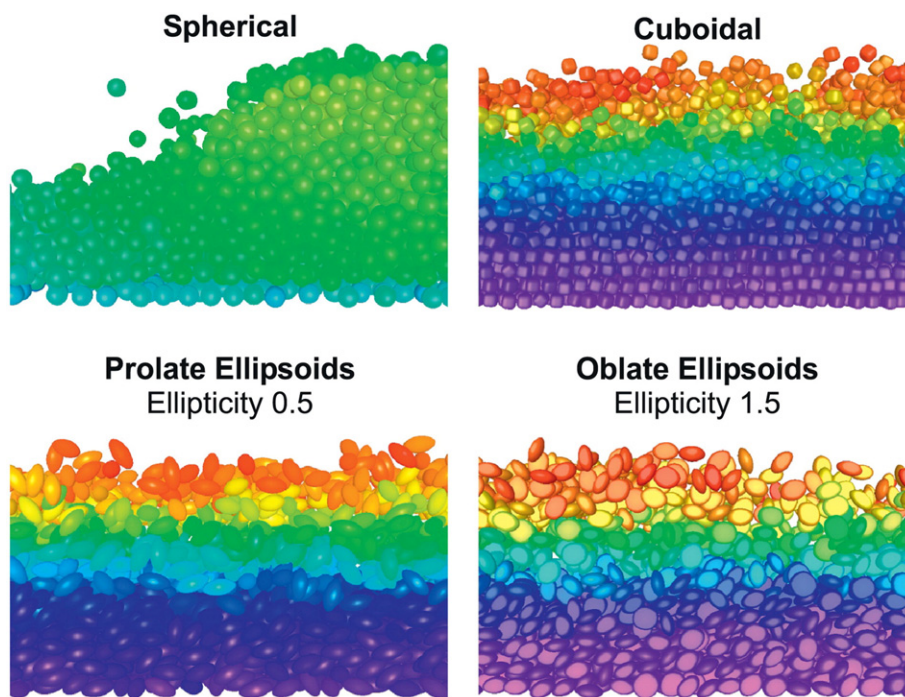


Fig. 45. Cross-section of the particle bed for prolate ellipsoidal particles.; (b) Bed cross-section for shaped particles at the steady state, particles shaded by relative velocity magnitude (Adapted from [96], Copyright 2010, with kind permission from Elsevier).

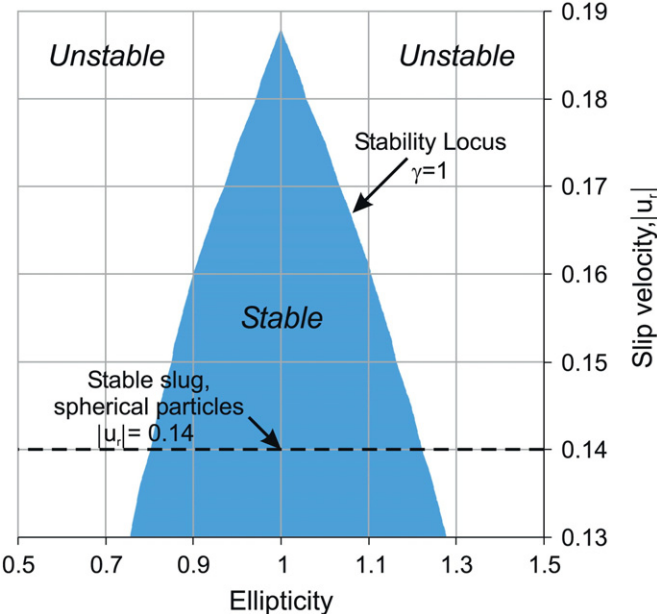


Fig. 46. Stability for slip velocity and aspect ratio, note the shaded region will form stable slug. (Adapted from [96], Copyright 2010, with kind permission from Elsevier).

of particles. When mixing with circular particles, the more eccentric the polygons were, the more pronounced was the dip observed in the vertical stresses. Hidalgo et al. [31,119] presented experimental and 2D DEM studies that investigated the effect of particle aspect ratio on the mechanical and structural properties of granular packing, the aspect ratio being varied from that of a square particle to an elongated one. For grains with maximal symmetry (squares), the stress propagation in the packing was localized, forming chains-like force networks analogous to the ones observed for spherical grains. When depositing cohesive particles, the preferred horizontal orientation disappeared. Zhou et al. [322] investigated piling of paired-spherical particles by a 3D DEM model and found that a pressure profile with a significant pressure dip was obtained for all three models (single layer pile model, planar wedge model and conical pile model) under certain conditions. Chung et al. [323] examined the influence of gravity on the bulk responses of a granular solid for spherical and corn-shaped particles that were constructed by the multi-sphere model using four spherical particles. It was found that the loading gradient was linearly proportional to the gravity and the angle of repose increased when the gravity was reduced. Fraige et al. [53] simulated the packing of cubic particles and spheres

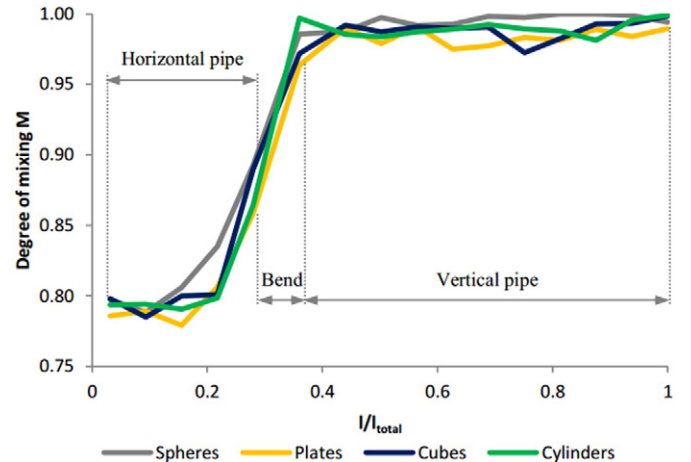


Fig. 48. Degree of mixing M plotted over the dimensionless pipe length for pneumatic conveying [59].

separately and found that the cube-shaped particles showed “better” packing characteristics but “worse” flow properties. However, it was to be noted that the system was fairly small in terms of the number of particles they used and thus, the wall effect played a significant role in this case. Acevedo et al. [324] further investigated the influence of the feeding mechanism on the deposition of smooth cubic particles. The results revealed that, although the final volume fraction was the same, their micromechanical properties were different. Roul et al. [63,325, 326] presented a series of studies on the effective material properties of aggregates consisting of soft convex polygonal particles. They found that the macroscopic stress and fabric tensors were not collinear in the sand pile and that the elastic behaviour was essentially anisotropic. Comparing the vertical normal strain tensors of two types of sand piles qualitatively, the construction histories of the piles were found to affect their strain distributions. Delaney et al. [87] simulated the loose packing of ellipsoidal grains having a high inter-particle friction. Unlike spheres, these cases of packing could not be considered as random because they had a significant degree of orientation-preferred ordering that increased with the aspect ratio of grains. Zhou et al. [88] presented a numerical study on the packing of ellipsoidal particles having different aspect ratios. Fig. 20 shows the packing state for spheroids of three different aspect ratios and their force networks, where each stick represented a normal contact force between a pair of particles. As shown in Fig. 21, the maximum packing fraction occurred at an aspect ratio of 0.6 for oblate spheroids, and 1.80 for prolate spheroids, which meant ellipsoids with either a small or large aspect ratio tend to give a locally ordered

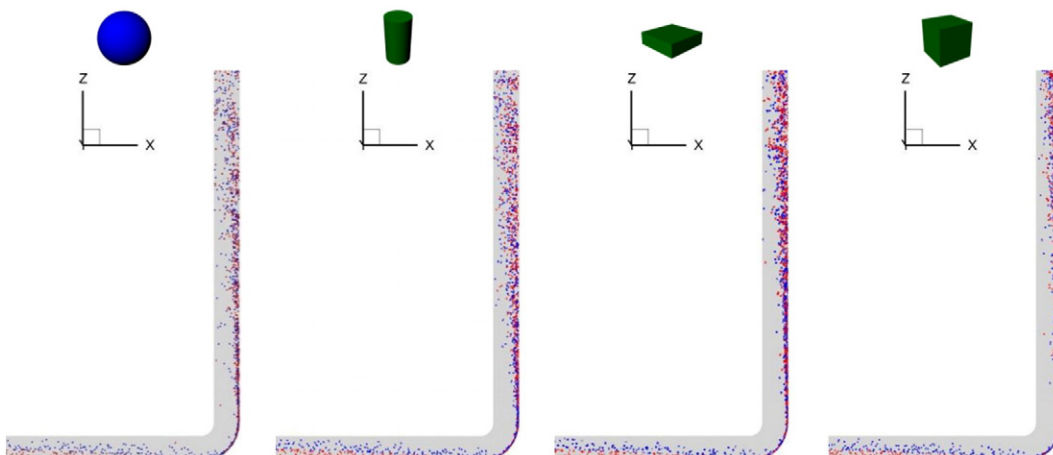


Fig. 47. Snapshots of the mixing process in the pipe bend at $t = 1\text{s}$ for spheres, cylinders, plates and cubes [59].

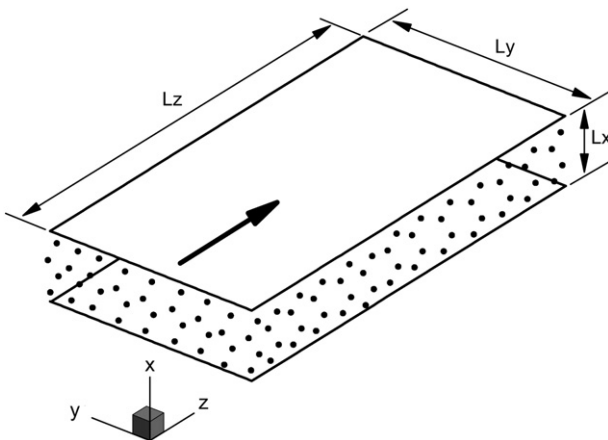


Fig. 49. Schematic of the computational domain of the channel flow [33].

structure. Zhao et al. [327] investigated the effect of particle shape on the packing fraction of randomly-packed cone particles having various aspect ratios (cones, truncated cones and cylinders). The optimal aspect ratios of truncated cones, which gave the highest packing densities, were all around 0.8. The highest packing densities of cylinders and cones were respectively 0.7055 and 0.6664, which were the upper and lower bounds of the packing density of randomly-packed truncated

cones, respectively. Recently, Stenzel et al. [103] found that prolate and oblate ellipsoid particle packings showed a striking similarity between their solid-phase graphs as well as between their pore-phase graphs. As shown in Fig. 22, the whole structures of solid-phase and pore-phase of the ellipsoid packing are extracted to separate graphs for analysing the solid- and pore-phases.

Deng et al. [151] investigated the effects of the particle size, aspect ratio, and cohesiveness on the packing structure. The packing of finer and cohesive particles showed the existence of a single contact between cohesive particles, which was attributed to the formation of a cage structure. As shown in Fig. 23, Dong et al. [44] simulated packing of particles of different shapes, such as disks, cylinders, oblates, prolates, tablets and capsules. Fig. 24 demonstrates that the simulated packing fractions were in good agreement with the experimental and other simulation data for different particle shapes.

Another important topic in this area is the effect of particle shape on the angle of repose during the sandpile formation. Zhu et al. [328] investigated the effect of the particle aspect ratio on the pressure at the bottom of a sandpile. They found that the particles tended to orient in the horizontal direction, which made the contacts to have a tendency of orienting in the vertical direction. Zhou et al. [183] also investigated the effect of particle shape (aspect ratio) on the properties of a sandpile. As shown in Fig. 25, the results confirmed that spheres had the lowest angle of repose. For oblate particles, the angle of repose first increased, then reached a maximum at an aspect ratio of 0.5, and finally decreased. For prolate particles, the angle of repose first increased, and then

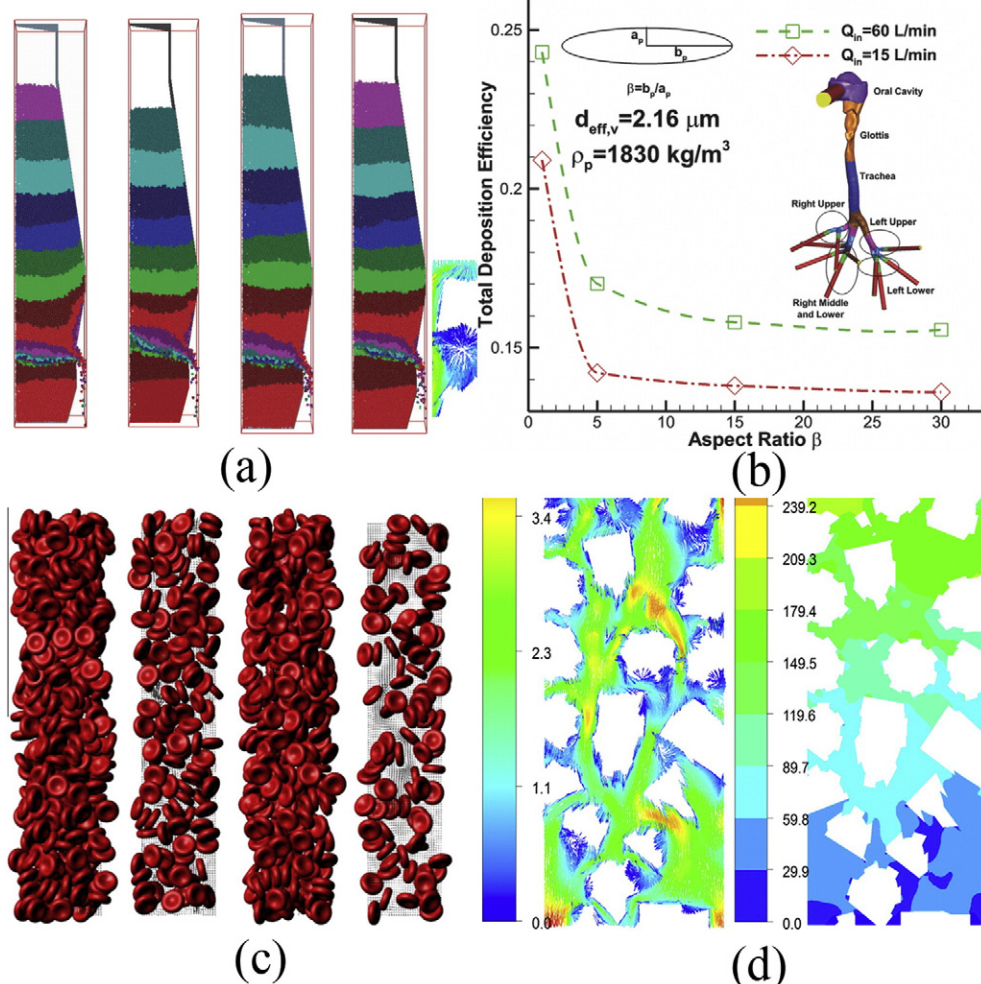


Fig. 50. (a) Pic-slice for spherical and non-spherical particles; (b) Particle deposition efficiency with different aspect ratios; (c) dense suspensions of red blood cells; (d) Contour of velocity and pressure in the chemical looping combustion reactor (Adapted from references [20,343–345], with kind permission from ISIJ, AIP publishing, Elsevier and ACS publication).

became constant after an aspect ratio of 1.8. Recently, Majidi et al. [156] investigated the packing density of irregularly shaped coke particles by the composite approach and found that the voids tracking method based on DEM simulation was an effective tool to study the packing density of granular systems.

Based on all the results and findings listed above, it can be seen that the packing structures of non-spherical particles largely depend on the particle shape. The relationship between the angle of repose (or packing fraction) and aspect ratio shows an M-shaped curve (Figs. 21 and 25). With advances in modelling, more internal mechanisms may be revealed in the future in this research field of packing of non-spherical particles.

5.2. Particle flow

5.2.1. Hopper discharge

Hoppers are widely used in many industrial processes, for example, in mining, metallurgy, and food industries, to name a few. To develop a comprehensive understanding of the granular flow in a hopper, extensive studies have been carried out by means of experimental and numerical approaches. In particular, the DEM modelling plays an important role as it allows a better understanding of the underlying mechanisms [91].

Many works have been carried out to examine the effect of particle shape on the discharge rate using the non-spherical DEM modelling approach since the first DEM simulation of the dynamics of hopper discharge flow in 2D by Kohring et al. [50] in 1995. Cleary et al. [74] further constructed a 3D DEM simulation to identify the relationship between particle shape and hopper discharge rate, indicating a linear decrease in mass flow rate with increasing particle elongation. Following the Cleary's work, Mack et al. [55] and Wang et al. [172] investigated the flow of polyhedral particles in a hopper and found that polyhedral particle flow was generally slightly faster than the spheres; the more angular the particles, the greater the resistance to the forcing load and smaller the flowability. Langston et al. [123] also applied DEM to simulate the flow of non-spherical particles in 3D and found that ellipsoidal particles of an aspect ratio of 5 discharged 40% faster than circles, which was explained by particle alignment yielding a lower resistance to flow. But friction between particles was ignored in their work. Li et al. [122] studied the effect of inter-particle friction, and found that friction had little effect on the discharge rate of spherical particles, but had a significant effect on the discharge rate of disc-like particles. Tao et al. [150, 154] constructed corn-shaped particles by the composite-spheres method to simulate the flow of those particles in a hopper and found that the horizontal velocity of the corn-shaped particles was relatively larger than that of spherical particles. Markauskas et al. [329] investigated the effect of rolling resistance on the flow of rice grains constructed by the composite-spheres method and found that the increase of rolling friction was due to geometric deviations of the particle shape from the symmetrical geometry. Kanzaki et al. [330] found that the discharge flow increased the disorder in elongated particles, which led to a reduction of the vertical stress propagation during the discharge. Höhner et al. [56,58,61] studied the effect of shape representation schemes on the simulation results by using hopper flows of polyhedral particles and ones constructed with the composite-sphere method. As shown in Fig. 26, the shape representation schemes have a minor influence on the final results [58]. As shown in Fig. 27, Liu et al. [91] thoroughly investigated the correlation of discharge rate to aspect ratios using the ellipsoidal particles and found that ellipsoids were not sensitive to boundary walls, and thus they did not experience as significant velocity gradient as spheres. A modified Beverloo equation shown in Fig. 28 was presented to take into account the effect of particle shape.

All the above results show that the particle shape has to be considered as one of the key parameters having a significant effect on the dynamics of hopper discharge flow. The capability of the DEM model to simulate non-spherical particle flows indicates that DEM is in fact a

useful tool to explore the mechanisms of non-spherical particle hopper flows.

5.2.2. Rotating drum

Rotating drums are widely used in many process industries, some examples being food, pharmaceutical, chemical and ceramic processing in the respective industries. The processes include mixing, heating, cooling, drying, and so on. The real shapes of particulate materials in the industries are normally non-spherical, and therefore, the effect of particle shape on the flow regimes of a rotating drum deserves further study.

As shown in Fig. 29, Geng et al. [115] investigated the mixing process of slender particles in a rotating dryer. They found that the overall mixing rate of slender particles was faster than that of spherical particles under the same operating conditions. The results indicated that particle shape had a significant effect on particle mixing in drums, and thus its effect should be considered seriously.

Third et al. [331] simulated the non-spherical particle flow in a horizontal rotating drum, with non-spherical particles being constructed through the multi-sphere model. Based on the tangential velocity profile, they found that the slip could be avoided by adding non-spherical particles. Wachs et al. [48] further demonstrated that the non-spherical particles more easily reached the avalanching regime compared to the spherical particles. Moreover, Fig. 30 shows that their model could simulate the granular flow dynamics of multi-shape mixture of particles consisting of spheres, cylinders, cubes and tetrahedral particles.

Kangi et al. [98] investigated the effects of the media shapes on the behaviours in a dry mill. As shown in Fig. 31, worn-out balls were defined by superquadric models, and cylpebs were modelled using a regular cylindrical shape model. The results showed that the particle shape had a significant effect on the performance of the dry mill. In a subsequent study, Dubé et al. [332] found that aspect ratios larger than 2 could show a deviation from the results for the spherical particle model, for example in the velocity profile and residence time.

The dynamic angle of repose and wall roughness are important parameters that deserve further investigation. Höhner et al. [174] studied the effect of angularity using polyhedrons and smoothed polyhedrons and found that the dynamic angle of repose increased with the angularity. Lu et al. [102] investigated the effect of wall roughness on the cross-sectional flow in a rotating drum and found that wall roughness was a key parameter for preventing the drum slippage in the case of spherical particles; in the case of non-spherical particles, increasing wall roughness decreased the dynamic repose angle of the drum. Pereira et al. [333,334] investigated the effect of particle shape, size and density on the formation of radial streak pattern in a rotating drum. They found that the stable streak patterns occurred when small, dense, non-spherical particles were mixed with large, less-dense, spherical particles. Smeets et al. [69] assessed the computational performance of the proposed method by simulating the motion of constructed particles in a rotating drum (Fig. 32). They found that the computational time greatly increased with the complexity of the particle shapes. Recently, Pei et al. [335] investigated the influence of the particle shape on contact electrification and found that smaller sphericity caused a larger charging coefficient, which led to a faster charge accumulation.

So far, the effect of particle shape (for example, aspect ratio) on the flow regimes of rotating drums has not been fully understood. Further future studies on non-spherical DEM modelling will be needed to fully establish such effects.

5.2.3. Other applications

In addition to the applications mentioned above, the non-spherical DEM model has been also used to study processes (e.g., screening, vibration, coating, impaction, mill, mixing, stress flow, chute flow, and so on). Here, only some relevant published works are introduced and their significant findings are summarised below.

Kruggel-Emden et al. [152] investigated the sieve behaviour of non-spherical particles represented by the composite-sphere method and found that the particle shape had an obvious influence on flow rates and residence time. Ramaoli et al. [336] presented DEM simulation results on order formation among elongated particles when they were vertically vibrated, and the results showed that there were three regimes that correspond with the three energy input levels of low, intermediate and high, respectively. Freireich et al. [2,5] investigated the effect of pharmaceutical tablet shape on the intra-tablet coating using the multi-sphere model. The results showed that the DEM model could qualitatively predict the variability of the intra-tablet coating thickness. Grima et al. [145] simulated the flow of non-spherical particles impinging on a vertical wall and found that numerical results were comparable with experimental ones with regard to the particle trajectories, the velocity before and after the impact and the resultant forces on the wall. Sinnott et al. [337] investigated the grinding performance of non-spherical particles in stirred mills and found that the energy dissipation and wear rate of the screw impeller both showed an increase compared to the spherical particles. Boton et al. [173] simulated the shear strength of non-spherical particles with different flatnesses and found the shear strength increased with the flatness as the anisotropic structure was enhanced. Li et al. [147] modelled the rock flow in a chute and found that the deposition structure had an influence on the flow pattern of the non-spherical particles. Cleary et al. [86] investigated the effect of particle shape on several large-scale industrial processes including vibrating screen, mixer, dragline bucket, transfer chute, cement ball mill and landslide collapse as shown in Fig. 33. Recently, Hua et al. [338] investigated the internal load and moment distribution of the rod-like particles in a vertical mixer and found that the spatial distributions of loads and moments are symmetric about the particle center-plane with a maximum at the particle center-plane.

5.3. Particle-fluid flow

5.3.1. Fluidized bed

Fluidised beds play an important role in physical and chemical processes (e.g. catalysis, drying, granulation, and so on). In the past, extensive studies based on DEM have been presented to clarify the dynamic processes within fluidized beds. However, most of these research works have assumed spherical geometry for the particles, although many experimental works have found that the particle shape has a significant effect on the dynamics of fluidized beds. Recently, the coupled CFD-DEM model for non-spherical particles has shown promise as a method that can be used for investigating the effect of particle shape on flow behaviour in gas fluidisation.

Zhong et al. [135] first reported a CFD-DEM study on the flow of cylinder-shaped particles in a fluidized bed. The cylinder-shaped particle was represented by the composite-sphere method. The drag force coefficient proposed by Tran-Cong et al. [274] was used in this work. As shown in Fig. 34, the gas-solid flow patterns obtained from simulations were comparable with the experimental results. As shown in Fig. 35, the model has been validated using the comparison of pressure drop between simulations and experiments. The results from the simulations showed the inter-particle collisions decreased while particle-wall collisions increased with an increase in the gas velocity.

In addition, the effect of particle shape on minimum fluidization velocity has also been studied by some researchers. Hilton et al. [95] simulated the dynamics of cuboids and three kinds of ellipsoidal particles (with aspect ratios of 0.4~1) in a fluidised bed. The particle shape was represented by 3D super-quadrics method proposed by Cleary et al. [74]. The drag coefficient was calculated by the equation proposed by Hölzer et al. [271], which took into account the projected cross-sectional area onto the fluid velocity vector. Fig. 36 shows the cumulative distribution of the face areas projected perpendicular to the vertical y-axis of particles of different shapes. The correlation of Reynolds number and non-dimensional friction factor plotted in Fig. 37. Fig. 37 indicates that all

non-spherical particle types situated above the Ergun relationship. The results showed that the fluidisation velocity of non-spherical particles was lower than that of spherical particles, which was due to the decreased porosity and increased drag force.

To further investigate the effect of aspect ratio thoroughly, Zhou et al. [34] simulated the fluidisation of ellipsoidal particles with aspect ratios in the range of 0.25–3.5. Four typical correlations shown in Fig. 38 have been proposed to determine the drag coefficient, and have been evaluated by comparing with the experimental results. The results showed that the modified Ergun equation was more suitable for their work. As shown in Fig. 39, the solid flow patterns observed in experiments and CFD-DEM simulations were comparable. Fig. 40 shows the spatial distributions of interaction forces for the aspect ratios, 0.25 and 3.5. Normally, large drag and contact forces appeared in the dense region. It can be seen from Fig. 41 that when the aspect ratio increases from 1.0, the minimum fluidization velocity decreased first and then increased. Interestingly, their results also showed that the orientations of ellipsoidal particles were not random. Oblate particles preferred vertical orientation while prolate particles preferred horizontal orientation.

As shown in Fig. 42, Ren et al. [6,15] presented a series of studies on the dynamic behaviour of corn-shaped and cylindroid particles in a spouted bed. The corn-shaped and cylindroid particles were constructed by the multi-sphere model. Comparison of simulations with experiments showed the ability of the CFD-DEM model in simulating spouting action with non-spherical particles. The key parameters, e.g. gas velocity, spout diameter and geometry of the fountain were varied to investigate their effects. Recently, Oschamann et al. [59,214] investigated the mixing process of elongated particle, such as cylinders, plates and cuboids, in a fluidised bed. As shown in Fig. 43, the results showed that the accuracy of the shape representation had a strong influence on the results as the projected areas got altered. They also found that the mixing time and index of non-spherical particles were lower than those of spherical particles, and elongated particles seemed to take up preferably upright positions. Recently, Vollmari et al. [339,340] investigated the pressure drop of non-spherical particles represented by polyhedron approximation method in a model scale fluidized bed and found that elongated cylinders showed a tendency to align themselves with the flow with increasing superficial velocities.

The above studies have demonstrated that particle shape has a significant effect on the fluidised bed dynamics. Despite the fact that there are some publications of research on non-spherical particles using the coupled CFD-DEM, there are still many issues that are needed to be investigated by non-spherical CFD-DEM simulations in the future.

5.3.2. Pneumatic conveying and channel flow

Pneumatic conveying is a popular approach to rapidly transport large volumes of granular material through a system of pipes using a gas/fluid as the transporting medium. Many studies have demonstrated the CFD-DEM model as a useful tool for investigating the gas-solid flows in pipes. However, there are only few studies that investigate the effects of particle shape on pneumatic conveying performance.

Hilton et al. [96] investigated the effect of particle shape on the pneumatic conveying by coupled CFD-DEM model and found that the particle shape had a significant effect on the flow modes under a given imposed gas flow rate (Fig. 44). The drag coefficient was calculated by the correlation proposed by Hölzer et al. [271]. Super-quadric particles were chosen as the non-spherical particles as they could provide an excellent trade-off between computational speed and shape flexibility [96]. As shown in Fig. 45, the spherical particles formed a slug, but the ellipsoids and the cuboidal particles had a dilute stream of particles over a sheared bed. Compared to spherical particles, Fig. 46 shows that the granular flow regime for non-spherical particles transited directly to dilute flow rather than to a slug flow at high imposed gas velocities.

Oschmann et al. [59] further studied the effect of particle shape on the mixing performance during the pneumatic conveying using a pipe bend (Fig. 47). A polyhedron method was applied to represent the desired particle shape and the CP method was used for contact detection. The results shown in Fig. 48 indicates that the non-spherical particles had a lower degree of mixing than that of spherical particles before they reached the pipe bend as the formation of particle-wall contacts were delayed by non-sphericity of particles. As a fundamental study on the effect of particle shape on the channel flow, Njobuenwu et al. investigated the dynamic behaviour of non-spherical particles in channel flows (Fig. 49) in laminar [341] and turbulent [33,342] regimes using LES-DEM model by simulations. The particle shapes were simulated using the super-quadric method. The results showed that there were distinct differences in the two types of flows for various particle shapes. Especially, the non-spherical particles in the turbulent flow had a broader particle orientation distribution than in the laminar flow due to the effect of turbulent dispersion. As in the case of fluidised beds, the pneumatic conveying of non-spherical particles also needs to be investigated by non-spherical CFD-DEM simulations in the future.

5.3.3. Other applications

In addition to the processes mentioned above, the CFD-DEM model for non-spherical particles has also been used to study the others processes such as material flows in the blast furnace, suspensions of blood cells, depositions in the lung, and chemical reactors. Adema et al. [20] investigated the influence of non-spherical particles on the cohesive zone of a blast furnace. As shown in Fig. 50(a), the simulation results showed that the particle shape had a significant influence on the solid flow pattern. Feng et al. [343] investigated the deposition behaviour of ellipsoidal particles of different aspect ratios in lungs using the human airway-lung model (Fig. 50(b)). They found that the slender particles were more harmful than thicker ones due to their ability to reach deeper regions of the lung at a high breathing rate. Shardt et al. [344] simulated the suspensions of red blood cells using the LBM and found that blood cell particles preferred vertical orientation during sedimentation (Fig. 50(c)). This model needs to be further improved by adding cohesive forces and a modified damping coefficient. Tabib et al. [345] investigated the transport phenomena in gas-flow reactors packed with long cylindrical pellets (aspect ratio 7) by using CFD-DEM simulation and found that the pressure drop increased with increasing aspect ratio (Fig. 50(d)). In general, the CFD-DEM methodology for non-spherical particles offers a new way of understanding numerous particulate phenomena involving practical particle shapes in various fields of interest.

6. Challenges and future research

Numerous efforts mentioned above have shown that DEM/CFD-DEM is a high-potential method to investigate the extensive NSPS by vividly capturing the unique features of non-spherical particles. However, since NSPSs are significantly complex and diverse, there are still many problems in terms of the accuracy, efficiency and universality of non-spherical DEM theory. In addition, due to the limitation of computational resources, most of the current DEM simulations for NSPS still focus on laboratory-scale systems, or are employed to develop local constitutive relations for those coarser numerical approaches (such as Euler-Euler or MP-PIC) which are usually used to deal with large-scale systems in this day. The state-of-the-art DEM simulation technique is far from being perfect enough to accurately deal with real non-spherical particulate systems in nature or industry. Considering all the difficulties to scale up the reactors in various industrial processes and the unsatisfactory performance of the coarser numerical approaches in NSPS, further development of non-spherical DEM towards engineering-scale systems is undoubtedly of great interest. From the perspectives of the non-spherical DEM theory and its application, the

main challenges and possible future efforts towards the development of a non-spherical model are mainly summarized as follows:

- Model developments in the non-spherical DEM

As mentioned above, a wide range of methods have been proposed for describing particle shapes and detecting particle contacts. However, each of these methods has its own distinct advantages and disadvantages regarding the accuracy, flexibility, numerical stability and efficiency. Huge challenges still exist in the non-spherical DEM especially when handling the extensive NSPS in the real world, some example being the NSPS with particles of concave-shapes, heterogeneous sizes, various shapes, and so on. Therefore, to explore and develop more efficient and robust methods to represent different particle shapes and detect their contacts is still one of the most interesting areas to focus on in the near future. Additionally, there is an urgent need for more accurate and general models to describe the contact forces between the non-spherical particles. Currently, the usual practice to compute the contact force in the non-spherical DEM is directly using the models that are originally established for the ideal spherical particles. In fact, for non-spherical particles, especially those with sharp corners, edges and flat faces, the contact force is quite complicated and closely related to the contact geometry including the contact area (or volume) and the specific geometry of overlap region. Finally, research effort should also focus on seeking far more efficient methods for multi-phase and multi-physics problems which are often complexly coupled together. As mentioned in this paper, the current CFD-DEM coupling methods can be briefly divided into two categories: namely the AVM-DEM and IFM-DEM. The AVM-DEM has more superior computational convenience to involve more particles in the simulations. However, it is not so competent (at least for now) to consider the actual particle geometry exactly due to the major assumptions in evaluating the particle-fluid interaction force. Various correlations have been proposed to describe the drag and lift forces acting on non-spherical particles. However, their practical verification and application in the AVM-DEM simulations are extremely rare. On the contrary, the IFM-DEM could produce detailed CFD information around a particle surface, but significantly suffers from its high computational burden. Therefore, the current IFM-DEM model is more suitable for small scale simulations with fundamental research targets. With the rapid development of the computational techniques, the IFM-DEM will draw more and more attentions. In this regard, the combination of these two schemes might be currently a promising choice to filter multiple shapes and sizes of particles into AVM or IFM in one system. Another interesting method is the combination of Lattice-Boltzmann (LB) and DEM. As recently shown by Rong et al. [346–348], this method can lead to the formulation of more accurate equations to calculate the drag forces for spheres and their mixtures, and for ellipsoidal particles too. The approach should be extended to more complicated non-spherical particles in the future.

Heat transfer characteristics occurring in the NSPS are also of paramount importance in the processes like chemical, environmental, food, mineral and process industries though not detailed in this paper. The particle shape has proven to influence on the overall heat transfer coefficient [349,350] greatly both by changing the flow structure and heat transfer behaviour, but the effect has not been quantified yet. Apart from those correlations (such as the drag force model) in the coupling of CFD and spherical DEM [351,352], additional important issues should be carefully considered to involve the effects of particle shape, some examples being the Nusselt number in the convective heat transfer [353], the contacting surface in the conductive heat transfer [354] and the particle surface area in the radiative heat transfer [354]. In general, there is still limited numerical work in the NSPS with heat transfer, and thus, it is a topic of choice for the next wave of research and development.

- Large-scale systems and parallel computation

Another great challenge DEM faces is the huge computational cost when simulating large-scale particulate systems. When a multi-phase system is taken into account, the computational effort further increases heavily. With the conventional computational resources, e.g., a typical PC hardware or workstation, three-dimensional DEM simulations are usually limited to systems with particle numbers not exceeding 10^5 [355]; for non-spherical particulate systems, only the range of 100 to 10000 particles has been achieved. How to accelerate the computations has always been very crucial for DEM, since in realistic systems the number of particles often surpasses 10^9 [356], which is much beyond the particle number traditional computational capacities would allow.

With recent developments in computer technology, parallel computing has shown great potential in accelerating computer simulations and overwhelmingly replaced the attempt to increasing CPU (Central Processing Unit) clock speed [357,358]. The most successful instances of parallel processing architectures are multi-core CPU and GPU (Graphic Processing Unit), and their typical applications to speed up DEM-simulations are reported in Table 8. However, a high-end multi-core CPU in the latest PC or compute clusters indicate good speedup performance only with 8~48 cores, beyond which speedup gains are swamped by the high network latencies for inter-process communications [359,360]. Fortunately, GPU, with massively parallel architecture and the development of its programming tools, such as CUDA (Compute Unified Device Architecture) technology, provides new possibilities for large-scale DEM simulations. Based on the multi-thread parallel computation in GPU, DEM simulation is becoming realistic to handle spherical particulate systems having particle numbers reaching 10^8 ~ 10^9 , which is already of practical interest to engineering applications [361]. However, in DEM simulations of NSPS, attempts at GPU acceleration are still very limited. Typically, Longmore et al. [362], Govender et al. [358,363,364] and Gan et al. [365] respectively reported their efforts to simulate tetrahedral lattices, convex polyhedrons and ellipsoids with the DEM running on GPU, as shown in Table 8. The maximum number of particles can reach 3.4×10^7 , but the authors pointed out that their GPU framework of BLAZE-DEM is limited to applications of simplified interactions, and the computational time is still considerable [364]. Additionally, all of the reports have not involved the multi-phase systems.

Obviously, GPU-based multi-threaded parallel computation is one of the most promising techniques to accelerate the DEM simulations. However, to date GPU-DEM is still fairly new technology compared to the traditional CPU platform and its development is very inadequate especially in the simulations of NSPS. Therefore, efforts to develop GPU-DEM to simulate NSPS or even to deal with the real engineering systems are highly recommended in the decades to come. Before that, many detailed problems need to be solved. For example, new DEM algorithms suited to the threading model of GPU are needed, and the GPU optimized collision analysis algorithm for non-spherical particles and efficient memory usage method may be the most crucial requirements. When simulating gas-solid systems, efficient coupling algorithm between CFD and DEM is very important; otherwise, the data exchange between the CPU-based CFD and GPU-based DEM will be considerably time-consuming.

7. Summary

In summary, theoretical development is the foundation that guarantees the rationality of the model. A universal contact detection method for particles of arbitrary shape is essential to study flow dynamics of multi-shape particles. But it is still a challenging task in non-spherical DEM. Actually this is a geometric problem which is beyond the scope of DEM. The accurate solution of interaction forces between fluid and non-spherical particles is the key step and also is significantly a tough

challenge for non-spherical AVM-DEM coupling method. The development of parallel computing codes (MPI, CUDA and OpenMP) and high performance computing resource (GPU) may extend the ability of IFM-DEM to simulate the engineering processes. Overall, the non-spherical modeling has a bright future as it offers a new way of understanding the many particle-related phenomena in industrial handling of particles of various shapes. However, the key evaluating factors such as the robustness, accuracy, speed and versatility of the numerical technique need to be improved in the future.

Nomenclature

a_i	Acceleration of particle i , m/s
a, b	Half-length of the principal axes of 2D superquadric curves, m
a_1, a_2, a_3	Half-length of the principal axes of 3D superquadric, m
$\mathbf{a} \mathbf{b} \mathbf{c}$	Normal vector of plane of potential particles, -
A_{ij}	Overlap area, m^2
A_p	Projected area, m^2
A_{\perp}	Cross-section area, m^2
b_w	Contact width, m
C_D	Drag coefficient, -
C_L	Lift coefficient, -
c	Parameter of circularity, -
d	Distance or diameter, m
d_A	Surface equivalent sphere diameter, m
d_n	Volume-equivalent-sphere diameter, m
e	Particle collision coefficient of restitution, -
e_1, e_2	Shape powders of the 2D superquadric curves, -
E	Young's elastic modulus, Pa
F	Force, N
G	Position of the center of gravity, -
g	Gravitational acceleration, m/s^2
I	Inertia tensor, kg/m^2
k	Material stiffness constant, N/m
K_n	Spring stiffness constant, N/m
K_1, K_2	Shape factors in low and high Reynolds number regions, respectively
L	Length of object, m
m_i	Quality of particle i , kg
\mathbf{n}	Normal vector, -
N	Number of characteristic elements considered, -
O	Center of gravity of a particle, -
p	Pressure, Pa
P_c	Probability of contact
P_p	Projected perimeter of particle, m
r, R	Radius of shape, m
R_{ij}	Reduced radius, m
Re	Reynolds number, -
Re_p	Particle Reynolds number, -
S	Area, m^2
t	Time, s
\mathbf{t}	Tangential vector, -
\mathbf{T}	Torques, Nm
\mathbf{u}	Angular acceleration, rad/s^2
\mathbf{u}, \mathbf{v}	Vectors of velocity, m/s
V_{ij}	Overlap volume, m^3
\mathbf{W}	Angular velocity in body-fixed frame, rad/s
\mathbf{w}	Angular velocity in inertia frame, rad/s
V	Potential function, -
\mathbf{x}	Displacement vector, m
Y	C_D/Re , -
x, y, z	Coordinates, -

Greek letters

α, ϑ, β	Parametric angles, degree
β_{pf}	Gas-solid interphase drag coefficient, -
χ	Voidage function exponent, -

δ	Overlap or displacement, m
$\dot{\delta}$	Contact overlap speed, m/s
ε	Characteristic energy, -
ε	Porosity, -
$\varepsilon_1, \varepsilon_2$	Squareness parameters of the 3D superquadric, -
φ	Sphericity, -
φ_{\perp}	Crosswise sphericity, -
φ_{\parallel}	Lengthwise sphericity, -
γ	Contact dissipation coefficient, N/m
μ	Fluid viscosity, Pa·s
σ	Roundness, -
π_i	Overall angular momentum, kg·m ² /s
θ_m, ϕ_m	Parametric angles of a discretised point, degree
θ	Vectors of orientation, -
$\phi\theta\psi$	Euler angular, -
ρ	Density, kg/m ³
σ	Poisson ratio, -
ς	Area of a cell, m ²
ξ, η	Coefficients of viscosity associated with the deformation of the volume and shear, -
ζ_j	Displacement between the reference point and the boundary point, m
Γ	Dimensionless rotational speed of the sphere, -
Λ	Transformation matrix, -
Ω	Rotate speed, rad/s

Acknowledgements

Financial supports from the NSFC for Distinguished Young Scholars (No. 51325601), Major Program of NSFC (No. 51390492) and Joint Funds of NSFC (No. U1560205) are sincerely acknowledged.

References

- [1] S. Torquato, Y. Jiao, Dense packings of the Platonic and Archimedean solids, *Nature* 460 (2009) 876–879.
- [2] B. Freireich, W.R. Ketterhagen, C. Wassgren, Intra-tablet coating variability for several pharmaceutical tablet shapes, *Chem. Eng. Sci.* 66 (2011) 2535–2544.
- [3] W.R. Ketterhagen, Modeling the motion and orientation of various pharmaceutical tablet shapes in a film coating pan using DEM, *Int. J. Pharm.* 409 (2011) 137–149.
- [4] D. Suzuki, G. Toschhoff, S. Radl, D. Machold, S.D. Fraser, B.J. Glasser, J.G. Khinast, DEM simulation of continuous tablet coating: Effects of tablet shape and fill level on inter-tablet coating variability, *Chem. Eng. Sci.* 69 (2012) 107–121.
- [5] B. Freireich, R. Kumar, W. Ketterhagen, K. Su, C. Wassgren, J.A. Zeitler, Comparisons of intra-tablet coating variability using DEM simulations, asymptotic limit models, and experiments, *Chem. Eng. Sci.* 131 (2015) 197–212.
- [6] B. Ren, W. Zhong, Y. Chen, X. Chen, B. Jin, Z. Yuan, Y. Lu, CFD-DEM simulation of spouting of corn-shaped particles, *Particuology* 10 (2012) 562–572.
- [7] W. Jittanit, G. Srzednicki, R.H. Driscoll, Comparison Between Fluidized Bed and Spouted Bed Drying for Seeds, *Dry. Technol.* 31 (2013) 52–56.
- [8] Z. Zhan, L. Yaoming, L. Zhenwei, G. Zhiqiang, DEM simulation and physical testing of rice seed impact against a grain loss sensor, *Biosyst. Eng.* 116 (2013) 410–419.
- [9] M. Marek, S. Wojciech, K. Iwona, T. Małgorzata, B. Ireneusz, Drying characteristics of barley grain dried in a spouted-bed and combined Ir-convection dryers, *Dry. Technol.* 25 (2007) 1621–1632.
- [10] W. Jittanit, G. Srzednicki, R. Driscoll, M.O. Carvalho, P.G. Fields, C.S. Adler, Modeling of seed drying in fluidised and spouted bed dryers, *Julius-Kühn-Archiv* 28 (2010) 275–280.
- [11] B. Ren, W. Zhong, B. Jin, Y. Shao, Z. Yuan, Numerical simulation on the mixing behavior of corn-shaped particles in a spouted bed, *Powder Technol.* 234 (2013) 58–66.
- [12] Y. Shao, W. Zhong, X. Chen, Y. Chen, B. Jin, Spouting of non-spherical particles in conical-cylindrical spouted bed, *Can. J. Chem. Eng.* 92 (2014) 742–746.
- [13] H. Krugel-Emden, F. Sudbrock, S. Wirtz, V. Scherer, Experimental and numerical investigation of the bulk behavior of wood pellets on a model type grate, *Granul. Matter* 14 (2012) 681–693.
- [14] Q. Guo, X. Chen, H. Liu, Experimental research on shape and size distribution of biomass particle, *Fuel* 94 (2012) 551–555.
- [15] B. Ren, W. Zhong, X. Jiang, B. Jin, Z. Yuan, Numerical simulation of spouting of cylindroid particles in a spouted bed, *Can. J. Chem. Eng.* 92 (2014) 928–934.
- [16] M.H. Abbaspour-Fard, Theoretical Validation of a Multi-sphere, Discrete Element Model Suitable for Biomaterials Handling Simulation, *Biosyst. Eng.* 88 (2004) 153–161.
- [17] M. Amutio, G. Lopez, M. Artetxe, G. Elordi, M. Olazar, J. Bilbao, Influence of temperature on biomass pyrolysis in a conical spouted bed reactor, *Resour. Conserv. Recycl.* 59 (2012) 23–31.
- [18] J.G. Peacey, W.G. Davenport, The iron blast furnace: theory and practice, Pergamon Press, 1979.
- [19] S. Gupta, D. French, R. Sakurovs, M. Grigore, H. Sun, T. Cham, T. Hilding, M. Hallin, B. Lindblom, V. Sahajwalla, Minerals and iron-making reactions in blast furnaces, *Prog. Energy Combust. Sci.* 34 (2008) 155–197.
- [20] A.T. Adema, Y. Yang, R. Boom, Discrete Element Method-Computational Fluid Dynamic Simulation of the Materials Flow in an Iron-making Blast Furnace, *ISIJ Int.* 50 (2010) 954–961.
- [21] M. Barz, Sewage sludge combustion in a spouted bed cascade system, *China Particuology* 1 (2003) 223–228.
- [22] N. Paterson, Y. Zhuo, G.P. Reed, D.R. Dugwell, R. Kandiyoti, pyrolysis and gasification of sewage sludge in a spouted bed reactor, *Water Environ. J.* 18 (2004) 90–95.
- [23] A. Adegoroye, N. Paterson, X. Li, T. Morgan, A.A. Herod, D.R. Dugwell, R. Kandiyoti, The characterisation of tars produced during the gasification of sewage sludge in a spouted bed reactor, *Fuel* 83 (2004) 1949–1960.
- [24] M. Olazar, R. Aguado, D. Vélez, M. Arabiourrutia, J. Bilbao, Kinetics of scrap tire pyrolysis in a conical spouted bed reactor, *Ind. Eng. Chem. Res.* 44 (2005) 3918–3924.
- [25] M.J.S. Jose, S. Alvarez, A.O.D. Salazar, A. Morales, J. Bilbao, M.J.S. Jose, Treatment of cork wastes in a conical spouted bed reactor, *Int. J. Chem. React. Eng.* 4 (2006) 80–90.
- [26] M. Thamavithya, A. Dutta, An investigation of MSW gasification in a spout-fluid bed reactor, *Fuel Process. Technol.* 89 (2008) 949–957.
- [27] G. López, M. Olazar, R. Aguado, J. Bilbao, Continuous pyrolysis of waste tyres in a conical spouted bed reactor, *Fuel* 89 (2010) 1946–1952.
- [28] M. Amutio, G. Lopez, M. Artetxe, Valorisation of waste tires by pyrolysis over a FCC catalyst in a conical spouted bed reactor, *Pres International Conference on Process Integration Modelling & Optimisation for Energy Saving & Pollution Reduction*, 29, 2012, pp. 817–822.
- [29] J.P. Latham, A. Munjiza, The modelling of particle systems with real shapes, *Philos. Trans. A Math. Phys. Eng. Sci.* 362 (2004) 1953–1972.
- [30] M.A. Knuth, J.B. Johnson, M.A. Hopkins, R.J. Sullivan, J.M. Moore, Discrete element modeling of a Mars Exploration Rover wheel in granular material, *J. Terramech.* 49 (2012) 27–36.
- [31] R.C. Hidalgo, I. Zuriguel, D. Maza, I. Pagonabarraga, Role of particle shape on the stress propagation in granular packings, *Phys. Rev. Lett.* 103 (2009) 118001.
- [32] G.W. Delaney, R.D. Morrison, M.D. Sinnott, S. Cummins, P.W. Cleary, DEM modeling of non-spherical particle breakage and flow in an industrial scale cone crusher, *Miner. Eng.* 74 (2015) 112–122.
- [33] D.O. Njobuenwu, M. Fairweather, Dynamics of single, non-spherical ellipsoidal particles in a turbulent channel flow, *Chem. Eng. Sci.* 123 (2015) 265–282.
- [34] Z.Y. Zhou, D. Pinson, R.P. Zou, A.B. Yu, Discrete particle simulation of gas fluidization of ellipsoidal particles, *Chem. Eng. Sci.* 66 (2011) 6128–6145.
- [35] Y. Guo, C. Wassgren, B. Hancock, W. Ketterhagen, J. Curtis, Granular shear flows of flat disks and elongated rods without and with friction, *Phys. Fluids* 25 (2013) 63304.
- [36] H.P. Zhu, Z.Y. Zhou, R.Y. Yang, A.B. Yu, Discrete particle simulation of particulate systems: A review of major applications and findings, *Chem. Eng. Sci.* 63 (2008) 5728–5770.
- [37] H.P. Zhu, Z.Y. Zhou, R.Y. Yang, A.B. Yu, Discrete particle simulation of particulate systems: Theoretical developments, *Chem. Eng. Sci.* 62 (2007) 3378–3396.
- [38] G. Lu, J.R. Third, C.R. Müller, Discrete element models for non-spherical particle systems: From theoretical developments to applications, *Chem. Eng. Sci.* 127 (2015) 425–465.
- [39] A. Džiugys, B. Peters, An approach to simulate the motion of spherical and non-spherical fuel particles in combustion chambers, *Granul. Matter* 3 (2001) 231–266.
- [40] C. Hogue, Shape representation and contact detection for discrete element simulations of arbitrary geometries, *Eng. Comput.* 15 (1998) 374–390.
- [41] P.A. Cundall, O.D.L. Strack, A discrete numerical model for granular assemblies, *Geotechnique* 29 (1979) 47–65.
- [42] O.R. Walton, Particle-dynamics calculations of shear flow, in: J.T. Jenkins (Ed.), *Mechanics of Granular Materials: New Models and constitutive Relations*, Elsevier Science, Amsterdam 1983, pp. 327–338.
- [43] C. Hogue, D. Newland, Efficient computer simulation of moving granular particles, *Powder Technol.* 78 (1994) 51–66.
- [44] K. Dong, C. Wang, A. Yu, A novel method based on orientation discretization for discrete element modeling of non-spherical particles, *Chem. Eng. Sci.* 126 (2015) 500–516.
- [45] J.R. Williams, R.O. Connor, Discrete element simulation and the contact problem, *Arch. Comput. Methods Eng.* 6 (1999) 279–304.
- [46] M. Mando, L. Rosendahl, On the motion of non-spherical particles at high Reynolds number, *Powder Technol.* 202 (2010) 1–13.
- [47] F. Jin, H. Xin, C. Zhang, Q. Sun, Probability-based contact algorithm for non-spherical particles in DEM, *Powder Technol.* 212 (2011) 134–144.
- [48] A. Wachs, L. Girolami, G. Vinay, G. Ferrer, Grains3D, a flexible DEM approach for particles of arbitrary convex shape- Part I: Numerical model and validations, *Powder Technol.* 224 (2012) 374–389.
- [49] J.R. Williams, A. Pentland, Superquadrics object representation for dynamics of multi-body structures, *Proceedings of ASCE Structures*, San Francisco, CA, 1989.
- [50] G.A. Kohring, S. Melin, H. Puhl, H.J. Tillemans, W. Verm Hlen, Computer simulations of critical, non-stationary granular flow through a hopper, *Comput. Methods Appl. Mech. Eng.* 124 (1995) 273–281.
- [51] A.A. Mirghasemi, L. Rothenburg, E.L. Matyas, Influence of particle shape on engineering properties of assemblies of two-dimensional polygon-shaped particles, *Geotechnique* 52 (2002) 209–217.
- [52] D. Zhao, E.G. Nezami, Y.M.A. Hashash, J. Ghaboussi, Three-dimensional discrete element simulation for granular materials, *Eng. Comput.* 23 (2006) 749–770.
- [53] F.Y. Fraige, P.A. Langston, G.Z. Chen, Distinct element modelling of cubic particle packing and flow, *Powder Technol.* 186 (2008) 224–240.
- [54] E. Azema, F. Radjai, R. Peyroux, V. Richefeu, G. Saussine, Short-time dynamics of a packing of polyhedral grains under horizontal vibrations, *Eur. Phys. J. E Soft Matter* 26 (2008) 327–335.
- [55] S. Mack, P. Langston, C. Webb, T. York, Experimental validation of polyhedral discrete element model, *Powder Technol.* 214 (2011) 431–442.

- [56] D. Höhner, S. Wirtz, V. Scherer, Experimental and numerical investigation on the influence of particle shape and shape approximation on hopper discharge using the discrete element method, *Powder Technol.* 235 (2013) 614–627.
- [57] H. Kruggel-Emden, T. Oschmann, Numerical study of rope formation and dispersion of non-spherical particles during pneumatic conveying in a pipe bend, *Powder Technol.* 268 (2014) 219–236.
- [58] D. Höhner, S. Wirtz, V. Scherer, A study on the influence of particle shape on the mechanical interactions of granular media in a hopper using the Discrete Element Method, *Powder Technol.* 278 (2015) 286–305.
- [59] T. Oschmann, K. Vollmar, H. Kruggel-Emden, S. Wirtz, Numerical Investigation of the Mixing of Non-spherical Particles in Fluidized Beds and during Pneumatic Conveying, *Procedia Eng.* 102 (2015) 976–985.
- [60] S. Zhao, X. Zhou, W. Liu, Discrete element simulations of direct shear tests with particle angularity effect, *Granul. Matter* 17 (2015) 793–806.
- [61] D. Höhner, S. Wirtz, V. Scherer, A numerical study on the influence of particle shape on hopper discharge within the polyhedral and multi-sphere discrete element method, *Powder Technol.* 226 (2012) 16–28.
- [62] H.G. Matuttis, S. Lüding, H.J. Herrmann, Discrete element simulations of dense packings and heaps made of spherical and non-spherical particles, *Powder Technol.* 109 (2000) 278–292.
- [63] P. Roul, A. Schinner, K. Kassner, Simulation of the strain distribution under a two-dimensional sand pile, *Powder Technol.* 214 (2011) 406–414.
- [64] A.A. Peña, R. García-Rojo, H.J. Herrmann, Influence of particle shape on sheared dense granular media, *Granul. Matter* 9 (2007) 279–291.
- [65] J. Ghaboussi, R. Barbosa, Three-dimensional discrete element method for granular materials, *Int. J. Numer. Anal. Methods Geomech.* 14 (1990) 451–472.
- [66] J. Eliáš, DEM simulation of railway ballast using polyhedral elemental shapes, particle-based methods III: fundamentals and applications, Proceedings of the 3rd International Conference on Particle-based Methods, Fundamentals and Applications, Stuttgart, Germany 2013, pp. 247–256.
- [67] R.E. Barbosa, Discrete element models for granular materials and rock masses, University of Illinois at Urbana-Champaign, IL, 1990.
- [68] D. Müller, T.M. Liebling, Detection of collisions of polygons by using triangulation, *Contact Mechanics*, Springer, US 1994, pp. 369–372.
- [69] B. Smeets, T. Odenthal, S. Vanmaercke, H. Ramon, Polygon-based contact description for modeling arbitrary polyhedra in the Discrete Element Method, *Comput. Methods Appl. Mech. Eng.* 290 (2015) 277–289.
- [70] P.A. Cundall, Formulation of a three-dimensional distinct element model Part I. A scheme to detect and represent contacts in a system composed of many polyhedral blocks, *Int. J. Rock Mech. Min. Sci. Geomech.* 25 (1988) 107–116.
- [71] E.G. Nezami, Y.M.A. Hashash, D. Zhao, J. Ghaboussi, A fast contact detection algorithm for 3-D discrete element method, *Comput. Geotech.* 31 (2004) 575–587.
- [72] E.G. Nezami, Y.M.A. Hashash, D. Zhao, J. Ghaboussi, Shortest link method for contact detection in discrete element method, *Int. J. Numer. Anal. Methods Geomech.* 30 (2006) 783–801.
- [73] J.M. Ting, M. Khwaja, L.R. Meachum, J.D. Rowell, An ellipse-based discrete element model for granular materials, *Int. J. Numer. Anal. Methods Geomech.* 17 (1993) 603–623.
- [74] P.W. Cleary, M.L. Sawley, DEM modelling of industrial granular flows: 3D case studies and the effect of particle shape on hopper discharge, *Appl. Math. Model.* 26 (2002) 89–111.
- [75] J.R. Williams, A.P. Pentland, Object representation for design-unifying cubes and squares, Proceedings of COMPLAS 89, 2nd International Conference on Computational Plasticity, Barcelona, Spain, 1989.
- [76] G.G.W. Mustoe, M. Miyata, Material flow analyses of noncircular-shaped granular media using discrete element method, *J. Eng. Mech.* 127 (2001) 1017–1026.
- [77] P.W. Cleary, The effect of particle shape on simple shear flows, *Powder Technol.* 179 (2008) 144–163.
- [78] P.W. Cleary, G.K. Robinson, M.J. Golding, P.J. Owen, Understanding factors leading to bias for falling-stream cutters using discrete element modelling with non-spherical particles, *Chem. Eng. Sci.* 63 (2008) 5681–5695.
- [79] A.H. Barr, Superquadrics and angle-preserving transformations, *IEEE Comput. Graph. Appl.* 1 (1981) 11–23.
- [80] X. Lin, T. Ng, Contact detection algorithms for three-dimensional ellipsoids in discrete element modelling, *Int. J. Numer. Anal. Methods Geomech.* 19 (1995) 653–659.
- [81] X. Lin, T.T. Ng, A three-dimensional discrete element model using arrays of ellipsoids, *Geotechnique* 319–329 (1997).
- [82] H. Ouadfel, L. Rothenburg, An algorithm for detecting inter-ellipsoid contacts, *Comput. Geotech.* 24 (1999) 245–263.
- [83] L. Vu-Quoc, X. Zhang, O.R. Walton, A 3-D discrete-element method for dry granular flows of ellipsoidal particles, *Comput. Methods Appl. Mech. Eng.* 187 (2000) 483–528.
- [84] T.T. Ng, Shear strength of assemblies of ellipsoidal particles, *Geotechnique* 54 (2004) 659–669.
- [85] Z.Y. Zhou, D. Pinson, R.P. Zou, A.B. Yu, CFD-DEM simulation of gas fluidization of ellipsoidal particles, Proceedings of the Seventh International Conference on CFD in the Minerals and Process Industries, CSIRO, Melbourne, Australia, 2009.
- [86] P.W. Cleary, DEM prediction of industrial and geophysical particle flows, *Particulology* 8 (2010) 106–118.
- [87] G.W. Delaney, J.E. Hilton, P.W. Cleary, Defining random loose packing for non-spherical grains, *Phys. Rev. E Stat. Nonlinear Soft Matter Phys.* 83 (2011) 51305.
- [88] Z. Zhou, R. Zou, D. Pinson, A. Yu, Dynamic simulation of the packing of ellipsoidal particles, *Ind. Eng. Chem. Res.* 50 (2011) 9787–9798.
- [89] J. Gan, Z. Zhou, R. Zou, A. Yu, Discrete element modeling of gas fluidization of fine ellipsoidal particles, *Powders and Grains 2013 - Proceedings of the 7th International Conference on Micromechanics of Granular Media*, 1, AIP Publishing 2013, pp. 1130–1133.
- [90] Z. Zhou, R. Zou, D. Pinson, A. Yu, Discrete modelling of the packing of ellipsoidal particles, *Powders and Grains 2013 - Proceedings of the 7th International Conference on Micromechanics of Granular Media*, 1, AIP Publishing 2013, pp. 357–360.
- [91] S.D. Liu, Z.Y. Zhou, R.P. Zou, D. Pinson, A.B. Yu, Flow characteristics and discharge rate of ellipsoidal particles in a flat bottom hopper, *Powder Technol.* 253 (2014) 70–79.
- [92] M.A. Hopkins, Polyhedra faster than spheres? *Eng. Comput.* 31 (2014) 567–583.
- [93] P.W. Cleary, N. Stokes, J. Hurley, Efficient collision detection for three dimensional super-ellipsoidal particles, Proceedings of 8th international computational techniques and applications conference CTAC97, Adelaide, 1997.
- [94] C. Wellmann, C. Lillie, P. Wriggers, Homogenization of granular material modeled by a three-dimensional discrete element method, *Comput. Geotech.* 35 (2008) 394–405.
- [95] J.E. Hilton, L.R. Mason, P.W. Cleary, Dynamics of gas-solid fluidised beds with non-spherical particle geometry, *Chem. Eng. Sci.* 65 (2010) 1584–1596.
- [96] J.E. Hilton, P.W. Cleary, The influence of particle shape on flow modes in pneumatic conveying, *Chem. Eng. Sci.* 66 (2011) 231–240.
- [97] J.E. Hilton, P.W. Cleary, Raceway formation in laterally gas-driven particle beds, *Chem. Eng. Sci.* 80 (2012) 306–316.
- [98] K. Kiangi, A. Potapov, M. Moys, DEM validation of media shape effects on the load behaviour and power in a dry pilot mill, *Miner. Eng.* 46–47 (2013) 52–59.
- [99] P.W. Cleary, Particulate mixing in a plough share mixer using DEM with realistic shaped particles, *Powder Technol.* 248 (2013) 103–120.
- [100] G.W. Delaney, P.W. Cleary, R.D. Morrison, S. Cummins, B. Loveday, Predicting breakage and the evolution of rock size and shape distributions in Ag and SAG mills using DEM, *Miner. Eng.* 50–51 (2013) 132–139.
- [101] G.W. Delaney, J.E. Hilton, P.W. Cleary, C. Miller, The role of inter-grain friction in determining the mechanical and structural properties of superellipsoid packings, *Powders and grains 2013: Proceedings of the 7th International Conference on Micromechanics of Granular Media*, 1542, AIP Publishing 2013, pp. 361–364.
- [102] G. Lu, J.R. Third, C.R. Müller, Effect of wall rougheners on cross-sectional flow characteristics for non-spherical particles in a horizontal rotating cylinder, *Particulology* 12 (2014) 44–53.
- [103] O. Stenzel, M. Salzer, V. Schmidt, P.W. Cleary, G.W. Delaney, Quantitative structural analysis of simulated granular packings of non-spherical particles, *Granul. Matter* 16 (2014) 457–468.
- [104] Y. Zhu, particle shape effects on dynamic load transfer in granular media, University of Rhode Island, 1996.
- [105] J.R. Williams, A.P. Pentland, Superquadrics and modal dynamics for discrete elements in interactive design, *Eng. Comput.* 9 (1992) 115–127.
- [106] J.F. Favier, M.H. Abbaspour-Fard, M. Kremmer, A.O. Raji, Shape representation of axi-symmetrical, non-spherical particles in discrete element simulation using multi-element model particles, *Eng. Comput.* 16 (1999) 467–480.
- [107] G. Lu, J.R. Third, C.R. Müller, Critical assessment of two approaches for evaluating contacts between super-quadratic shaped particles in DEM simulations, *Chem. Eng. Sci.* 78 (2012) 226–235.
- [108] J.M. Ting, A robust algorithm for ellipse-based discrete element modelling of granular material, *Comput. Geotech.* 13 (1992) 175–186.
- [109] G.T. Houslby, Potential particles: a method for modelling non-circular particles in DEM, *Comput. Geotech.* 36 (2009) 953–959.
- [110] J.R. Williams, R. O'Connor, A linear complexity intersection algorithm for discrete element simulation of arbitrary geometries, *Eng. Comput.* 12 (1995) 185–201.
- [111] X. Jia, R.A. Williams, A packing algorithm for particles of arbitrary shapes, *Powder Technol.* 120 (2001) 175–186.
- [112] X. Jia, N. Gopinathan, R.A. Williams, Modeling complex packing structures and their thermal properties, *Adv. Powder Technol.* 13 (2002) 55–71.
- [113] X. Jia, M. Gan, R.A. Williams, D. Rhodes, Validation of a digital packing algorithm in predicting powder packing densities, *Powder Technol.* 174 (2007) 10–13.
- [114] J.S. Ketchel, P.M. Larochelle, Collision detection of cylindrical rigid bodies using line geometry, ASME 2005 International Design Engineering Technical Conferences and Computers and Information in Engineering Conference, Am. Soc. Mech. Eng. (2005) 811–825.
- [115] F. Geng, Z.L. Yuan, Y.M. Yan, D.S. Luo, H.S. Wang, B. Li, D.Y. Xu, Numerical simulation on mixing kinetics of slender particles in a rotary dryer, *Powder Technol.* 193 (2009) 50–58.
- [116] M. Kodam, R. Bharadwaj, J. Curtis, B. Hancock, C. Wassgren, Cylindrical object contact detection for use in discrete element method simulations. Part I-Contact detection algorithms, *Chem. Eng. Sci.* 65 (2010) 5852–5862.
- [117] M. Kodam, R. Bharadwaj, J. Curtis, B. Hancock, C. Wassgren, Cylindrical object contact detection for use in discrete element method simulations, Part II-Experimental validation, *Chem. Eng. Sci.* 65 (2010) 5863–5871.
- [118] Y. Guo, C. Wassgren, W. Ketterhagen, B. Hancock, B. James, J. Curtis, A numerical study of granular shear flows of rod-like particles using the discrete element method, *J. Fluid Mech.* 713 (2012) 1–26.
- [119] R.C. Hidalgo, D. Kadau, T. Kanzaki, H.J. Herrmann, Granular packings of cohesive elongated particles, *Granul. Matter* 14 (2012) 191–196.
- [120] Y. Guo, C. Wassgren, W. Ketterhagen, B. Hancock, J. Curtis, Some computational considerations associated with discrete element modeling of cylindrical particles, *Powder Technol.* 228 (2012) 193–198.
- [121] G.D. Wehinger, T. Eppinger, M. Kraume, Evaluating catalytic fixed-bed reactors for dry reforming of methane with detailed CFD, *Chem. Eng. Tech.* 87 (2015) 734–745.
- [122] J. Li, P.A. Langston, C. Webb, T. Dyakowski, Flow of spheroid-disc particles in rectangular hoppers - a DEM and experimental comparison in 3D, *Chem. Eng. Sci.* 59 (2004) 5917–5929.
- [123] P.A. Langston, M.A. Al-Awamleh, F.Y. Fraige, B.N. Asmar, Distinct element modelling of non-spherical frictionless particle flow, *Chem. Eng. Sci.* 59 (2004) 425–435.
- [124] Y. Song, R. Turton, F. Kayihan, Contact detection algorithms for DEM simulations of tablet-shaped particles, *Powder Technol.* 161 (2006) 32–40.
- [125] M. Kodam, J. Curtis, B. Hancock, C. Wassgren, Discrete element method modeling of bi-convex pharmaceutical tablets: Contact detection algorithms and validation, *Chem. Eng. Sci.* 69 (2012) 587–601.
- [126] G.T. Nolan, P.E. Kavanagh, Random packing of non-spherical particles, *Powder Technol.* 84 (1995) 199–205.

- [127] T. Pöschel, V. Buchholtz, Static friction phenomena in granular materials: Coulomb law versus particle geometry, *Phys. Rev. Lett.* 70 (1993) 3963–3966.
- [128] V. Buchholtz, T. Pöschel, Numerical investigations of the evolution of sandpiles, *Phys. A Stat. Mech. Appl.* 202 (1994) 390–401.
- [129] Y. Maeno, Numerical investigation of surface level instability due to a tube in a vibrating bed of powder, *Phys. A Stat. Mech. Appl.* 232 (1996) 27–39.
- [130] A.V. Potapov, C.S. Campbell, M.A. Hopkins, A two-dimensional dynamic solution of solid fracture. Part I: Description of model, *Int. J. Mod. Phys. C* 6 (1995) 371–398.
- [131] A.V. Potapov, C.S. Campbell, M.A. Hopkins, A two-dimensional dynamic solution of solid fracture. Part II: Examples, *Int. J. Mod. Phys. C* 6 (1995) 399–425.
- [132] M.P. Allen, D. Frenkel, J. Talbot, Molecular dynamics simulation using hard particles, *Comput. Phys. Rep.* 9 (1989) 301–353.
- [133] C. Tutz, U. Exner, A. Preh, B. Grasemann, The influence of particle orientation on the loading condition of pebbles in fluvial gravel, *Granul. Matter* 14 (2012) 639–649.
- [134] C.J. Coetzee, D.N.J. Els, Calibration of discrete element parameters and the modeling of silo discharge and bucket filling, *Comput. Electron. Agric.* 65 (2009) 198–212.
- [135] W. Zhong, Y. Zhang, B. Jin, M. Zhang, Discrete element method simulation of cylinder-shaped particle flow in a gas-solid fluidized bed, *Chem. Eng. Technol.* 32 (2009) 386–391.
- [136] H. Tao, B. Jin, W. Zhong, X. Wang, B. Ren, Y. Zhang, R. Xiao, Discrete element method modeling of non-spherical granular flow in rectangular hopper, *Chem. Eng. Process.* 49 (2010) 151–158.
- [137] C. González-Montellano, F. Ayuga, J.Y. Ooi, Discrete element modelling of grain flow in a planar silo: influence of simulation parameters, *Granul. Matter* 13 (2011) 149–158.
- [138] Y. Yu, H. Fu, J. Yu, DEM-based simulation of the corn threshing process, *Adv. Powder Technol.* 26 (2015) 1400–1409.
- [139] D. Markauskas, Á. Ramírez-Gómez, R. Kačianauskas, E. Zdancvičius, Maize grain shape approaches for DEM modelling, *Comput. Electron. Agric.* 118 (2015) 247–258.
- [140] Z. Ma, Y. Li, L. Xu, Discrete-element method simulation of agricultural particles' motion in variable-amplitude screen box, *Comput. Electron. Agric.* 118 (2015) 92–99.
- [141] Z. Grof, M. Kohout, F. Štěpánek, Multi-scale simulation of needle-shaped particle breakage under uniaxial compaction, *Chem. Eng. Sci.* 62 (2007) 1418–1429.
- [142] M. Akashi, M. Hiroshi, A. Shimosaka, Y. Shirakawa, J. Hidaka, S. Nomura, Estimation of bulk density distribution in particle charging process using discrete element method considering particle shape, *ISIJ Int.* 48 (2008) 1500–1506.
- [143] J.F. Ferrellec, G.R. McDowell, A simple method to create complex particle shapes for DEM, *Geomech. Geoeng.* 3 (2008) 211–216.
- [144] D. Markauskas, R. Kačianauskas, A. Džiugys, R. Navakas, Investigation of adequacy of multi-sphere approximation of elliptical particles for DEM simulations, *Granul. Matter* 12 (2010) 107–123.
- [145] A.P. Grima, P.W. Wypych, Investigation into calibration of discrete element model parameters for scale-up and validation of particle-structure interactions under impact conditions, *Powder Technol.* 212 (2011) 198–209.
- [146] S. Amberger, M. Friedl, C. Goniva, S. Pirker, C. Kloss, Approximation of objects by spheres for multisphere simulations in DEM, *ECOMMAS*, Vienna Austria, 2012.
- [147] H. Li, G.R. McDowell, I.S. Lowndes, A laboratory investigation and discrete element modeling of rock flow in a chute, *Powder Technol.* 229 (2012) 199–205.
- [148] T. Liudas, K. Rimantas, N. Arnoldas, Z. Daiva, Comparison study of spherical and multi-spherical particles under cyclic uniaxial compression, *J. Civ. Eng. Manag.* 18 (2012) 537–545.
- [149] C. González-Montellano, E. Gallego, Á. Ramírez-Gómez, F. Ayuga, Three dimensional discrete element models for simulating the filling and emptying of silos: Analysis of numerical results, *Comput. Chem. Eng.* 40 (2012) 22–32.
- [150] H. Tao, W. Zhong, B. Jin, Comparison of construction method for DEM simulation of ellipsoidal particles, *Chin. J. Chem. Eng.* 21 (2013) 800–807.
- [151] X.L. Deng, R.N. Davé, Dynamic simulation of particle packing influenced by size, aspect ratio and surface energy, *Granul. Matter* 15 (2013) 401–415.
- [152] H. Krugel-Emden, F. Elskamp, Modeling of screening processes with the discrete element method involving non-spherical particles, *Chem. Eng. Technol.* 37 (2013) 847–856.
- [153] Y.C. Chung, H.H. Liao, S.S. Hsiao, Convection behavior of non-spherical particles in a vibrating bed: Discrete element modeling and experimental validation, *Powder Technol.* 237 (2013) 53–66.
- [154] H. Tao, W. Zhong, B. Jin, Flow behavior of non-spherical particle flowing in hopper, *Front. Energy* 8 (2014) 315–321.
- [155] S. Akhshik, M. Behzad, M. Rajabi, CFD-DEM Model for simulation of non-spherical particles in hole cleaning process, *Part. Sci. Technol.* 33 (2015) 472–481.
- [156] B. Majidi, J. Melo, M. Fafard, D. Ziegler, H. Alamdari, Packing density of irregular shape particles: DEM simulations applied to anode-grade coke aggregates, *Adv. Powder Technol.* 26 (2015) 1256–1262.
- [157] R. Maiione, S. Kiesgen De Richter, G. Maувиель, G. Wild, DEM investigation of granular flow and binary mixture segregation in a rotating tumbler: Influence of particle shape and internal baffles, *Powder Technol.* 286 (2015) 732–739.
- [158] J. Ferrellec, G.R. McDowell, A method to model realistic particle shape and inertia in DEM, *Granul. Matter* 12 (2010) 459–467.
- [159] J. Ferrellec, G. McDowell, Modelling realistic shape and particle inertia in DEM, *Geotechnique* 60 (2010) 227–232.
- [160] E.J.R. Parteli, DEM simulation of particles of complex shapes using the multisphere method: application for additive manufacturing, *AIP Conf. Proc.* 1542 (2013) 185–188.
- [161] E.J.R. Parteli, Using LIGGGHTS for performing DEM simulations of particles of complex shapes with the multisphere method, In: *DEM6–6th International Conference on Discrete Element Methods and Related Techniques*, Golden, USA, 2013.
- [162] L. Wang, J. Park, Y. Fu, Representation of real particles for DEM simulation using X-ray tomography, *Constr. Build. Mater.* 21 (2007) 338–346.
- [163] T. Matsushima, H. Saomoto, M. Matsumoto, K. Toda, Y. Yamada, Discrete element simulation of an assembly of irregular-shaped grains: quantitative comparison with experiments, *16th ASCE Engineering Mechanics Conference*, Springer-Verlag, Heidelberg 2013, p. 44.
- [164] H. Krugel-Emden, S. Rickelt, S. Wirtz, V. Scherer, A study on the validity of the multi-sphere Discrete Element Method, *Powder Technol.* 188 (2008) 153–165.
- [165] M. Price, V. Murariu, G. Morrison, Sphere clump generation and trajectory comparison for real particles, *Proceeding of Discrete Element Modelling*, 2007.
- [166] C. Li, W. Xu, Q. Meng, Multi-sphere approximation of real particles for DEM simulation based on a modified greedy heuristic algorithm, *Powder Technol.* 286 (2015) 478–487.
- [167] J. Quist, C.M. Evertsson, Cone crusher modelling and simulation using DEM, *Miner. Eng.* 85 (2016) 92–105.
- [168] L. Gao, Q. Luo, Y. Xu, G. Jing, H. Jiang, Discrete element method of improved performance of railway ballast bed using elastic sleeper, *J. Cent. South Univ.* 22 (2015) 3223–3231.
- [169] Y. Guo, C. Wassgren, B. Hancock, W. Ketterhagen, J. Curtis, Computational study of granular shear flows of dry flexible fibres using the discrete element method, *J. Fluid Mech.* 775 (2015) 24–52.
- [170] A. Reinhold, S. Schorsch, M. Mazzotti, H. Briesen, Modeling and measurement of abraded particles, *Powder Technol.* 271 (2015) 134–140.
- [171] F.Y. Fraige, P.A. Langston, A.J. Matchett, J. Dodds, Vibration induced flow in hoppers: DEM 2D polygon model, *Particuology* 6 (2008) 455–466.
- [172] J. Wang, H.S. Yu, P. Langston, F. Fraige, Particle shape effects in discrete element modelling of cohesive angular particles, *Granul. Matter* 13 (2011) 1–12.
- [173] M. Boton, E. Azéma, N. Estrada, F. Radjai, A. Lizcano, Quasistatic rheology and microstructural description of sheared granular materials composed of platy particles, *Phys. Rev. E* 87 (2013) 32206.
- [174] D. Höhner, S. Wirtz, V. Scherer, A study on the influence of particle shape and shape approximation on particle mechanics in a rotating drum using the discrete element method, *Powder Technol.* 253 (2014) 256–265.
- [175] E. Crammond, Squaring the circle: arbitrarily shaped particle modeling in distinct element analysis, *M. Eng. Project report*, Dept. of Engineering Science, Oxford University, 2007.
- [176] C.W. Boon, G.T. Housby, S. Utili, A new algorithm for contact detection between convex polygonal and polyhedral particles in the discrete element method, *Comput. Geotech.* 44 (2012) 73–82.
- [177] C.W. Boon, G.T. Housby, S. Utili, A new contact detection algorithm for three-dimensional non-spherical particles, *Powder Technol.* 248 (2013) 94–102.
- [178] L. Pournin, M. Weber, M. Tsukahara, J.A. Ferrellec, M. Ramaoli, T.M. Liebling, Three-dimensional distinct element simulation of spherocylinder crystallization, *Granul. Matter* 7 (2005) 119–126.
- [179] L. Pournin, A generalization of Distinct Element Method to tridimensional particles with complex shapes, *General Information*, 2, 2005, pp. 1375–1478.
- [180] F. Alonso-Marroquín, Y. Wang, An efficient algorithm for granular dynamics simulations with complex-shaped objects, *Granul. Matter* 11 (2009) 317–329.
- [181] F. Alonso-Marroquín, Á. Ramírez-Gómez, C. González-Montellano, N. Balaam, D.A.H. Hanaor, E.A. Flores-Johnson, Y. Gan, S. Chen, L. Shen, Experimental and numerical determination of mechanical properties of polygonal wood particles and their flow analysis in silos, *Granul. Matter* 15 (2013) 811–826.
- [182] H. Li, T. Yu, L. Zhu, W. Wang, Modeling and simulation of grinding wheel by discrete element method and experimental validation, *Int. J. Adv. Manuf. Technol.* 81 (2015) 1921–1938.
- [183] Z.Y. Zhou, R.P. Zou, D. Pinson, A.B. Yu, Angle of repose and stress distribution of sandpiles formed with ellipsoidal particles, *Granul. Matter* 16 (2014) 695–709.
- [184] A. Rahman, F.H. Stillinger, Molecular dynamics study of liquid water, *J. Chem. Phys.* 55 (1971) 3336–3359.
- [185] D.J. Evans, S. Murad, Singularity free algorithm for molecular dynamics simulation of rigid polyatomics, in: C. G. D. Frenkel, R. McDonald (Eds.), *Simulation of liquids and solids*, North-Holland 1977, pp. 367–371.
- [186] D. Fincham, M.D. Heyes, Recent advances in molecular-dynamics Computer simulation, in: M.W. Evans (Ed.), *Dynamic processes in condensed matter-advances in chemical physics*, John Wiley & Sons 1985, pp. 493–575.
- [187] H. Goldstein, *Classical Mechanics*, Addison-Wesley Publishing Company, 1980.
- [188] I.I. Kosenko, Integration of the equations of a rotational motion of a rigid body in quaternion algebra, The Euler case, *J. Appl. Math. Mech.* 2 (1998) 193–200.
- [189] J. Barojas, D. Levesque, B. Quentrec, Simulation of diatomic homonuclear liquids, *Phys. Rev. A* 7 (1973) 1092.
- [190] G. Ciccotti, M. Ferrario, J.P. Ryckaert, *Simulation of liquids and solids*, North-Holland, 1987.
- [191] T. Pöschel, T. Schwager, *Computational Granular Dynamics*, Springer, Berlin, 2005.
- [192] A. Munjiza, J.P. Latham, N.W.M. John, 3D dynamics of discrete element systems comprising irregular discrete elements – integration solution for finite rotations in 3D, *Int. J. Numer. Methods Eng.* 56 (2003) 35–55.
- [193] J.C. Simo, K.K. Wong, Unconditionally stable algorithms for rigid body dynamics that exactly preserve energy and momentum, *Int. J. Numer. Methods Eng.* 31 (1991) 19–52.
- [194] H. Krugel-Emden, E. Simsek, S. Rickelt, S. Wirtz, V. Scherer, Review and extension of normal force models for the Discrete Element Method, *Powder Technol.* 171 (2007) 157–173.
- [195] Q.J. Zheng, Z.Y. Zhou, A.B. Yu, Contact forces between viscoelastic ellipsoidal particles, *Powder Technol.* 248 (2013) 25–33.
- [196] G.A. Kohring, Studies of diffusional mixing in ratating drums via computer simulations, *J. Phys. I France* 5 (1995) 1551–1561.
- [197] G.A. Kohring, in: J.A. Désidéri (Ed.), *Dynamical simulations of granular flows on multi-processor computer*, *Computational Methods in Applied Sciences*, 96, 1997, pp. 190–196.
- [198] N.V. Brilliantov, F. Spahn, F.M. Hertzsch, The collision of particles in granular systems, *Physica A* 231 (1996) 417–424.
- [199] G. Kuwabara, K. Kono, Restitution coefficient in a collision between two spheres, *Jpn. J. Appl. Phys.* 26 (1987) 1230–1233.

- [200] H. Krugel-Emden, S. Wirtz, V. Scherer, An analytical solution of different configurations of the linear viscoelastic normal and frictional-elastic tangential contact model, *Chem. Eng. Sci.* 62 (2007) 6914–6926.
- [201] M. Kodam, R. Bharadwaj, J. Curtis, B. Hancock, C. Wassgren, Force model considerations for glued-sphere discrete element method simulations, *Chem. Eng. Sci.* 64 (2009) 3466–3475.
- [202] Y.T. Feng, D.R.J. Owen, A 2D polygon/polygon contact model: algorithmic aspects, *Eng. Comput.* 21 (2004) 265–277.
- [203] K.L. Johnson, *Contact mechanics*, Cambridge University Press, New York, 1985.
- [204] Y. Tsuji, T. Kawaguchi, T. Tanaka, Discrete particle simulation of two-dimensional fluidized bed, *Powder Technol.* 77 (1993) 79–87.
- [205] H.H. Hu, Direct simulation of flows of solid-liquid mixtures, *Int. J. Multiphase Flow* 22 (1996) 335–352.
- [206] B.K. Cook, D.R. Noble, J.R. Williams, A direct simulation method for particle-fluid systems, *Eng. Comput.* 21 (2004) 151–168.
- [207] W. Ge, J.H. Li, Macro-scale pseudo-particle modelling for particle-fluid systems, *Chin. Sci. Bull.* 46 (2001) 1503–1507.
- [208] W. Ge, J.H. Li, Macro-scale phenomena reproduced in microscopic systems-pseudo-particle modelling of fluidization, *Chem. Eng. Sci.* 58 (2003) 1565–1585.
- [209] W. Ge, J.H. Li, Simulation of particle-fluid systems with macro-scale pseudo-particle modelling, *Powder Technol.* 137 (2003) 99–108.
- [210] T.W. Pan, D.D. Joseph, R. Bai, Fluidization of 1204 spheres: simulation and experiment, *J. Fluid Mech.* 451 (2002) 169–191.
- [211] H. Zhou, G. Flamant, D. Gauthier, J. Lu, Numerical simulation of the turbulent gas-particle flow in a fluidized bed by an LES-DPM model, *Chem. Eng. Res. Des.* 82 (2004) 918–926.
- [212] H.S. Zhou, G. Flamant, D. Gauthier, DEM-LES of coal combustion in a bubbling fluidized bed. Part I, gas-particle turbulent flow structure, *Chem. Eng. Sci.* 59 (2004) 4193–4203.
- [213] H.S. Zhou, G. Flamant, D. Gauthier, DEM-LES simulation of coal combustion in a bubbling fluidized bed. Part II, coal combustion at particle level, *Chem. Eng. Sci.* 59 (2004) 4205–4215.
- [214] T. Oschmann, J. Hold, H. Krugel-Emden, Numerical investigation of mixing and orientation of non-spherical particles in a model type fluidized bed, *Powder Technol.* 258 (2014) 304–323.
- [215] V. Singh, L.O. Simon, Predicting pressure drop in pneumatic conveying using the discrete element modeling approach, *Seventh International Conference on CFD in the Minerals and Process Industries*, CSIRO, Melbourne, Australia, 2009.
- [216] R. Clift, J.R. Grace, M.E. Weber, *Bubbles, drops, and particles*, Academic Press, New York, 2005.
- [217] A.R. Khan, J.F. Richardson, Fluid-particle interactions and flow characteristics of fluidized beds and settling suspensions of spherical particles, *Chem. Eng. Commun.* 78 (1989) 111–130.
- [218] M. Hartman, J.G. Yates, Free-fall of solid particles through fluids, *Collect. Czechoslov. Chem. Commun.* 58 (1993) 961–982.
- [219] B.D. Bowen, J.H. Masliyah, Drag force on isolated axisymmetric particles in Stokes flow, *Can. J. Chem. Eng.* 51 (1973) 8–15.
- [220] J. Militzer, J.M. Kan, F. Hamdullahpur, P.R. Amyotte, A.M. Al Taweel, Drag coefficient for axisymmetric flow around individual spheroidal particles, *Powder Technol.* 57 (1989) 193–195.
- [221] A. Tripathi, R.P. Chhabra, T. Sundararajan, Power law fluid flow over spheroidal particles, *Ind. Eng. Chem. Res.* 32 (1994) 403–410.
- [222] E.S. Pettyjohn, E.B. Christiansen, Effect of particle shape on free-settling rates of isometric particles, *Chem. Eng. Prog.* 44 (1948) 157–172.
- [223] A. Haider, O. Levenspiel, Drag coefficient and terminal velocity of spherical and nonspherical particles, *Powder Technol.* 58 (1989) 63–70.
- [224] D. Rodrigue, R.P. Chhabra, K.D. De, Drag on non-spherical particles in non-newtonian fluids, *Can. J. Chem. Eng.* 72 (1994) 588–593.
- [225] G.V. Madhav, R.P. Chhabra, Drag on non-spherical particles in viscous fluids, *Int. J. Miner. Process.* 43 (1995) 15–29.
- [226] N. Agarwal, R.P. Chhabra, Settling velocity of cubes in Newtonian and power law liquids, *Powder Technol.* 178 (2007) 17–21.
- [227] D. Laskovski, P. Stevenson, K.P. Galvin, Lift and drag forces on an isolated cubic particle in pipe flow, *Chem. Eng. Res. Des.* 87 (2009) 1573–1581.
- [228] Y. Chen, J.R. Third, C.R. Müller, A drag force correlation for approximately cubic particles constructed from identical spheres, *Chem. Eng. Sci.* 123 (2015) 146–154.
- [229] E.K. Marchildon, A. Clamen, W.H. Gauvin, Drag and oscillatory motion of freely falling cylindrical particles, *Can. J. Chem. Eng.* 42 (1964) 178–182.
- [230] B. Huner, R.G. Hussey, Cylinder drag at low Reynolds number, *Phys. Fluids* 20 (1977) 1211–1218 (1958–1988).
- [231] T.J. Uli, R.G. Hussey, R.P. Roger, Stokes drag on a cylinder in axial motion, *Phys. Fluids* (1958–1988) 27 (1984) 787–795.
- [232] A. Unnikrishnan, R.P. Chhabra, An experimental study of motion of cylinders in Newtonian fluids: wall effects and drag coefficient, *Can. J. Chem. Eng.* 69 (1991) 729–735.
- [233] N. Phan-Thien, H.S. Dou, Viscoelastic flow past a cylinder: drag coefficient, *Comput. Methods Appl. Mech. Eng.* 180 (1999) 243–266.
- [234] R.P. Chhabra, K. Rami, P.H.T. Uhlherr, Drag on cylinders in shear thinning viscoelastic liquids, *Chem. Eng. Sci.* 56 (2001) 2221–2227.
- [235] J. Hsu, C. Shie, S. Tseng, Sedimentation of a cylindrical particle in a Carreau fluid, *J. Colloid Interface Sci.* 286 (2005) 392–399.
- [236] J. Gabitto, C. Tsouris, Drag coefficient and settling velocity for particles of cylindrical shape, *Powder Technol.* 183 (2008) 314–322.
- [237] A. Vakil, S.I. Green, Drag and lift coefficients of inclined finite circular cylinders at moderate Reynolds numbers, *Comput. Fluids* 38 (2009) 1771–1781.
- [238] L. Jossic, A. Magnin, Drag of an isolated cylinder and interactions between two cylinders in yield stress fluids, *J. Non-Newtonian Fluid Mech.* 164 (2009) 9–16.
- [239] B. Ren, W. Zhong, B. Jin, Y. Lu, X. Chen, R. Xiao, Study on the drag of a cylinder-shaped particle in steady upward gas flow, *Ind. Eng. Chem. Res.* 50 (2011) 7593–7600.
- [240] W.W. Willmarth, N.E. Hawk, R.L. Harvey, Steady and unsteady motions and wakes of freely falling disks, *Phys. Fluids* 7 (1964) 197–208.
- [241] R. Shail, D.J. Norton, On the slow broadside motion of a thin disc along the axis of a fluid-filled circular duct, *Mathematical Proceedings of the Cambridge Philosophical Society*, 65, Cambridge University Press 1969, pp. 793–802.
- [242] P. Davis, Application of optical chaos to temporal pattern search in a nonlinear optical resonator, *Jpn. J. Appl. Phys.* 29 (1990) L1238–L1240.
- [243] P. Rajitha, R.P. Chhabra, N.E. Sabiri, J. Comiti, Drag on non-spherical particles in power law non-Newtonian media, *Int. J. Miner. Process.* 78 (2006) 110–121.
- [244] J. Wang, H. Qi, C. You, Experimental study of sedimentation characteristics of spheroidal particles, *Particuology* 7 (2009) 264–268.
- [245] J.F. Heiss, J. Coull, The effect of orientation and shape on the settling velocity of non-isometric particles in a viscous medium, *Chem. Eng. Prog.* 48 (1952) 133–140.
- [246] K. Jayaweera, B.J. Mason, The behavior of freely falling cylinders and cones in a viscous fluid, *J. Fluid Mech.* 22 (1965) 709–720.
- [247] R.P. Roger, R.G. Hussey, Stokes drag on a flat annular ring, *Phys. Fluids* 25 (1982) 915–922.
- [248] T.L. Thompson, N.N. Clark, A holistic approach to particle drag prediction, *Powder Technol.* 67 (1991) 57–66.
- [249] G.H. Ganser, A rational approach to drag prediction of spherical and nonspherical particles, *Powder Technol.* 77 (1993) 143–152.
- [250] S.F. Chien, Settling velocity of irregularly shaped particles, *SPE Drill. Compleat.* 9 (1994) 281–289.
- [251] M. Hartman, O. Trnka, K. Svoboda, V. Veselý, Influence of particle shape on the drag coefficient for isometric particles, *Collect. Czechoslov. Chem. Commun.* 59 (1994) 2583–2594.
- [252] G. Venu Madhav, R.P. Chhabra, Settling velocities of non-spherical particles in non-Newtonian polymer solutions, *Powder Technol.* 78 (1994) 77–83.
- [253] H. Wadell, Sphericity and roundness of rock particles, *J. Geol.* 41 (1933) 310–331.
- [254] E.B. Christiansen, D.H. Barker, Effect of shape and density on free settling of particles at high Reynolds number, *AIChE J.* 11 (1965) 145–151.
- [255] R.P. Chhabra, L. Agarwal, N.K. Sinha, Drag on non-spherical particles: an evaluation of available methods, *Powder Technol.* 101 (1999) 288–295.
- [256] J.L. Isaacs, G. Thodos, The Free-settling of solid cylindrical particle in the Turbulent Regime, *Can. J. Chem. Eng.* 45 (1967) 150–155.
- [257] S. Ergun, Fluid flow through packed columns, *Chem. Eng. Prog.* 48 (1952).
- [258] C.Y. Wen, Y.H. Yu, A generalized method for predicting the minimum fluidization velocity, *AIChE J.* 12 (1966) 610–612.
- [259] J. Happel, N. Epstein, Cubical assemblages of uniform spheres, *Ind. Eng. Chem.* 46 (1954) 1187–1194.
- [260] H.D. Stenzing, Fluid drag on clouds consisting of solid particles enclosed in a pipe, *Pneumotransport I* (BHRA) 1971, pp. 6–8.
- [261] Y. Tsuji, Y. Morikawa, LDV measurements of an air-solid two-phase flow in a horizontal pipe, *J. Fluid Mech.* 120 (1982) 385–409.
- [262] J.F. Richardson, W.N. Zaki, The sedimentation of a suspension of uniform spheres under conditions of viscous flow, *Chem. Eng. Sci.* 3 (1954) 65–73.
- [263] J.F. Richardson, Incipient fluidization and particulate systems, *Fluidization* 1971, pp. 27–29.
- [264] R. Mabrouk, J. Chaouki, C. Guy, Effective drag coefficient investigation in the acceleration zone of an upward gas-solid flow, *Chem. Eng. Sci.* 62 (2007) 318–327.
- [265] R. Di Felice, The Voidage function for fluid-particle interaction systems, *Int. J. Multiphase Flow* 20 (1994) 153–159.
- [266] D.L. Koch, R.J. Hill, Inertial effects in suspension and porous-media flows, *Annu. Rev. Fluid Mech.* 33 (2001) 619–647.
- [267] R. Beetstra, M.A. van der Hoef, J.A.M. Kuipers, Drag force of intermediate Reynolds number flow past mono- and bidisperse arrays of spheres, *AIChE J.* 53 (2007) 489–501.
- [268] D. Nemeč, J. Levec, Flow through packed bed reactor: 1. single-phase flow, *Chem. Eng. Sci.* 60 (2005) 6947–6959.
- [269] E. Ozahi, M.Y. Gundogdu, M.Ö. Carpinlioglu, A modification on Ergun's correlation for use in cylindrical packed beds with non-spherical particles, *Adv. Powder Technol.* 19 (2008) 369–381.
- [270] J. Wang, H. Qi, J. Zhu, Experimental study of settling and drag on cuboids with square base, *Particuology* 9 (2011) 298–305.
- [271] A. Höller, M. Sommerfeld, New simple correlation formula for the drag coefficient of non-spherical particles, *Powder Technol.* 184 (2008) 361–365.
- [272] D. Leith, Drag on nonspherical objects, *Aerosol Sci. Technol.* 6 (1987) 153.
- [273] P.K. Swamee, C.S.P. Ojha, Drag coefficient and fall velocity of nonspherical particles, *J. Hydraul. Eng.* 117 (1991) 660–667.
- [274] S. Tran-Cong, M. Gay, E.E. Michaelides, Drag coefficients of irregularly shaped particles, *Powder Technol.* 139 (2004) 21–32.
- [275] F. Dioguardi, D. Mele, A new shape dependent drag correlation formula for non-spherical rough particles: Experiments and results, *Powder Technol.* 277 (2015) 222–230.
- [276] J.F. Hoerner, fluid-dynamics drag, *Hoerner Fluid Dynamics*, 1965 (published by the author).
- [277] M. Zastawny, G. Mallouppas, F. Zhao, B. van Wachem, Derivation of drag and lift force and torque coefficients for non-spherical particles in flows, *Int. J. Multiphase Flow* 101 (2012) 288–295.
- [278] H. Zhang, Y. Tan, S. Shu, X. Niu, F.X. Trias, D. Yang, H. Li, Y. Sheng, Numerical investigation on the role of discrete element method in combined LBM-IBM-DEM modeling, *Comput. Fluids* 94 (2014) 37–48.
- [279] H. Zhang, F.X. Trias, A. Oliva, D. Yang, Y. Tan, Y. Sheng, PIBM: Particulate immersed boundary method for fluid-particle interaction problems, *Powder Technol.* 272 (2015) 1–13.
- [280] M. Couturier, B. Doucette, D. Stevens, S. Poolpol, V. Razbin, Temperature, gas concentration and solid mass flux profiles within a large circulating fluidized bed combustor, *11th International Conference on FBC, ASME 1991*, pp. 21–24.

- [281] A. Ocampo, E. Arenas, F. Chejne, J. Espinel, C. Londono, J. Aguirre, J.D. Perez, An experimental study on gasification of Colombian coal in fluidised bed, *Fuel* 82 (2003) 161–164.
- [282] A.J. Minchener, Coal gasification for advanced power generation, *Fuel* 84 (2005) 2222–2235.
- [283] K. Dewettinck, A. Huyghebaert, Fluidized bed coating in food technology, *Trends Food Sci. Technol.* 10 (1999) 163–168.
- [284] K. Jono, H. Ichikawa, M. Miyamoto, Y. Fukumori, A review of particulate design for pharmaceutical powders and their production by spouted bed coating, *Powder Technol.* 113 (2000) 269–277.
- [285] X.F. Dong, A.B. Yu, J.I. Yagi, P. Zulli, Modelling of multiphase flow in a blast furnace: Recent developments and future work, *ISIJ Int.* 47 (2007) 1553–1570.
- [286] H. Zhang, F.X. Trias, A. Gorobets, A. Oliva, D. Yang, Y. Tan, Y. Sheng, Effect of collisions on the particle behavior in a turbulent square duct flow, *Powder Technol.* 269 (2015) 320–336.
- [287] J. Yao, M. Fairweather, Particle deposition in turbulent duct flows, *Chem. Eng. Sci.* 84 (2012) 781–800.
- [288] J.F.W. Adams, M. Fairweather, J. Yao, Modelling and simulation of particle re-suspension in a turbulent square duct flow, *Comput. Chem. Eng.* 35 (2011) 893–900.
- [289] J. Feng, H.H. Hu, D.D. Joseph, Direct simulation of initial value problems for the motion of solid bodies in a Newtonian fluid Part 1. Sedimentation, *J. Fluid Mech.* 261 (1994) 95–134.
- [290] J. Feng, H.H. Hu, D.D. Joseph, Direct simulation of initial value problems for the motion of solid bodies in a Newtonian fluid. Part 2. Couette and Poiseuille flows, *J. Fluid Mech.* 277 (1994) 271–301.
- [291] G. Tryggvason, B. Bunner, A. Esmaeli, D. Juric, A front-tracking method for the computations of multiphase flow, *J. Comput. Phys.* 169 (2001) 708–759.
- [292] S.R. Idelsohn, E. Oñate, F.D. Pin, The particle finite element method: a powerful tool to solve incompressible flows with free-surfaces and breaking waves, *Int. J. Numer. Methods Eng.* 61 (2004) 964–989.
- [293] A.J. Ladd, Numerical simulations of particulate suspensions via a discretized Boltzmann equation. Part 1. Theoretical foundation, *J. Fluid Mech.* 271 (1994) 285–309.
- [294] A.J. Ladd, Numerical simulations of particulate suspensions via a discretized Boltzmann equation. Part 2. Numerical results, *J. Fluid Mech.* 271 (1994) 311–339.
- [295] M.P. Allen, D.J. Tildesley, Computer simulation of liquids, Oxford Science Publication, 1990.
- [296] H.H. Hu, D.D. Joseph, M.J. Crochet, Direct simulation of fluid particle motions, *Theor. Comput. Fluid Dyn.* 3 (1992) 285–306.
- [297] W. Zhong, Y. Xiong, Z. Yuan, M. Zhang, DEM simulation of gas-solid flow behaviors in spout-fluid bed, *Chem. Eng. Sci.* 61 (2006) 1571–1584.
- [298] F.X. Trias, O. Lehmkuhl, A. Oliva, C.D. Pérez-Segarra, R.W.C.P. Verstappen, Symmetry-preserving discretization of Navier-Stokes equations on collocated unstructured grids, *J. Comput. Phys.* 258 (2014) 246–267.
- [299] B.P.B. Hoomans, J.A.M. Kuipers, W.J. Briels, W.P.M. Van Swaaij, Discrete particle simulation of bubble and slug formation in a two-dimensional gas-fluidised bed: a hard-sphere approach, *Chem. Eng. Sci.* 51 (1995) 99–118.
- [300] B.H. Xu, Y.Q. Feng, A.B. Yu, S.J. Chew, P. Zulli, A numerical and experimental study of gas-solid flow in a fluid-bed reactor, *Powder Handl. Process.* 13 (2001) 71–76.
- [301] K.D. Kafui, C. Thornton, M.J. Adams, Discrete particle-continuum fluid modelling of gas-solid fluidised beds, *Chem. Eng. Sci.* 57 (2002) 2395–2410.
- [302] R.W. Macomack, Numerical solution of the interaction of a shock wave with a laminar boundary layer, Proceedings of the Second international Conference on Numerical Methods in Fluid Dynamics, Springer, Berlin Heidelberg 1971, pp. 151–163.
- [303] D.R.J. Owen, C.R. Leonardi, Y.T. Feng, An efficient framework for fluid-structure interaction using the lattice Boltzmann method and immersed moving boundaries, *Int. J. Numer. Methods Eng.* 87 (2011) 66–95.
- [304] Z. Zhou, S. Kuang, K. Chu, A. Yu, Discrete particle simulation of particle-fluid flow: model formulations and their applicability, *J. Fluid Mech.* 661 (2010) 482–510.
- [305] Y.Q. Feng, A.B. Yu, Assessment of model formulations in the discrete particle simulation of gas-solid flow, *Ind. Eng. Chem. Res.* 43 (2004) 8378–8390.
- [306] M. Nitschke, E.H. Knickmeyer, Rotation parameters—a survey of techniques, *J. Surv. Eng.* (2000).
- [307] C.S. Peskin, Numerical analysis of blood flow in the heart, *J. Comput. Phys.* 25 (1977) 220–252.
- [308] Y.H. Qian, D. D'Humieres, P. Lallemand, Lattice BGK Models for Navier-Stokes Equation, *Europhys. Lett.* 17 (1992) 479–484.
- [309] D.R. Noble, J.R. Torczynski, A lattice-Boltzmann method for partially saturated computational cells, *Int. J. Mod. Phys. C* 09 (1998) 1189–1201.
- [310] Z.G. Feng, E.E. Michaelides, The immersed boundary-lattice Boltzmann method for solving fluid-particles interaction problems, *J. Comput. Phys.* 195 (2004) 602–628.
- [311] Z.G. Feng, E.E. Michaelides, Proteus: a direct forcing method in the simulations of particulate flows, *J. Comput. Phys.* 202 (2005) 20–51.
- [312] X. Niu, C. Shu, Y. Chew, Y. Peng, A momentum exchange-based immersed boundary-lattice Boltzmann method for simulating incompressible viscous flows, *Phys. Lett. A* 354 (2006) 173–182.
- [313] Y. Hu, D. Li, S. Shu, X. Niu, Modified momentum exchange method for fluid-particle interactions in the lattice -Boltzmann method, *Phys. Rev. E Stat. Nonlinear Soft Matter Phys.* 91 (2015) 33301.
- [314] K. Luo, Z. Wang, J. Fan, K. Cen, Full-scale solutions to particle-laden flows: Multidirect forcing and immersed boundary method, *Phys. Rev. E Stat. Nonlinear Soft Matter Phys.* 76 (2007) 66709.
- [315] X. García, D. Pavlidis, G.J. Gorman, J.L.M.A. Gomes, M.D. Piggott, E. Aristodemou, J. Mindel, J. Latham, C.C. Pain, H. ApSimon, A two-phase adaptive finite element method for solid-fluid coupling in complex geometries, *Int. J. Numer. Methods Fluids* 66 (2011) 82–96.
- [316] H.H. Hu, N.A. Patankar, M.Y. Zhu, Direct numerical simulations of fluid–solid systems using the arbitrary Lagrangian-Eulerian technique, *J. Comput. Phys.* 169 (2001) 427–462.
- [317] P.Y. Huang, J. Feng, D.D. Joseph, The turning couples on an elliptic particle settling in a vertical channel, *J. Fluid Mech.* 274 (1994) 1–16.
- [318] H.H. Hu, Motion of a circular cylinder in a viscous liquid between parallel plates, *Theor. Comput. Fluid Dyn.* 7 (1995) 441–455.
- [319] J. Feng, P.Y. Huang, D.D. Joseph, Dynamic simulation of the motion of capsules in pipelines, *J. Fluid Mech.* 286 (1995) 201–227.
- [320] R.L. Brown, P.G.W. Hawksley, Packing of regular (spherical) and irregular particles, *Nature* 156 (1945) 421–422.
- [321] H.G. Matutis, Simulation of the pressure distribution under a two-dimensional heap of polygonal particles, *Granul. Matter* 1 (1998) 83–91.
- [322] C. Zhou, J.Y. Ooi, Numerical investigation of progressive development of granular pile with spherical and non-spherical particles, *Mech. Mater.* 41 (2009) 707–714.
- [323] Y. Chung, J.Y. Ooi, A study of influence of gravity on bulk behaviour of particulate solid, *Particuology* 6 (2008) 467–474.
- [324] M. Acevedo, R.C. Hidalgo, I. Zuriguel, D. Maza, I. Pagonabarraga, Influence of the feeding mechanism on deposits of square particles, *Phys. Rev. E* 87 (2013) 12202.
- [325] P. Roul, A. Schinner, K. Kassner, Mechanical properties of non-cohesive polygonal particle aggregates, *Granul. Matter* 13 (2011) 303–317.
- [326] P. Roul, A. Schinner, K. Kassner, Discrete-element computation of averaged tensorial fields in sand piles consisting of polygonal particles, *Geotech. Geol. Eng.* 29 (2011) 597–610.
- [327] J. Zhao, S. Li, P. Lu, L. Meng, T. Li, H. Zhu, Shape influences on the packing density of frustums, *Powder Technol.* 214 (2011) 500–505.
- [328] J.Y. Zhu, Y.Y. Liang, Y.H. Zhou, The effect of the particle aspect ratio on the pressure at the bottom of sandpiles, *Powder Technol.* 234 (2013) 37–45.
- [329] D. Markauskas, R. Kačianauskas, Investigation of rice grain flow by multi-sphere particle model with rolling resistance, *Granul. Matter* 13 (2011) 143–148.
- [330] T. Kanzaki, M. Acevedo, I. Zuriguel, I. Pagonabarraga, D. Maza, R.C. Hidalgo, Stress distribution of faceted particles in a silo after its partial discharge, *Eur. Phys. J. E* 34 (2011) 1–8.
- [331] J.R. Third, D.M. Scott, S.A. Scott, C.R. Muller, Tangential velocity profiles of granular material within horizontal rotating cylinders modelled using the DEM, *Granul. Matter* 12 (2010) 587–595.
- [332] O. Dube, E. Alizadeh, J. Chaouki, F. Bertrand, Dynamics of non-spherical particles in a rotating drum, *Chem. Eng. Sci.* 101 (2013) 486–502.
- [333] G.G. Pereira, S. Pucilowski, K. Liffman, P.W. Cleary, Streak patterns in binary granular media in a rotating drum, *Appl. Math. Model.* 35 (2011) 1638–1646.
- [334] G.G. Pereira, N. Tran, P.W. Cleary, Segregation of combined size and density varying binary granular mixtures in a slowly rotating tumbler, *Granul. Matter* 16 (2014) 711–732.
- [335] C. Pei, C. Wu, M. Adams, Numerical analysis of contact electrification of non-spherical particles in a rotating drum, *Powder Technol.* 285 (2015) 110–122.
- [336] M. Ramaoli, L. Pournin, T.M. Liebling, Vertical ordering of rods under vertical vibration, *Phys. Rev. E* 76 (2007) 21304.
- [337] M.D. Sinnott, P.W. Cleary, R.D. Morrison, Is media shape important for grinding performance in stirred mills? *Miner. Eng.* 24 (2011) 138–151.
- [338] X. Hua, J. Curtis, Y. Guo, B. Hancock, W. Ketterhagen, C. Wassgren, The internal loads, moments, and stresses in rod-like particles in a low-speed, vertical axis mixer, *Chem. Eng. Sci.* 134 (2015) 581–598.
- [339] K. Vollmari, R. Jasevicius, H. Kruggel-Emden, Experimental and numerical study of fluidization and pressure drop of spherical and non-spherical particles in a model scale fluidized bed, *Powder Technol.* 291 (2016) 506–521.
- [340] K. Vollmari, T. Oschmann, S. Wirtz, H. Kruggel-Emden, Pressure drop investigations in packings of arbitrary shaped particles, *Powder Technol.* 271 (2015) 109–124.
- [341] D.O. Njobuenwu, M. Fairweather, Effect of shape on inertial particle dynamics in a channel flow, *Flow Turbul. Combust.* 92 (2014) 83–101.
- [342] D.O. Njobuenwu, M. Fairweather, Simulation of inertial fibre orientation in turbulent flow, *Phys. Fluids* 28 (2016) 063307.
- [343] Y. Feng, C. Kleinstreuer, Analysis of non-spherical particle transport in complex internal shear flows, *Phys. Fluids* 25 (2013) 91904.
- [344] O. Shadrt, J.J. DerkSEN, Direct simulations of dense suspensions of non-spherical particles, *Int. J. Multiphase Flow* 47 (2012) 25–36.
- [345] M.V. Tabib, S.T. Johansen, S. Amini, A 3D CFD-DEM methodology for simulating industrial scale packed bed chemical looping combustion reactors, *Ind. Eng. Chem. Res.* 52 (2013) 12041–12058.
- [346] L.W. Rong, K.J. Dong, A.B. Yu, Lattice-Boltzmann simulation of fluid flow through packed beds of uniform spheres: Effect of porosity, *Chem. Eng. Sci.* 99 (2013) 44–58.
- [347] L.W. Rong, Z.Y. Zhou, A.B. Yu, Lattice-Boltzmann simulation of fluid flow through packed beds of uniform ellipsoids, *Powder Technol.* 285 (2015) 146–156.
- [348] L.W. Rong, K.J. Dong, A.B. Yu, Lattice-Boltzmann simulation of fluid flow through packed beds of spheres: Effect of particle size distribution, *Chem. Eng. Sci.* 116 (2014) 508–523.
- [349] A.G. Dixon, Wall and particle-shape effects on heat transfer in packed beds, *Chem. Eng. Commun.* 71 (1988) 217–237.
- [350] A.S. Cherkasova, J.W. Shan, Particle aspect-ratio effects on the thermal conductivity of micro- and nanoparticle suspensions, *J. Heat Transf.* 130 (2008) 82406.
- [351] Z. Zhou, A. Yu, P. Zulli, Particle scale study of heat transfer in packed and bubbling fluidized beds, *AIChE J* 55 (2009) 868–884.
- [352] Z. Zhou, A. Yu, P. Zulli, A new computational method for studying heat transfer in fluid bed reactor, *Powder Technol.* 197 (2010) 102–110.
- [353] N. Kishore, S. Gu, Momentum and heat transfer phenomena of spheroid particles at moderate Reynolds and Prandtl numbers, *Int. J. Heat Mass Transf.* 54 (2011) 2595–2601.
- [354] J. Gan, Z. Zhou, A. Yu, Particle scale study of heat transfer in packed and fluidized beds of ellipsoidal particle, *Chem. Eng. Sci.* 144 (2016) 201–215.
- [355] D. Jajcevic, E. Siegmann, C. Radeke, J.G. Khinast, Large-scale CFD-DEM simulations of fluidized granular systems, *Chem. Eng. Sci.* 98 (2013) 298–310.
- [356] C.A. Radeke, B.J. Glasser, J.G. Khinast, Large-scale powder mixer simulations using massively parallel GPU architectures, *Chem. Eng. Sci.* 65 (2010) 6435–6442.

- [357] J. Zheng, X. An, M. Huang, GPU-based parallel algorithm for particle contact detection and its application in self-compacting concrete flow simulations, *Comput. Struct.* 112 (2012) 193–204.
- [358] N. Govender, P. Pizette, D.N. Wilke, N. Abriak, Validation of the GPU based BLAZE-DEM framework for hopper discharge, IV International Conference on particle-based methods- PARTICLES 2015, Barcelona, Spain, 2015.
- [359] Y. Shigeto, M. Sakai, Parallel computing of discrete element method on multi-core processors, *Particuology* 9 (2011) 398–405.
- [360] D.K. Kafui, S. Johnson, C. Thornton, J.P.K. Seville, Parallelization of a Lagrangian-Eulerian DEM/CFD code for application to fluidized beds, *Powder Technol.* 207 (2011) 270–278.
- [361] M. Xu, F. Chen, X. Liu, W. Ge, J. Li, Discrete particle simulation of gas-solid two-phase flows with multi-scale CPU-GPU hybrid computation, *Chem. Eng. J.* 207–208 (2012) 746–757.
- [362] J. Longmore, P. Marais, M.M. Kuttel, Towards realistic and interactive sand simulation: A GPU-based framework, *Powder Technol.* 235 (2013) 983–1000.
- [363] N. Govender, R.K. Rajamani, S. Kok, D.N. Wilke, Discrete element simulation of mill charge in 3D using the BLAZE-DEM GPU framework, *Miner. Eng.* 79 (2015) 152–168.
- [364] N. Govender, D.N. Wilke, S. Kok, R. Els, Development of a convex polyhedral discrete element simulation framework for NVIDIA Kepler based GPUs, *J. Comput. Appl. Math.* 270 (2014) 386–400.
- [365] J. Gan, Z. Zhou, A. Yu, DEM simulation of flow of ellipsoidal particles in rotating drums, APCChe 2015 Congress incorporating Chemeca 2015, Melbourne, Australia, 2015.
- [366] N. Govender, D.N. Wilke, S. Kok, Collision detection of convex polyhedra on the NVIDIA GPU architecture for the discrete element method, *Appl. Math. Comput.* 267 (2015) 810–829.